A Study of Cu-loaded SAPO-34 for the Direct Conversion of Methane to Methanol

Karoline Kvande

Thesis for the degree of
Master of Science

Department of Chemistry
Faculty of Mathematics and Natural Sciences

UNIVERSITY OF OSLO

January 2019

Abstract

The direct conversion of methane to methanol has received a lot of attention in research over the last years, due to the potential prospect of finding an alternative route to the energy intensive syngas production for converting methane into valuable products. Extensive research on the optimal reaction conditions, as well as the nature of the active Cu-sites is nevertheless necessary for further improvement of the reaction. Herein, SAPO-34 materials loaded/exchanged with Cu by the means of liquid (LIE) and solid-state (SSIE) ion exchange techniques were investigated for the reaction. The CHA (Chabazite) zeotype, SAPO-34, was chosen due to the limited research found on this material for the direct conversion of methane to methanol.

The materials were characterized by SEM/EDX, PXRD, TGA, N_2-adsorption and ^{27}Al and ^{31}P MAS-NMR techniques to examine the elemental and framework composition, water content and the structural stability after being exposed to the various treatment conditions. The materials were found to be successfully ion exchanged with Cu. This was further supported by an evident decrease in acidity of the Cu-SAPO-34 materials observed by CO and CD_3CN FTIR spectroscopy.

Performance tests revealed that it was possible to convert methane to methanol over the O_2-activated Cu-sites in SAPO-34 under the various reaction conditions applied. However, by comparison to the widely studied aluminosilicate CHA zeolite, SSZ-13, tested under the same reaction conditions, it is apparent that Cu-SAPO-34 has a significantly lower conversion of methane.

Comprehensive examinations of the Cu_xO_y species formed in the materials were executed with CO-FTIR, Raman and XAS. Three- and four fold coordinated Cu-species are evidenced to form after O_2-activation of the materials; among them the active species for methane activation. Interestingly, it was observed that the nature of the Cu-sites found in SAPO-34 deviated from the active sites found previously in SSZ-13. The difference in productivity and Cu-site formation in the two materials were attributed to the difference in framework polarity, as well as location and amount of ion exchange sites in the two materials.

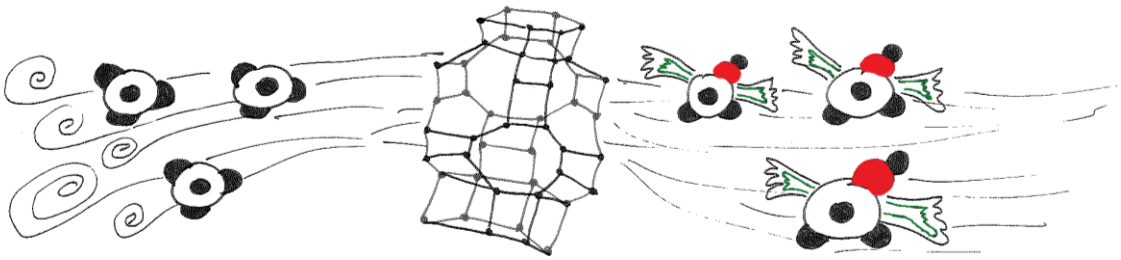

Figure 1. “Giving Methane Wings” – Illustration of the reaction procedure.

2019

A Study of Cu-loaded SAPO-34 for the Direct Conversion of Methane to Methanol

Karoline Kvande

http://www.duo.uio.no/

Print: Reprosentralen, University of Oslo

Acknowledgements

First, I would like to express my deepest gratitude to my supervisors, Stian Svelle, Dimitrios K. Pappas and Michael Dyballa. Thank you for all the guidance, interesting discussions and passionate inputs throughout this work.

I would also like to appreciate Andrea for teaching me the ways of the IR-lab, Kirill Lomachenko and Elisa Borfecchia for performing the tests and analyses of the XAS data, and Michael and Bjørnar for helping me with obtaining the NMR-data. A special appreciation goes to Pablo Beato for giving me the opportunity to spend the summer at Haldor Topsøe to learn and perform Raman spectroscopy experiments.

Thanks to all the great people I have gotten to know at the catalysis group for all the fun, coffee breaks and inspiring working environment.

Kine, Kari and Ina, I want to thank you for all the laughs and stories. My years at Blindern would not have been the same without your friendship, and I hope we will have a lot more fun in the years to come.

I am grateful to my family for your constant support, and for listening to all my phone calls where I babbled away in both excitement and frustration. A special thanks to my brother-in-law, Josh, for proofreading my thesis and giving me amazing feedback.

Last, but definitely not least, I would like to thank you, Simon. Thank you for believing in me, for being my rock through everything, and most importantly, always making me smile!

Table of contents

List of abbreviations used in this thesis

6mr	Six-membered-ring
***BEA**	IZA code for the zeolite framework of Beta
a.u.	Arbitrary unit
AEI	IZA code for the zeotype framework Aluminophosphate-eighteen
AlPO	Aluminophosphate
BET	Brunauer-Emmett-Teller
BSE	Backscattered electrons
CHA	IZA code for the zeolite framework Chabazite
D6R	Double-six-membered-ring
DME	Dimethyl ether
DMTM	Direct methane to methanol
EDX	Energy dispersive X-rays
ESRF	European Synchrotron Radiation Facility
EXAFS	Extended X-ray absorption fine structure
FBR	Fixed bed reactor
FER	IZA code for the zeolite framework Chabazite
FT-EXAFS	Fourier transform-extended X-ray absorption fine structure
FTIR	Fourier transform infrared spectroscopy
GC	Gas chromatography
GC-MS	Gas chromatography with MS detector
IR	Infrared
LIE	Liquid ion exchange
MAS-NMR	Magic-angle-spinning-nuclear magnetic resonance

MeOH	Methanol
MFI	IZA code for the zeolite framework ZSM-5
MMO	Methane monooxygenase
MOR	IZA code for the zeolite framework Mordenite
MS	Mass spectrometry
PXRD	Powder X-ray diffraction
SAPO	Silicoaluminophosphate
SCR	Selective catalytic reduction
SE	Secondary electrons
SEM	Scanning electron microscopy
SM2	Substitution mechanism 2
SM3	Substitution mechanism 3
SSIE	Solid-state ion exchange
TGA	Thermogravimetric analysis
TOC	Table-of-content image
TOS	Time-on-stream
TPR	Temperature programmed reduction
XANES	X-ray absorption near edge structure
XAS	X-ray absorption spectroscopy

List of Publications

In addition to the work presented in this thesis, contributions were also provided for three publications that were not a part of the scope of this thesis. The three articles are listed below.

I. *The Nuclearity of the Active Site for Methane to Methanol Conversion in Cu-Mordenite: A Quantitative Assessment.* Dimitrios K. Pappas, Andrea Martini, Michael Dyballa, Karoline Kvande, Shewangizaw Teketel, Kirill A. Lomachenko, Rafal Baran, Pieter Glatzel, Bjørnar Arstad, Gloria Berlier, Carlo Lamberti, Silvia Bordiga, Unni Olsbye, Stian Svelle, Pablo Beato and Elisa Borfecchia. *Journal of the American Chemical Society*, **2018**, 140, 15270 – 15278.

II. *On How Copper Mordenite Properties Govern the Framework Stability and Activity in the Methane-to-Methanol Conversion*, Michael Dyballa, Dimitrios K. Pappas, Karoline Kvande, Elisa Borfecchia, Bjørnar Arstad, Pablo Beato, Unni Olsbye, and Stian Svelle. *ACS Catalysis*, **2018**, 9, 365 – 375.

III. *Local structure of Cu(I) ions in the MOR zeolite: a DFT-assisted XAS study*, Carlo Buono, Andrea Martini, Ilia A. Pankin, Dimitrios K. Pappas, Chiara Negri, Karoline Kvande, Kirill A. Lomachenko and Elisa Borfecchia. Radiation Physics and Chemistry, **2018**, https://doi.org/10.1016/j.radphyschem.2018.12.031

The Author's Contributions

Article I: The author participated by executing performance tests on several Cu-loaded MOR zeolite materials for the direct methane to methanol conversion. The purpose of the tests were to mimic test conditions applied during *in situ* and *operando* investigations of the materials by XAS. The test conditions and data obtained for these measurements are summarized in Appendix 7.8.

Article II: The author participated by doing both performance tests (multiple and single process cycles) on several Cu-loaded MOR zeolite materials for the direct methane to methanol conversion. The multiple process cycles were performed

to evaluate the stability of the materials. Single process cycles were performed on the materials for a subsequent structural stability investigation by ^{27}Al and ^{29}Si MAS-NMR. The data obtained for these contributions are summarized in Appendix 7.8. The author also carried out mapping with SEM/EDX spectroscopy to investigate the presence of Cl in two of the materials. Furthermore, the author participated in creating the TOC of this publication.

Article III: The author participated in a synchrotron campaign at the European Synchrotron Radiation Facility (ESRF), where the XAS data were collected.

1 Introduction and Scope

Methane is a valuable energy source that has become increasingly abundant as a feedstock, and is an acceptable alternative to petroleum based fossil fuels on our route towards creating a more sustainable environment. Methane can be found in numerous sources, such as natural gas, shale gas and biogas. [3] However, methane itself is a very potent greenhouse gas [3], and because of the complex process of converting methane to higher valued products, associated natural gas is often flared off at oil production sites rather than utilized [4-5]. Flaring of methane causes more than 300 million tons of CO_2 being released to the atmosphere every year. The elimination of flaring from an environmental and resource management perspective has received so much attention that a "zero routine flaring initiative" has been set in motion by the World Bank in order to remove all routine flaring by 2030. This is an agreement between governments, oil companies and development institutions all over the world [6].

The main method for converting methane to chemicals in industry today is *via* the production of synthesis gas (syngas for short). Syngas consists of CO, H_2 and some CO_2. However, the need for finding an alternative method is highly demanded with respect to sustainability, since the current process requires high temperatures (700 – 1000 °C) and high pressures (100 bar) [7]. In addition to being energy intensive, the production of syngas also requires large facilities (the economy of scale) and transportation from remote areas becomes prohibitively costly. Since the cost of transporting methane as compressed or liquefied gas is high, a way of utilizing methane on-site in small-scale operations would be a very good solution for utilization of stranded gas [4]. Direct conversion of methane into liquid products such as olefins, alcohols, ethers and other higher-value products has therefore received a lot of focus in research over the recent years [8].

In nature, methanotrophic bacteria perform the conversion of methane to methanol under ambient conditions, using methane monooxygenase (MMO) enzymes [3]. This reaction has a very high selectivity towards methanol. By using a synthetic, inorganic material (zeolite), in an attempt to mimic nature, a new route has been found that can selectively oxidize methane to methanol, which can be more easily transported from remote areas and small sites. This is the so-called dream reaction (eq. 1), and several groups are dedicated to develop this approach.

$$CH_4 + \frac{1}{2}O_2 \rightleftharpoons CH_3OH \quad (1)$$

Scope and motivation for this study

The direct methane to methanol (DMTM) conversion will be performed by incorporating Cu into SAPO-34 zeolites, and using this material in a cyclic stoichiometric reaction. The Cu-loaded SAPO-34 will first be exposed to an O_2-atmosphere and activated at 500 °C, before the temperature is cooled down to 200 °C and CH_4 is introduced to the material. Finally, steam is passed through the reactor to extract methanol from the pores.

The highest reported value to this day is for a Cu-loaded Mordenite, with a productivity of 0.47 mol_{MeOH}/mol_{Cu} [9]. This value is close to the theoretical limit of 0.5 assuming a dinuclear active Cu-site. Based on the existing research, the conversion of methane to methanol over Cu-loaded zeolites is both plausible and possible [10-13]. However, there are still many unresolved issues and questions regarding the reaction. Most of the focus in the recent years has been on determining how the chemical composition of the zeolites influence the reaction, as well as pin pointing the nature of the active Cu-sites and their role in the reaction [10, 14]. Even though the amount of studies on selective oxidation of methane to methanol is growing every year, the literature found on this reaction tested with SAPO-34 is scarce. SAPO-34 is the silicoaluminophosphate equivalent to SSZ-13, which is a material that has been studied extensively for this type of reaction. Table A10 in the appendix gives an overview of the different versions of Cu-loaded SSZ-13 (Chabazite) that have been tested for the reaction [14].

SAPO-34 has a high technological interest in many important processes. The protonic form of SAPO-34 is actually used on an industrial scale as a catalyst for the conversion of methanol to olefins (MTO) [15], and in the NH_3-assisted selective catalytic reduction (SCR) of NO_x, Cu-loaded SAPO-34 has been proven to work well [16]. These reactions show that SAPO-34 is a versatile and valuable material, exhibiting catalytic activities – with and without Cu in the framework.

With this in mind, and knowing that SSZ-13 exhibits rather high yields of methanol, it became truly interesting to do a thorough investigation of the activity and nature of the Cu-sites in Cu-SAPO-34 for the direct methane to methanol conversion.

2 Literature

2.1 Catalysis

In the chemical industry, almost 90 % of the products are produced from a chemical reaction that includes a catalytic process. A catalyst accelerates a chemical reaction by lowering the activation energy, without being consumed in the reaction itself. Therefore, a catalyst is any substance that can offer an alternative mechanism to the non-catalytic reaction (Figure 2), to obtain a more energetically favorable route, by accelerating the progress of the chemical reaction towards equilibrium. The presence of a catalyst in an industrial chemical process is often used in order to obtain a more sustainable reaction with respect to the environment. With a catalyst present, new routes can be made so the formation of various waste and/or harmful byproducts can be prevented [17].

A catalytic reaction consist usually of several steps. First, the reactants diffuse from the bulk to the catalyst, before they are adsorbed on the catalyst surface. Then, a chemical reaction occurs between the reactants while adsorbed on the surface, producing the desired product. Last, the products are desorbed from the catalyst surface, and diffuse from the catalyst to the bulk.

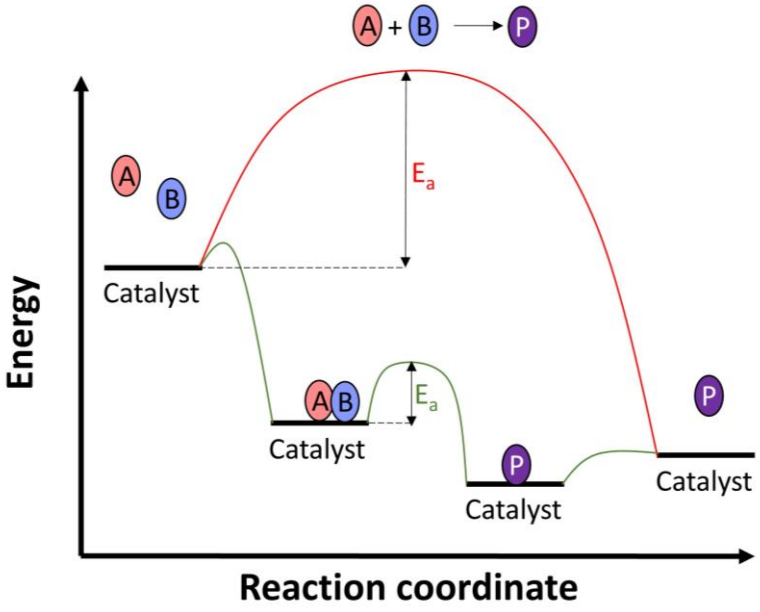

Figure 2. Potential energy diagram for a catalytic (green) and non-catalytic (red) pathway for the reaction of A and B to the product P. Adapted from [17].

Catalysis is often separated into three sub-groups. Heterogeneous, homogeneous and biocatalysis. The latter is the definition of nature's own catalytic processes. Enzymes are catalysts, which have a high specificity towards the substrates (reactants). Enzymatic reactions are optimal for the reactions they are created to perform, which is why we often try to mimic nature when creating synthetic catalysts in the laboratory.

Homogeneous catalysis is when the reactants and the catalyst are in the same phase, most commonly the liquid phase. This type of catalysis is mostly common in the production of fine chemicals, such as pharmaceuticals. However, large scale operations based on homogeneous catalysis does also exist, such as the production of acetic acid from carbonylation of methanol [18]. In heterogeneous catalysis, the reactants and the catalyst are in two different phases. Usually, the catalyst are a solid material, and the reactants are either in a liquid or gas phase. In heterogeneous catalysis, the reactions occur on the surface of the catalytic material, and this approach is mostly used to produce bulk chemicals [17].

2.2 Zeolites

Zeolites are crystalline aluminosilicate minerals with a three-dimensional structure built up from $[SiO_4]^{4-}$ and $[AlO_4]^{5-}$ coordination polyhedra (Figure 3). The tetrahedral are the primary building units, and the atom surrounded by the four oxygen-atoms (such as Si and Al) are often referred to as the T-atom [19].

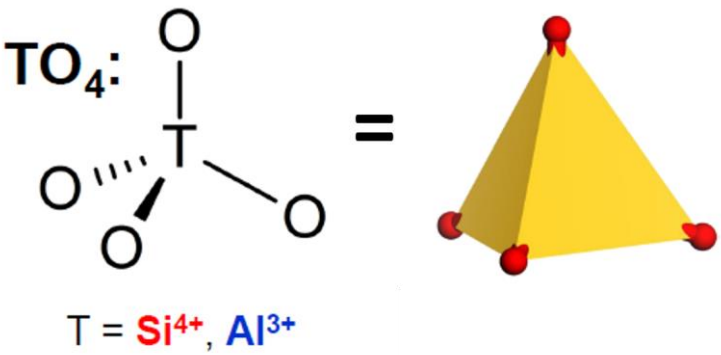

Figure 3. Primary building unit of a zeolite (left), and the unit displayed as a tetrahedron (right) [20].

The primary units (TO_4) are covalently linked together in the corner by a shared oxygen atom, and arranged into secondary building units (sbus) as displayed in Figure 4. Different zeolites are constructed by repeating the secondary building units in various manners to form the framework of the zeolite. The resulting networks are open microporous structures

(≤ 2 nm), with channels and large cavities. Because of the porous structure, zeolites have a high internal surface area, which makes them good candidates for heterogeneous catalysis. Since the secondary building units are assembled in different manners, the size of the channels and pore openings vary between frameworks [17, 19, 21]. The same periodic structure can also be built with other T-atoms, other than Al and Si, known as zeotypes. The most commonly known example of this is aluminophosphates (AlPOs). The framework of AlPOs are built up of alternating $[AlO_4]^{5-}$ and $[PO_4]^{3-}$ tetrahedra. Many zeotypes can be derived from AlPOs by the incorporation of other T-atoms to the framework, such as Si, Co, Zn, Mg and Mn [22]. In this thesis, the two terms, zeolites and zeotypes, will be used interchangeably.

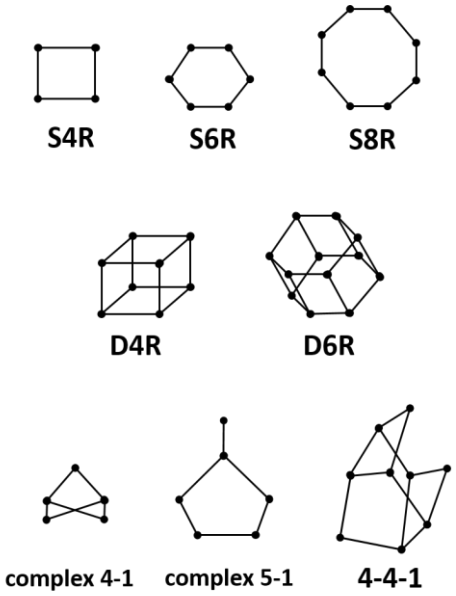

Figure 4. Secondary building units (sbus) in zeolites. Adapted from [19]

2.2.1 Ion Exchange and Acidity in Zeolites

If a zeolite only consisted of SiO_4 tetrahedra, the net charge of the framework would be neutral. Therefore, for every Al-atom present, a negative charge is introduced to the framework, because there is a charge difference between Si(4+) and Al(3+). This negative charge is situated on the oxygen bridge between a Si and an Al atom in the framework, and is neutralized by a cation, such as Na^+ or NH_4^+, present during synthesis [19, 23].

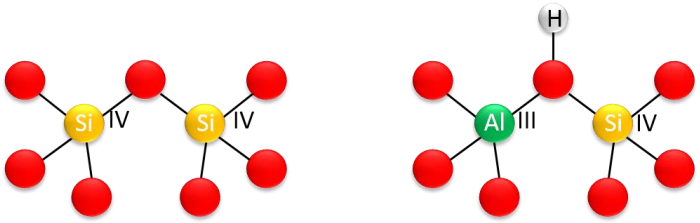

Figure 5. Ball-and-stick representation of a proton balancing the charge, when an Al(3+) exchanges a Si(4+) atom in the framework. Oxygen is represented in red.

When the negative site is stabilized by a proton (H^+), a bridging hydroxyl group is formed between the Si and Al atom, which is known as a Brønsted acid site since a proton can be donated from the site (Figure 5). Because of the acidic character, the zeolites may function as catalysts for acid-base reactions. If transition metals, such as Fe or Cu, are ion exchanged to charge balance the framework, the zeolites can also function as redox catalysts.

Acid properties can also be found in the zeotype family, silicoaluminophosphates (SAPOs). SAPO-materials are obtained by isomorphous replacement of Al or P in a neutral AlPO framework. The incorporation of Si can follow several mechanisms so that different types of Si environment can exist within the framework (Figure 6). Substitution mechanism two (SM2) occurs when Si exchanges a P in the framework. When this mechanism occurs, a Brønsted site is formed within the framework because a net negative charge is introduced from the exchange. Si can also exchange out two neighboring T-atoms (both P and Al). This is substitution mechanism three (SM3), and preserves the neutral charge of the framework, because two tetravalent Si atoms exchange out a trivalent Al and a pentavalent P. The SM3 mechanism introduces Si-rich environments in the framework, known as Si-islands. The incorporation of Si occurs either solely by SM2, or as a combination of SM2 and SM3, in such a way that the combination Si-O-P is prevented since this formation is unstable. Because of these different types of Si incorporation, the amount of Brønsted sites in a SAPO- material relies on the total amount of Si, as well as the relative extent of SM3 mechanism occurring. It has also been suggested that the strength of an acid site is stronger at the edges of Si-rich environments, rather than for Brønsted sites occurring from the SM2 mechanism where the Si is isolated. In a SAPO-material, the concentration of active sites are therefore higher when solely SM2 mechanism occurs, but the strength of the acid sites increase with a higher contribution of SM3 with respect to SM2 [24].

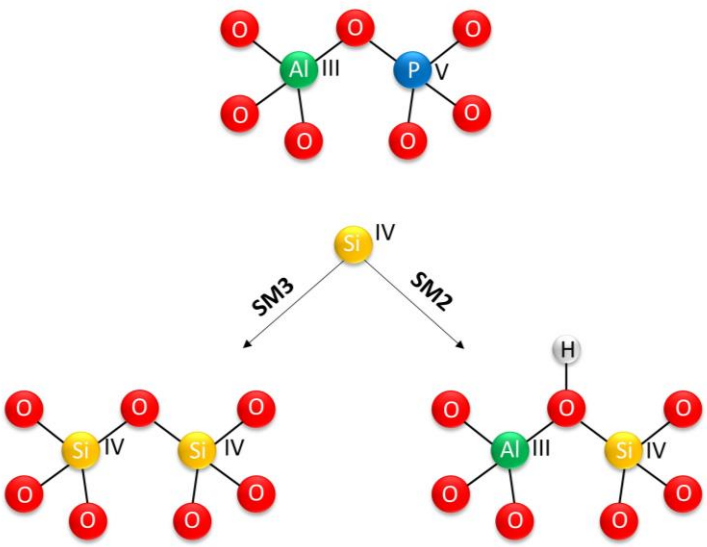

Figure 6. Scheme of the two mechanisms occurring in SAPO-34 when Si is incorporated into the framework.

2.2.2 Shape Selectivity

The unique ion exchange properties of zeolites, in addition to their well-defined crystallinity, microporosity and high internal surface area, make them good candidates to function as catalysts. Since the size of the pores and cavities of the zeolite, and the interacting molecules are in the same order of magnitude, the zeolites have a unique property referred to as shape-selectivity. Shape selectivity can be classified into three categories, as illustrated in Figure 7.

Reactant selectivity (a), arises from the fact that some molecules are constricted from entering the pores, due to the shape being too large to fit inside the pore opening. Only molecules with a size smaller than the pore opening can diffuse into the channels and be converted over the active sites.

When a reaction occurs at the active site, several products with different shape may be formed in parallel or consecutive reactions inside the cavities. The size of the pores can inhibit the bulkier molecules to diffuse out, which leads to a selectivity towards the smaller products. This is called product shape selectivity (b).
When a transition state is involved in a reaction, a restricted transition state selectivity may occur (c). Sometimes, the reactant and product diffuse easily inside the pores, but the

intermediate formed in the transition state is too bulky, and cannot fit inside the pores and cavities around the active site. If this is the case, the overall reaction will be limited, thus, reactions involving less bulky intermediates will be preferred [23].

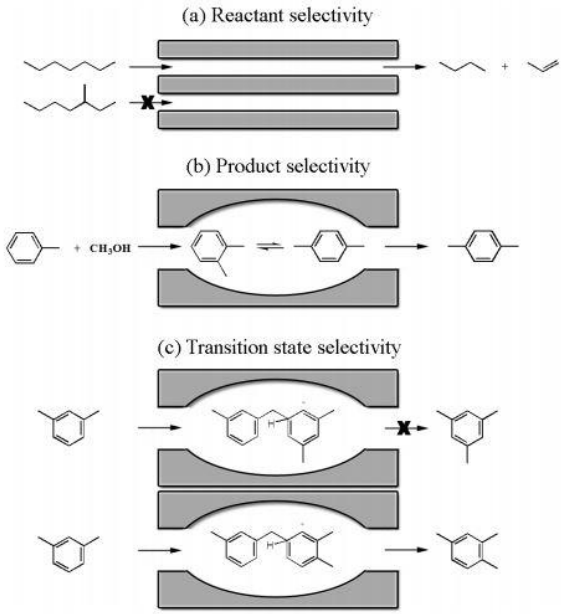

Figure 7. Three forms of shape-selectivity in zeolites [25].

The methanol-to-hydrocarbons (MTH) reaction is an example of a process that rely strongly on the product shape-selectivity effect in zeolites. This is because the reaction occurs on the surface inside the pores. In medium-pore zeolites (10-membered rings) a high selectivity is displayed towards aromatics and alkenes (C^{5+} hydrocarbons). When the reaction occurs over smaller-pore zeolites such as SAPO-34, however, smaller sized products are favored, i.e. olefins (C_2 and C_3 hydrocarbons) [26].

2.2.3 Chabazite (CHA) Framework

The silicoaluminophosphate, SAPO-34, and its aluminosilicate equivalent, SSZ-13, are both zeolites with a Chabazite (CHA) topology. The Chabazite framework is built up from double six-membered rings (D6R) that are stacked in an ABC sequence and interconnected by units of four-membered rings (S4R). The resulting CHA framework has a periodic pattern of barrel-shaped cages interconnected by eight-membered ring windows as shown in Figure 8 (a). The Chabazite structure has a trigonal $R\bar{3}m$ space group and is highly symmetric [14]. Only one crystallographically unique T-site exists in the CHA framework,

and the unit cell consists of 36 tetrahedrally coordinated T-atoms [27]. Among these, four unique ion exchanged locations, depending on which oxygen atom the exchanged cation is attached to, have been determined in the CHA framework (Figure 8 (b)). The protons that are attached to O3 point in to the D6R, and have a more constrained environment than protons attached to O1, O2 and O4, all of which are directed towards the center of the eight-membered ring in a more open environment [14, 28].

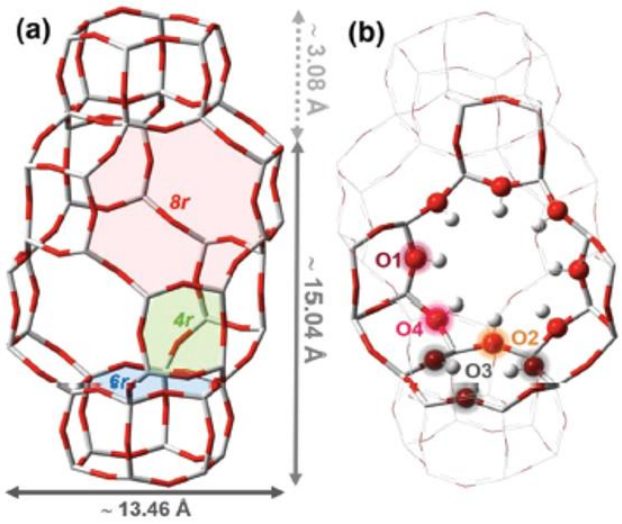

Figure 8. The Chabazite (CHA) type framework (a). Red represents oxygen, and grey represents Si or Al in the case of SSZ-13, while for SAPO-34, the grey sites are either Al, P or Si. (b) Representation of the four different oxygens available for ion exchange in the framework. Published in [14].

SAPO-34/AlPO-18 Intergrowth

The Chabazite structure is closely related to an AEI type framework. Like many other zeolite groups, Chabazite- and the AEI type framework can form an integrowth with each other depending on the choice of structure directing agent, as well as the synthesis route [29]. A structure directing agent is present in the synthesis mixture as a template to help control the morphology of the crystal and to govern the distribution of atoms in the framework [30]. The (silico-)aluminophosphate, SAPO/AlPO-18, has an AEI type framework, and readily forms an intergrowth with SAPO-34. An AEI type framework is built up from the same primary (SiO_4, AlO_4 and PO_4 tetrahedra) and secondary building units as CHA (D6R). However, while the neighboring layers of D6R in SAPO-34 are parallel to each other, in SAPO/AlPO-18, the layers are cross arranged and possesses

therefore a different orientation [29]. Intergrowth occurs by a stacking fault in the layering during the growth of the crystals. Two types of stacking faults can occur, known as displacement and growth faults. A displacement stacking faults occur when a perfect sequence of SAPO-34 layers are interrupted with one layer of AlPO-18, before the sequence with SAPO-34 continues. Growth stacking fault occurs when a perfect stacking of SAPO-34 is changed into a continuing stacking of AlPO-18 layers [29]. The two types of intergrowth are illustrated in Figure 9.

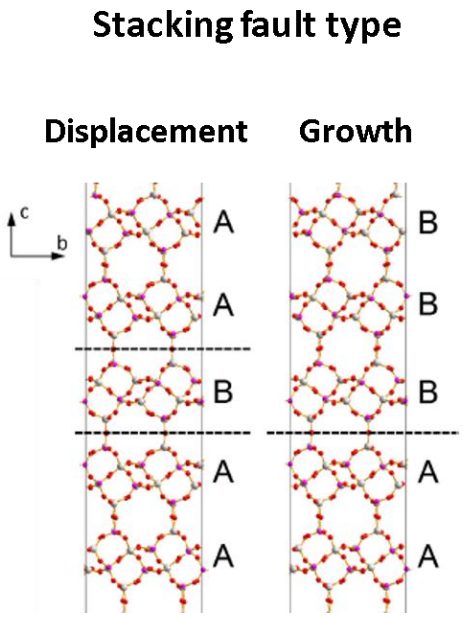

Figure 9. Crystal structure of dislacement stacking fault (left) and growth stacking fault (right) in a SAPO-34 (A) and AlPO-18 (B) family. The dashed line shows a change in the direction of crystal growth. Figure adapted from [29].

2.3 Direct Conversion of Methane

Different approaches have been investigated over the last years for the direct conversion of methane to valuable products, however, there has yet to be a method developed on an industrial scale. One of the reasons for this is due to the chemical stability of the methane molecule. Methane has a melting point of -183 °C, and a boiling point of -162 °C. The C-H bonds are exceptionally strong (425 kJ/mol), and the molecule contains no functional group, magnetic moment or polar distribution to promote chemical reactions. To activate methane, the C-H bond needs to be cleaved, which requires high temperatures and/or the use of oxidation agents [4]. It is thermodynamically complicated to convert methane to other products, since the C-H bond is weaker in the products than in methane, leading to

complications especially due to over-oxidation of the product [31]. The main objective of the reaction design is often, therefore, to find a balance between product selectivity and methane conversion. A wide array of methods have been suggested and tested for the direct conversion of methane (Figure 10). Two important routes are the oxidative coupling of methane to C_2-hydrocarbons [5, 32], and the non-oxidative coupling of methane to aromatics [33-34]. However, both suffers from the limitation arising from methane conversion *versus* product selectivity. In the latter, the yield of aromatics are only around 12 % at 700 °C, with as much as 5-10 % selectivity towards coke formation. Oxidative coupling is also subject to high temperatures (around 800 °C) in the reaction conditions and the ethylene selectivity obtained lie around 30-40 % selectivity at most.

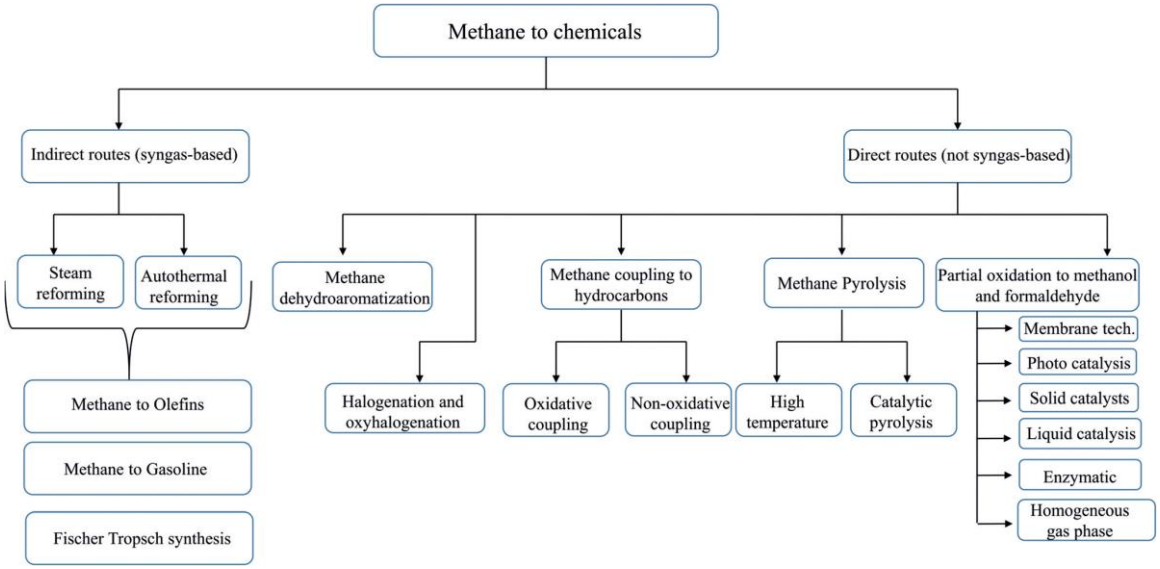

Figure 10. Flow scheme of the current routes for the conversion of methane to valuable products. Figure published in [31]

In this thesis, the focus will be on the direct conversion of methane to methanol. The so-called dream reaction. The conversion to methanol does not require harsh conditions to reach equilibrium, which makes it more desirable for small-scale operations [10]. Methanol is a liquid at standard conditions and is therefore easy to transport, in addition to being an important and valuable product.

2.3.1 Selective Oxidation of Methane to Methanol

Many routes have been attempted to convert methane to methanol. The direct oxidation of methane as a catalytic process have proven to be difficult, because of very low yields obtained due to over-oxidation of methanol [10]. Because of the difficulties with the direct partial oxidation, other approaches have been proposed. Periana et al. suggested a stepwise mechanism based on reacting methane over Pt-based catalysts in sulfuric acid. SO_3 functions as an oxidant in the reaction, and methane would react in solution to form methyl bisulfate, which can be further converted to methanol in a reaction with water. They have accomplished a methane conversion of 90 %, with a selectivity of 81 % towards methyl bisulfate [35]. Even though the Periana chemistry is a very interesting route for the direct conversion of methane to methanol, the chemicals are highly corrosive, and the Pt-based catalysts are expensive and water sensitive, in addition will the subsequent oxidation of SO_2 to SO_3 add process cost [10].

The idea of a stepwise process for converting methane to methanol over Cu-based zeolites is based on the enzyme mono-oxygenase, which is able to convert methane to methanol under ambient conditions with a high selectivity. The conversion is based on copper or iron containing active sites in the enzyme [3]. In 2005, Groothaert et al. initiated the interest for this conversion route when they were able to use O_2-activated Cu-ZSM-5 and Cu-MOR zeolites to convert methane to methanol [13]. The stepwise reaction process consists usually of three steps. First, the material is activated at high temperatures (350-550 °C) with an oxidant present (usually oxygen). After activation, the temperature is lowered substantially to around 60-200 °C, where CH_4 is dosed on the zeolite [14]. When CH_4 interacts with the O_2 activated Cu-centers, the C-H bond will be cleaved, and methyl groups formed. Finally, methanol is extracted from the pores by the use of steam passing through the reactor [36], or sometimes with a solvent, such as ethanol or acetonitrile/water [37]. This process is illustrated in Figure 11. Since the process separates all the reactants, the problem with over-oxidation of methanol is eliminated. This leads to a high selectivity (~90 %), as limited amounts of CO_x or other byproducts are observed. The yield tends to be moderate, and is usually expressed as $\mu mol/g_{zeolite}$ per reaction cycle, or stoichiometrically as mol_{MeOH}/mol_{Cu} [14].

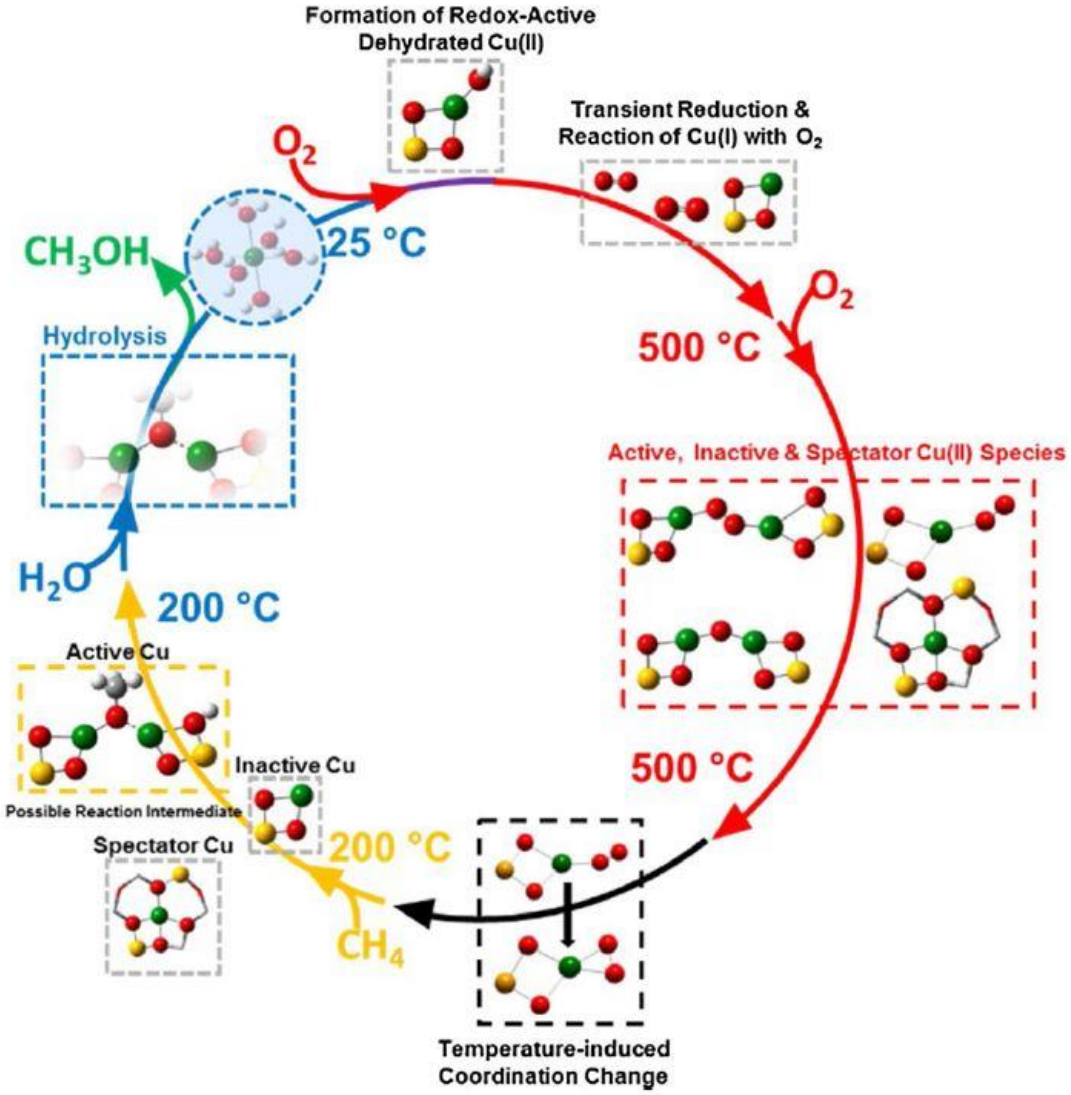

Figure 11. A cyclic representation of the reaction protocol for the stepwise conversion of methane to methanol. Pictorial examples of different Cu-sites suggested to form in the six- and eight membered rings of Cu-zeolites are presented for the key steps in the DMTM conversion. Figure published in [38].

The conversion of methane relies on the amount of active Cu-sites and their nuclearity in the material, and is therefore a stoichiometric process, and not catalytic. However, it has been shown that the Cu-sites can easily be recovered, and the process can therefore function as a looping cycle. Even so, each step requires a long period of time, and excessive amounts of reactants are used, leading to a very low production rate overall. Extensive further understanding and development of this process is therefore necessary for it to be applicable on an industrial scale.

A great amount of zeolite frameworks have been tested for the reaction, such as MOR, MFI, CHA and FER [31, 39]. It is apparent from the literature on this process, that the productivity is greatly influenced by the reaction conditions. In addition, the framework topology, the ratio of Si to Al ((Al+P)/Si for SAPOs), the preparation and exchange method, as well as the amount of Cu all have an impact on the performance [14]. Therefore, the main focus on this topic in the recent years has been on determining the optimal conditions to obtain the highest yield of methanol, in addition to determining structure-activity relationships with the help of spectroscopy to obtain a deeper understanding of the chemistry involved [10, 14, 31]. This is especially in relation to the nature of the activated Cu-sites, and their involvement in the reaction. Figure 11 illustrates some possible Cu-sites that have been proposed to exist in the CHA framework.

2.3.2 SAPO-34 for the DMTM conversion

SAPO-34 is a scarcely researched material for the DMTM-reaction, as mentioned in the introduction to this thesis. Up to date, only one other group has tested Cu-loaded SAPO-34 for the stepwise conversion of methane to methanol. It is also worth mentioning that one group has tested Cu-SAPO-34 for a direct, catalytic oxidation of methane to methanol in a steady-state approach, but since this is not based on the same stepwise reaction principle, it will not be discussed any further here [40].

Wulfers et al. [41] investigated in 2014 the possibility for Cu-loaded small-pore zeolites (8-membered rings) to activate methane in the DMTM-reaction. Two different techniques were used to ion exchange Cu into the materials. Either by the use of a liquid ion exchange with $Cu(II)Ac_2$ as a precursor, or with the use of $Cu_2(I)Cl$ in a high temperature gas-solid exchange. The latter was performed *in situ* in the reactor prior to the reaction procedure. Na-form of the materials were used for the liquid ion exchange, while H-form of the zeolites were used for the *in situ* exchange. The experimental procedures used for the two different materials are presented in Figure 12.

The liquid ion exchanged Na-SAPO-34 ((Al+P)/Si = 6) had a Cu/Si ratio of 0.17, and with this material Wulfers et al. [41] obtained a productivity of less than 0.001 mol_{MeOH}/mol_{Cu}. The *in situ* exchange was performed with an excess amount of Cu_2Cl on top of a bed with

0.300 g of SAPO-34, separated with quartz wool. With this procedure, a much higher productivity of 0.01 mol_{MeOH}/mol_{Cu} was obtained. However, with an in-situ procedure like this, it is difficult to determine if the conversion originated exclusively from ion xchanged Cu or if the Cu_2Cl material on the top of the bed would affect the reaction in any way. When analyzing the material after the reaction with EDX and PXRD, residual Cl and the formation of CuO complexes in the material was observed.

An interesting finding from Wulfers et al. [41] was that the methanol extraction over SAPO-34 occurred at a significantly higher rate than over the other materials tested. They proposed that this effect could be due to a weaker interaction of the intermediates formed during the reaction with the SAPO-framework (presumably due to the different polarity of a silicoaluminophosphate compared to a regular zeolite), in addition to a faster diffusion rate.

Wulfers et al. [41] also employed UV-vis spectroscopy to investigate the Cu-sites in the materials. For the Cu_2Cl exchanged H-SAPO-34 a band at 24 300 cm^{-1} was observed. This band was centered at almost the same place as a band observed for ZSM-5 (23 000 cm^{-1}), which has previously been assigned to a mono-μ-oxo dicopper site. Even so, because of chlorine and CuO impurities on the sample, this assignment could not be verified.

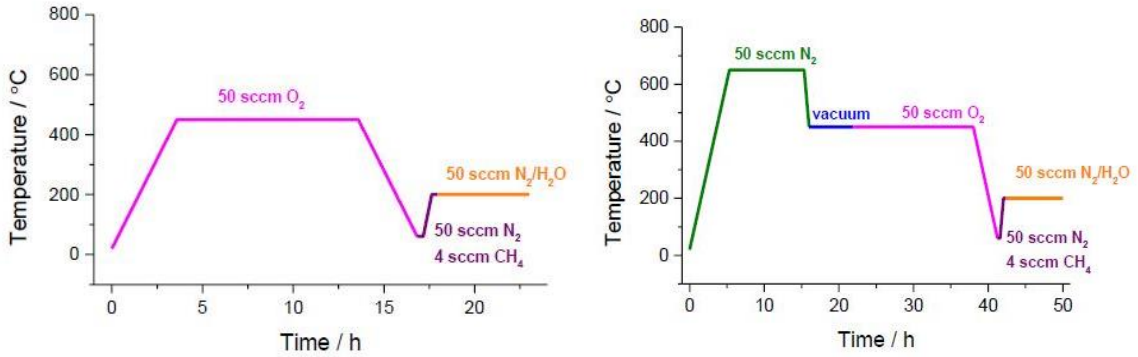

Figure 12. Temperature profile and gas flow rates used for the conversion of methane to methanol, reported in the supplementary information by Wulfers et al. [41] The left is the profile used for the liquid ion exchange material, while the profile on the right is the in-situ procedure used for the Cu_2Cl incorporation and consecutive performance test. (sccm stands for standard cubic centimeters per minute (cm^3/min)).

3 Instrumental Theory of the Characterization Techniques

Characterization offers important tools to study the nature of active materials, and it should therefore be a substantial part of any experimental investigation. In this study, microscopy, spectroscopy and various adsorption techniques are combined in an attempt to understand as much as possible about the structure and composition of the materials. This is in order to rationalize the activity and selectivity of the materials in the direct methane to methanol conversion. This chapter presents the theoretical background for all methods and instrumentations applied in this thesis.

3.1 Scanning Electron Microscopy (SEM)

In a scanning electron microscope (SEM), a narrow electron beam is scanned across the surface of the sample, and by collecting the scattered electrons, a topographical image of the size and shape can be made [17]. Figure 13 shows the schematics of how a SEM operates. The study of the morphology of a zeolite is especially important in catalysis as it can reveal the particle size, and possible defects in the material.

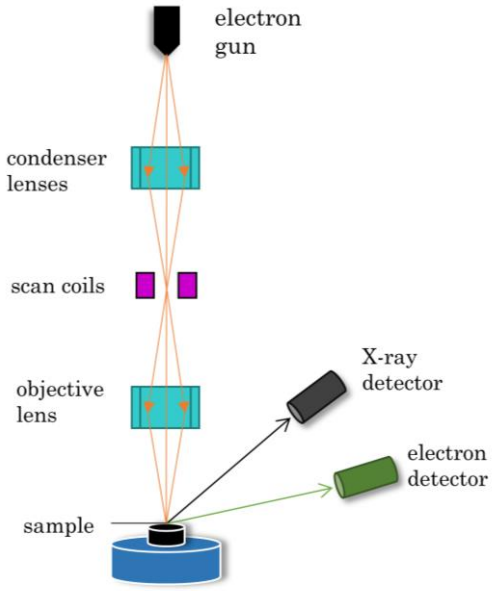

Figure 13. Schematic set up of a scanning electron microscope. Adapted from [17].

A detector collects the yield of electrons as a function of the position of the primary beam. Both secondary (SE) and backscattered electrons (BSE) can be collected. The secondary electrons have low energy (~5-50 eV) and therefore only scatter off the surface region (< 10 nm deep) [42]. With SEM, it is possible to obtain a resolution down to one nm in size. The contrast in an image is caused by the orientation, where the parts that are facing the detector appear brighter than when the facet of the surface is pointing away from it. This brightening effect becomes more apparent on edges, as more secondary electrons leave the surface. Backscattered electrons can travel as far as several 10's of nm up to 100 nm into the sample before returning, and can therefore give information on the composition [17]. Since the amount of backscattered electrons that reach the detector are proportional to the atomic number of atoms, heavier atoms appear brighter than lighter atoms.

In a SEM instrument there is also an X-ray detector, which collects energy dispersive X-rays (EDX) from the sample. With this technique, the sample is bombarded with electrons. When the electrons collide with electrons from the inner shells of atoms, the latter have the potential to be ejected. The hole that is left behind will quickly be filled with an electron decaying from an outer shell, emitting an X-ray photon [43]. The X-ray photon energies emitted are fingerprints of the different elements in the sample, and can therefore be used to create a spectrum, detailing the elemental composition in the material. By analyzing the intensity of the peaks, it is possible to determine the concentration of each element in the sample. It is also possible to do a mapping of the surface while collecting the EDX. This is ideal to determine if the elements in the zeolite are well dispersed throughout the pores and channels, or if there are agglomerations in μm size.

3.2 Powder X-ray Diffraction (PXRD)

Powder X-ray diffraction is a valuable method for the identification of crystalline materials. By collecting X-ray diffractograms from a sample, the crystal structure of a material can be determined and with that, get structural information of a crystalline material. A crystal structure is built up from a unit cell, which contains all information about structure and symmetry of the crystal. With translational displacement, the entire three-dimensional crystal structure can be constructed from the unit cell [44].

When X-rays are incident with the crystal lattice of a solid they are diffracted by the atom planes. Diffractions can occur from different crystal planes. When the difference of the path lengths are equal to a whole number of wavelengths, constructive interference occurs. This phenomenon can be explained by Bragg's law (eq. 2), which is illustrated in Figure 14.

$$n\lambda = 2d\,sin\,\theta \qquad (2)$$

Here, d is the lattice spacing, λ is the wavelength of the diffracted beam and θ is the diffraction angle.

By plotting the intensities of the diffracted beam vs the diffraction angles (2θ), a diffractogram can be created [17]. The position of each peak correlates to a Miller index (hkl), which makes it possible to determine the unit cell parameters of the crystal structure and the diffractogram will therefore work as a fingerprint for the material.

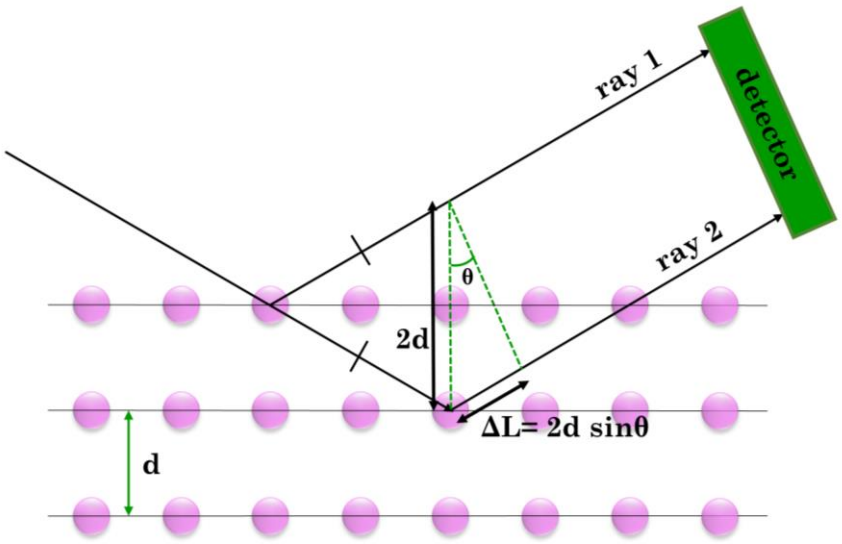

Figure 14. Illustration of Bragg's law. X-rays are scattered by atoms in an ordered lattice. ΔL is the path difference between the two scattered X-rays, and is equal to nλ. Constructive interference occurs when n is an integer (eq. 2). Adapted from [45].

3.3 Thermogravimetric Analysis (TGA)

Zeolites have a high water affinity and can adsorb up to 0.40 $g_{water}/g_{zeolite}$, depending on the framework type [46]. Zeolites, therefore, contain a lot of water at room temperature. In this study, the reaction occurs at elevated temperatures, where all water is desorbed and thus, it is important to know the actual weight of a dry sample for the analysis of the experimental data. Thermogravimetric analysis is a technique to analyze weight changes in a material by exposing it to a controlled atmosphere as a function of temperature or time, and is an ideal method for measuring the water content in a material [47].

3.4 N_2-Adsorption

As described in a previous chapter, zeolites contain pores that provide a high internal surface area. This surface is essential for heterogeneous catalysis since all reactions occur on the surface of the material. The pore-system in a zeolite consists of microporous ($\leq$ 2 nm) channels and cages. It is important to be able to quantify the surface area of these pores, as this gives an indication of whether the surface is intact or slightly damaged by various treatment methods. The surface area is measured by introducing an inert gas, such as N_2 or Ar, which is physisorbed on the material. One can then determine how many molecules that are needed to create a monolayer that covers the whole surface [17]. By applying the adsorption isotherm (eq. 3) of Brunauer, Emmet and Teller (BET), it is possible to create a plot where the slope and intercept will give the monolayer volume. The monolayer volume can then be converted further into the total surface area of the material if the diameter of the adsorbing molecule is known.

$$\frac{p}{v_{ads}\cdot(p_0-p)} = \frac{1}{v_{mono}\cdot C} + \frac{C-1}{v_{mono}\cdot C}\cdot {}^{p}/_{p_0} \qquad (3)$$

Here, v_{ads} is the amount of adsorbed gas, v_{mono} is the volume of adsorbed gas, corresponding to one complete monolayer. C is a constant, p is the partial pressure of the adsorbed gas and p_0 is the vapor pressure above the gas at the temperature used for the measurement [48].

The BET isotherm is only valid under certain assumptions, such as: (i) all adsorption sites are equivalent. (ii) That there are no interactions between the adsorbates, and (iii) that

adsorbed molecules functions as potential adsorption sites for the next layer. The surface area determined by the BET isotherm is not valid for microporous materials because the pores are so narrow that the gas adsorbing on the surface starts condensing [17]. However, the method can still be used for relative comparison between materials.

3.5 Fourier Transformed Infrared Spectroscopy (FT-IR)

Vibrational spectroscopy is widely used as a technique to provide information about the fundamental vibrations of a molecule. All molecules possess separate levels of rotational and vibrational energy. The vibrational energies, and the energy difference between the levels lie in the infrared region of the electromagnetic spectrum [49]. From a mechanistic view, a harmonic oscillator can be used to explain the transitions between the vibrational levels in a diatomic molecule;

$$\upsilon = \frac{1}{2\pi}\sqrt{\frac{k}{\mu}}, \qquad \frac{1}{\mu} = \frac{1}{m_1} + \frac{1}{m_2} \tag{4}$$

Here, υ is the vibrational frequency, k is the force constant (a measure of the bond strength), μ is the reduced mass and m_1 and m_2 are the masses of the two vibrating atoms.

Transitions between energy levels are restricted by the vibrational quantum number (n), which can change by one unit. Nonetheless, in realistic systems, forbidden transitions where $\Delta n > 1$ can occur. These frequencies are seen in the spectrum as overtones. Another rule for the absorption of a photon to occur is that the dipole moment of the molecule must change during the vibration. Therefore, asymmetric or out-of-phase vibrations and polar groups are readily investigated with infrared spectroscopy. The vibrational bands are characterized by their frequency, intensity and band shape, where the frequency is higher when the bond energy is stronger. Since this is different for each molecule, the spectrum will function as a fingerprint for the material in question [49].

The design of the optical pathway in an infrared spectrometer produces an interferogram. This complex, wave-like pattern consists of all frequencies that make up the infrared spectrum with a plot of intensity versus time. By applying a Fourier transformation to the

pattern, the frequencies can be separated into individual peaks and appear as a spectrum with intensity versus frequency [50]. Figure 15 shows the schematics of an infrared spectrometer.

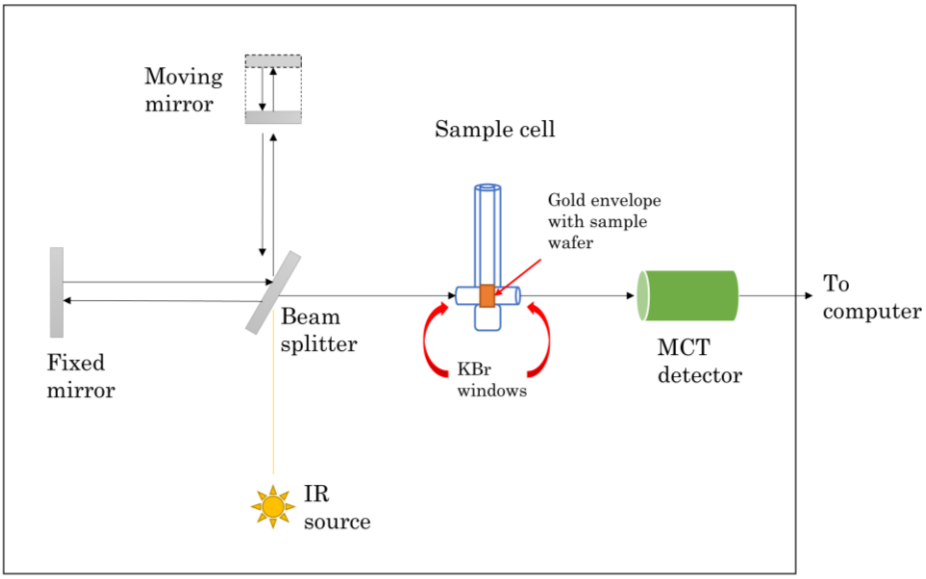

Figure 15. Schematic diagram of Fourier transform infrared spectrometer. Adapted from [50].

In materials science and catalysis, IR spectroscopy is applied to identify adsorbed species on the surface, and to study the way these species interact with various surface sites. The use of probe molecules that are adsorbed on the various adsorption sites can give information about the density/concentration of these sites and/or the strength of interaction between the probe and these sites. A version of the Beer-Lambert law (eq. 5) can be applied to determine the concentration of the acid sites from the absorbance (A).

$$A = \varepsilon bc \qquad (5)$$

Here, ε is the extinction coefficient (cm/μmol), b is the area density of the wafer (mg/cm^2), and c is the concentration (mmol/$g_{zeolite}$).

3.6 Raman Spectroscopy

As with infrared spectroscopy, Raman is also a vibrational spectroscopy technique. When molecules interact with light, the IR bands appear as a result of a change in the dipole moment. However, the Raman bands originate from a change in the polarizability

(distortion of the electron cloud of the molecule by an external electric field). As with IR, these bands are specific to each molecule, and can therefore be plotted as a spectrum which serves as a fingerprint for the molecule or material [49].

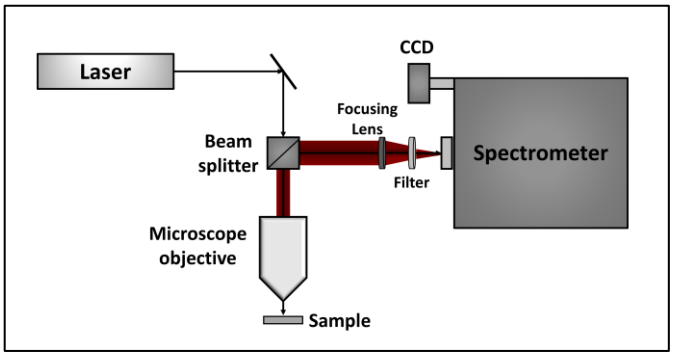

Figure 16. Raman Spectroscopy instrumentation. Adapted from [1].

When high energy light is scattered by a molecule, the incident photon excites an electron from the molecule into a higher energy state. That electron then decays to ground state again, emitting a scattered photon in the process. Usually, when light is scattered from a molecule the bands are elastic, meaning that the incident photons have the same wavelength as the scattered photons. This is known as Rayleigh scattering. However, in 1 out of 10^7 scatterings, the excited photon decays to a state lower or higher than the state in which it was excited from, leading to an inelastic scattering process. This is known as the Raman effect, and arises when the incident photons interact with the electric dipoles of the molecule [51]. When the electron decays to a lower state, it is called anti-Stokes scattering. When the electron returns to a higher energy level, it is called Stokes scattering, as shown in Figure 17.

In a Raman experiment, the sample is irradiated with monochromatic radiation from a laser. The schematic of the instrument is illustrated in Figure 16. The light source covers a wide array of the electromagnetic spectrum including UV, visible and near-IR radiation. In contrast to IR, it is easiest to study symmetric or in-phase vibrations and non-polar groups with Raman [49].

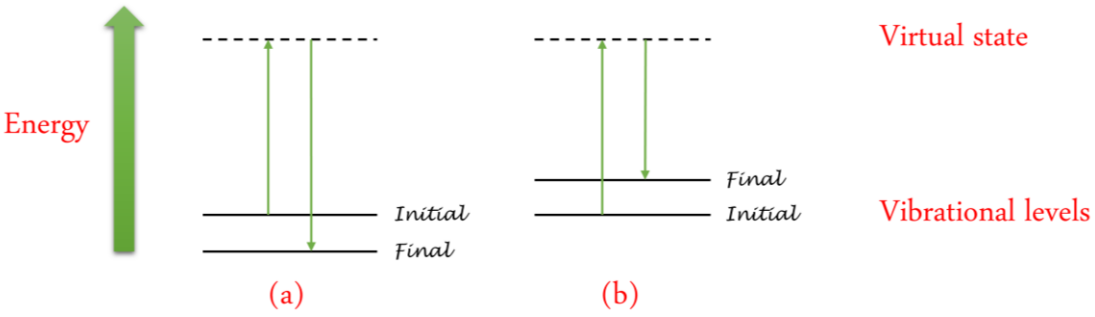

Figure 17. Energy level diagram for Raman Scattering; (a) Anti-Stokes scattering (b) Stokes scattering. Adapted from [51].

Raman-active vibrations can be increased by a factor of 10^2-10^4 when the wavelength of the laser is within the electronic spectrum of a molecule or vibration. This is called resonance enhancement, and is very useful to examine vibrations from certain species that are present in a small amount [51]. In this work, the resonance Raman effect will play an important role to observe Cu-O and O-O vibrations in the materials under investigation.

3.7 Magic-angle-spinning Nuclear Magnetic Resonance Spectroscopy (^{27}Al and ^{31}P MAS-NMR)

Nuclear magnetic resonance is a widely used spectroscopic method, which works within the radio wave- area of the electromagnetic spectrum [52]. The magnetic resonance occurs when the nuclei of specific atoms with non-zero spin are placed in a static magnetic field, and then are exposed to electromagnetic irradiation that excites some of the spins. The free induction decay (FID) of this unbalanced spin system is then monitored. *Via* Fourier Transformation, the time domain is transferred into the frequency domain, and the final spectrum is given after correcting the phase of the signal. This method gives information about the nearest coordinated neighbors to the nucleus under investigation.

Magic angle spinning is used to overcome orientational dependencies that occur with solid state samples, with dipolar and quadruploar interactions being the most important. The sample is rotated rapidly around an angle of 54.74° to the static magnetic field. This averages out the frequency of nuclear interactions that depend on the orientational distribution of molecules in the sample. This makes it possible to retrieve information on the environment around the nucleus under investigation. Depending on the spinning speed and strength of the above mentioned interactions, spinning sidebands might appear [53].

With zeolites or zeotypes, one of the possibilities with MAS NMR is to obtain information about the coordination number of silicon and phosphorous to aluminum, as well as to differentiate between Al that is coordinated to oxygen atoms in a tetrahedral or an octahedral position. When an aluminum is in an octahedral coordination, it is outside the framework, and called extra-framework aluminum.

3.8 X-ray Absorption Spectroscopy (XAS)

When X-rays interact with materials, or more specifically, when they are adsorbed by atoms, the energy involved leads to the excitation or ejection of a core electron. The electron is promoted to an unoccupied state above the Fermi level, and leaves behind a hole in the core. In order to increase the probability of absorption, X-rays of definite energies are used. The absorption is quantified by comparing the incident and transmitted beam energies by the fluorescence emitted from the excited atoms as the core is filled, or by measuring the Auger electrons. The sharp increase in absorption is called the edge, which occurs when the energy of the incident X-ray photons have enough energy to excite electrons. For example, in order to excite electrons from the 1s orbital of Cu, 8978 eV is required. This is known as the Cu K-edge. The emitted photoelectron will interact with the neighboring atoms as a wave radiating out in all directions and returning to the absorbing atom. These interactions can be constructive or destructive and can give information about bond lengths and the local structure around the atom in question. This is called extended X-ray absorption fine structure (EXAFS). Before the energy of the X-ray beam reaches the absorption edge, several weak transitions arise from bound state transitions. In Cu, the peaks comes from 1s → 3d and 1s → 4p transitions. This region is known as X-ray absorption near edge structure (XANES), and covers the spectrum up to the white line, which is the highest peak of the absorption cross-section. An increase in oxidation state correlates with a higher energy of the edge. This implies that the absorption edge of Cu^{2+} should lie higher in energy than that of Cu^{1+} [54].

A typical X-ray absorption spectrum is collected by measuring the incident and transmitted X-ray flux with an ion chamber on both sides of the sample (Figure 18). The transmittance can then be used to calculate the absorbance coefficient, by applying Beer's law (eq. 6).

$$A = -lnT = ln\left(\frac{I_0}{I_1}\right) \quad (6)$$

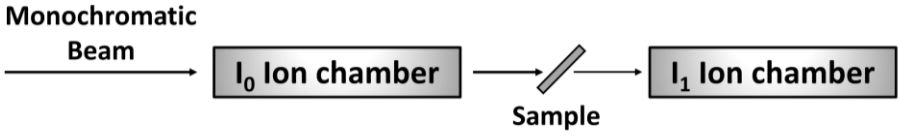

Figure 18. Experimental instrumentation for XAS measurements. The incident (I_0) and transmitted (I_1) intensities are typically measured with an ion chamber.

4 Experimental Methods

4.1 Various Methods for Incorporating Cu into the SAPO-34 Framework

4.1.1 Preparation of SAPO-34

Anna Lind, SINTEF, synthesized the template containing SAPO-34 material according to the synthesis route presented by Mertens et al. [ref: WO 2009/117186 A1]. The molar ratio of the final gel was 0.3 SiO_2/1 Al_2O_3/1 P_2O_5/1 TEAOH/35 H_2O. First, a mixture of orthophosphoric acid, (85 %, Merck), tetraethyl ammonium hydroxide (TEAOH, 35 %, Sigma Aldrich) and deionized water was prepared. The mixture was heated to 30 °C, after which silica (ludox-AS-40, 40 % SiO_2, DuPont) and alumina (Pural SB, 76 % Al_2O_3, SASOL) were added under continuous stirring, before aging at 30 °C for 2 h. The aged gel was transferred into Teflon lined autoclaves and heated to 165 °C, with a heating rate of 5 °C/h, and kept there for 72 h with rotation. Subsequently, the reaction was stopped by quenching, and the obtained powder was washed well with deionized water before drying over night at 95 °C.

The protonic form of SAPO-34 was prepared from the template containing, as-synthesized material. To remove the template, the material was calcined in a multi-step static calcination oven (Naberthem) at 600 °C for 15 h. The heating rate was 2 °C/min, starting from room temperature in static air atmosphere [55].

4.1.2 NH_3-Facilitated Incorporation of Cu in Zeolites

An attempt was made to use NH_3 to incorporate Cu(I) into zeolites. In an article from Shwan et al. 2014 [56] it was claimed that Cu(I) becomes mobile at low temperatures when NH_3 is present. The mobility is proposed to be related to the formation of $[Cu^{I}(NH_3)_x]^+$ (x ≥2) complexes that are formed during NH_3-SCR of NO_x (NH_3-assisted Selective Catalytic Reduction of NO_x).

A ceramic boat was packed lightly with a mixture of a zeolite (Mordenite) that had been mixed thoroughly with Cu_2O-powder using a mortar and pestle. Mordenite was used because large quantities were readily available. The boat was placed in a horizontal, tubular oven with a quartz tube.

Prior to mixing, the Cu_2O-powder was stored in a sealed glass vial under inert Argon to keep it from reacting with air. N_2 and pure NH_3 were introduced at the inlet of the oven so that gas would flow through and over the powder. A flow of 120 ml/min N_2 and < 5 ml/min of pure NH_3 were used. The flows were controlled by a manual ball flow controller and because of inaccuracies at low flow levels, it was not possible to obtain an accurate ammonia flow. After an experiment was determined unsuccessful due to no Cu being detected in EDX, more control of the amount of NH_3 added to the reaction was attempted. To achieve more control, a bottle of 2000 ppm of NH_3 in N_2 was used. Several parameters, such as temperature, amounts of zeolite and Cu(I)O, and time of reaction were varied (See Table 1). To test the reaction even further, a simple set-up (Figure 19) with a fixed-bed reactor was built to obtain a more even flow of reactants through the Cu_2O and zeolite mix.

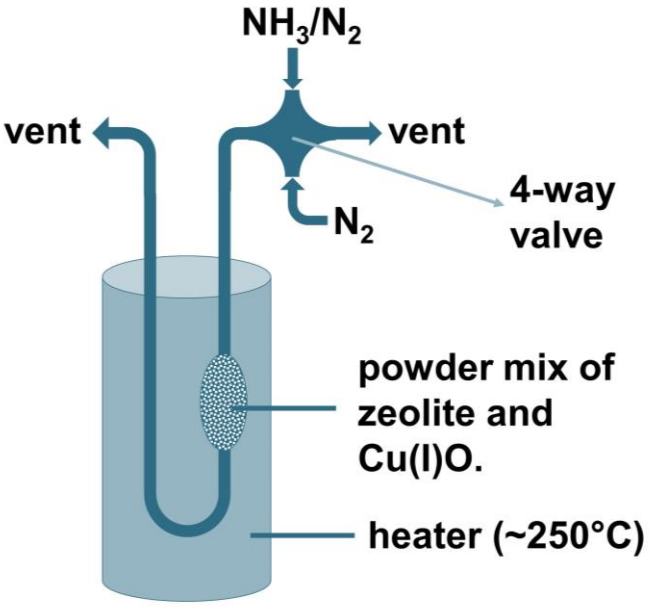

Figure 19. Schematic design of the fixed bed reactor built for the NH_3-synthesis.

Table 1. Overview of the various experimental conditions used with the NH_3-facilitated incorporation of Cu.

		Flow (ml/min)	Calculated Cu/Al**	Temp. (°C)	Time (h)	Mass (g)
MOR_101	Tube	N_2(120)+NH_3(<5)	0.1	250	16	5
MOR_102	Tube	N_2(108)+N_2/NH_3(12)	0.35	200	1	4
MOR_103	Tube	N_2(108)+N_2/NH_3(12)	0.35	110	1	4
MOR_104	Tube	N_2(108)+N_2/NH_3(12)	0.56	110	1	4
MOR_105	Tube	N_2(108)+N_2/NH_3(12)	0.56	200	1	4
MOR_106	Tube	N_2(120)***	0.35	200	2	4
MOR_201	New tube*	N_2(120)***	0.56	200	10	4
MOR_202	New tube*	N_2(108)+N_2/NH_3(12)	0.5	200	10	4
MOR_301	FBR	N_2/NH_3(50)	0.5	250	16	0.3
MOR_302	FBR	N_2/NH_3(50)	0.5	250	10	0.3

N_2/NH_3 = 2000 ppm NH_3 in N_2

**Changed to a different tube.*

***Intended Cu/Al ratio. Calculation procedure can be found in Appendix 7.1.*

****Blind test without NH_3 to check for differences in the EDX-parameters.*

4.1.3 Liquid Ion Exchange for the Introduction of Cu into SAPO-34

Another method to incorporate Cu was the liquid ion exchange (LIE). Two batches of Cu-SAPO-34 were made with this method. The first with a $CuAc_2$-solution of 0.02 M and the second one was made with ten times the amount of $CuAc_2$ (0.2 M). 60 ml of solution was prepared per gram of material. Before the zeolite was added to the $CuAc_2$- solution, the weighed amount was carefully mixed with a few drops of water (~3 mL) to make a slurry so that the framework would not be harmed when added to the $CuAc_2$-solution. This is because zeolites/zeotypes react vigorously when coming in contact with water and the sudden pH-drop can cause precipitation of Cu(II). Universal pH-paper was used to measure the pH, to make sure it was in the range of 5.5-6.0. The mixture was then stirred for 24 hours at room temperature. Afterwards, the mixture was centrifuged at 5000 rpm for 5 min.

Excess water was decanted and replaced with new distilled water before being mixed thoroughly again. This process was repeated 3 – 4 times. Afterwards the material was left in an oven to dry over night at 60°C.

A third material was made using a synthesis protocol similar to one described by Vennestrøm et al. [57]. First a batch with 0.02 M $CuAc_2$- solution was prepared in the same manner as above, followed by two consecutive ion exchanges where the amount of $CuAc_2$ used in the solution was equal to full exchange of the material (Cu/Si-ratio = 0.5). The concentrations of the $CuAc_2$-solutions in the two consecutive exchanges were therefore 0.008 M (All such calculations can be found in Appendix 7.1). A calcining step at 750 °C for 1 hour was applied between each ion exchange. The Cu/Si-ratio resulting from all three batches was later determined by EDX-analysis.

4.1.4 Solid State Ion Exchange

Another method applied was the solid-state ion exchange (SSIE). Two samples were made with this method based on a calculated amount (see calculations in Appendix 7.1) of $CuCl_2$, which was gravimetrically adjusted to give a theoretical Cu/Si ratio of 0.10 and 0.65. The $CuCl_2$-salt was then mixed with water equivalent to the total pore volume of the zeolite, which was determined from the BET-isotherm. SAPO-34 was dried for 2 hours at 60 °C to remove most of the water from the pores before it was weighed out and mixed with the highly concentrated $CuCl_2$-solution, using a glass rod. Finally, the zeolite/Cu-salt mix was placed in a muffle furnace and heated to 550 – 600 °C for 24 – 48 h.

The names of the materials derived from LIE and SSIE were given following this rule:
*x.xx*CuSAPO-34/exchange method*
*x.xx is the Cu/Si-ratio given by EDX-analysis.

Table 2 gives an overview of the treatment data performed on all samples that have been used throughout the thesis.

Table 2. Overview of the experimental conditions used for SSIE and LIE.

	Preparation conditions	Exchange conditions
0.08CuSAPO-34/LIE	0.4 g $CuAc_2$ / ~110 mL H_2O / 1.8 g SAPO-34	Stirring at 25°C (24h)
0.23CuSAPO-34/LIE	3.4 g $CuAc_2$ / ~90 mL H_2O / 1.5 g SAPO-34	Stirring at 25°C (24h)
0.25CuSAPO-34/3xLIE	1. 0.4 g $CuAc_2$ / ~110 mL H_2O / 1.8 g SAPO-34 2. 0.17 g $CuAc_2$ / ~110 mL H_2O 3. 0.17 g $CuAc_2$ / ~110 mL H_2O	Stirring at 25°C (24h), calcining at 750 (1h) – 3x
0.03CuSAPO-34/SSIE	0.93 g from (1.151 g $CuCl_2$*H_2O + 20.0 mL H_2O) / 3.0 g of dried SAPO-34	550°C (24h) + 600°C (48h)
0.22CuSAPO-34/SSIE	0.49 g from (2.30 g $CuCl_2$*H_2O + 20.0 mL H_2O) / 1.5 g of dried SAPO-34	600°C (48h)

4.2 Characterization

4.2.1 Powder X-ray Diffraction

Powder X-ray diffraction was used to investigate the phase purity and to see the effect of heat-treatment to the crystallinity of the materials.

The patterns were measured in a 2θ range of 2-70 with rotation, using a step of 0.02. A deep sample holder was used for all samples. The patterns were measured on a Bruker D8 Discover Diffractometer, using a Cu Kα radiation (λ = 1.5406 Å). The data was analyzed using Eva 4.0 and Topas 5.0.

4.2.2 Scanning Electron Microscopy

Scanning electron microscopy (SEM) in normal and deceleration mode and high angle backscattering images (BSE) was collected on a Hitachi SU8230 and used to determine if the crystals had a typical Chabazite-morphology. SEM was also used to estimate the crystal size. BSE was used to look for CuO nanoparticles. Analysis of the elemental composition

of the sample was performed with energy dispersive X-ray spectroscopy (EDX). Mapping of the sample particle was also employed to see if the elements were evenly distributed throughout the sample. This quantification was performed using a Bruker Quantax system with an X-flash 6|10 detector and Esprit software.

Before conducting EDX-measurements, a small amount of sample was pressed to a wafer (5 tons), and placed on a carbon tape. The holder was also made out of carbon. For the microscopy, a small amount of powder was dispersed on the carbon tape with all excess material blown off using compressed air.

4.2.3 Thermogravimetric Analysis

Thermogravimetric analysis was used to measure the weight of the template in the as-synthesized material, as well as to measure the water content in the parent and Cu-containing materials. For all measurements, around 20-25 mg of sample was weighed out in a platinum crucible and placed on a small balance inside a Stanton Redcroft furnace. The sample was then exposed to an atmosphere of synthetic air consisting of 20 ml/min N_2 and 5 ml/min O_2. For the removal of water, the sample was heated to 300 °C with a heating rate of 2 °C/min. The sample was then kept at 300 °C for 30min before it was cooled to RT.
To measure the weight of the template, the sample was heated to 600 °C at a rate of 2 °C/min, and kept for 15 h, before slowly cooled to RT. These conditions were identical to the calcination procedure performed on the parent material in order to qualify that the template was removed under these conditions. The template removal analysis was performed three times to obtain a statistical value. The values obtained from template removal are presented in Appendix 7.5.

4.2.4 N_2 – Adsorption for Surface Area Analysis

N_2 – adsorption was performed to determine the surface area of the materials. This was done by using a BelSorp MINI instrument. Around 40 mg of sample was added to a cell which was carefully weighed before and after the addition of sample. The cells were weighed because the sample amount is crucial for the data analysis after treatment. The

samples were then pretreated for 3 hours in vacuum (< 0.1 μbar). First 1 h at 80 °C, then 2 h at 300 °C. After pretreatment, the heater was exchanged with a dewar filled with liquid N_2 (LN_2). After the program had finished, the cells were weighed again. The BET adsorption isotherm was estimated from a p/p_0-range of 0.0-0.1, and from it, the surface area was collected.

4.2.5 Nuclear Magnetic Resonance with Magic-angle-spinning

^{27}Al, ^{29}Si and ^{31}P MAS NMR were performed on a Bruker Avance III spectrometer, operating at a magnetic field of 11.74 T at SINTEF in Oslo. The measurements were carried out together with Michael Dyballa. Spectra of all samples were collected using 4 mm probes at a spinning speed of 10 kHz. ^{27}Al spectra were collected with a resonance frequency of 130.31 MHz with 4000 scans. For ^{29}Si, the applied frequency was 99.36 MHz and 1200 scans were taken. Last, the ^{31}P resonance frequency was 202.46 MHz and the spectra were accumulated over 40 scans.

4.2.6 Fourier Transformed Infrared Spectroscopy Measurements

For recording the infrared spectra, a small amount of the material (~15 mg) was pressed to a self-supporting wafer with a round pellet maker (diameter = 1.3 cm), and placed into a gold envelope. All spectra were recorded in transmission mode. The material was first pretreated by heating in vacuum for 1 h at 150 °C, 1 h at 300 °C and 1 h at 450 °C. The sample was then cooled to room temperature, while still kept under vacuum. When probing with CO, small amounts of gas were introduced into the system, and a spectrum was recorded between each introduction. When it was no longer possible to detect any changes in the spectra, the system was de-gassed until approximately 20 mbar of CO was left in the cell, and further cooled down by immersing it in LN_2. At RT, CO interacts with the Cu-sites, while at LN_2-temperatures, the CO is able to interact with the Brønsted acid sites of the material.

To investigate the concentration of Lewis and Brønsted acid sites in the material, the same pretreatment in vacuum was performed on the materials. 14 mbar of deuterated acetonitrile

vapor were then dosed into the cell at room temperature, and kept in contact with the samples for 20 min. Finally, the cells were evacuated for 10 min before being reheated to 200 °C for 2h, and then cooled to room temperature again. The concentration of acid sites were calculated with Beer-Lamberts law. The integrated absorbance of the bands related to Brønsted and Lewis sites were calculated from a deconvolution of the peaks into Gaussian curves. These calculations are presented in Appendix 7.6, together with the deconvoluted spectra. The extinction coefficients of the CN stretch interaction with Brønsted and Lewis applied was determined by Wichterlová et al. to 2.05 and 3.6 cm/µmol, respectively [58].

4.2.7 Raman Spectroscopy Measurements

Raman measurements were performed at Haldor Topsøe A/S in Lyngby, Denmark. These measurements were performed to investigate Cu-O and O-O vibrations in the materials after activation in air. A system for *in situ*-measurements was also employed to investigate the Raman vibrations during the reaction.

For measuring the activated materials, a small amount of material was filled inside a capillary of borosilicate glass with a diameter of 0.5 mm and 0.01 mm wall thickness. After loading, the capillaries were carefully placed in a Cu-block with four slots, and transferred to a muffle-oven. The capillaries were then heated in air to 550 °C with a ramp of 3 °C/min as reported for Cu-SSZ-13 samples by Pappas et al. [11]. After 14 h at 550 °C, the capillaries were sealed with a flame gun while still in the hot oven, in order to avoid re-hydration. The Cu-block with the capillaries was then slowly cooled to room temperature while residing in the oven.

The *in situ* measurements were performed in a CCR1000 cell from Linkam Scientific. A small amount (~25 mg) of pelletized material (150-300 µm), was loaded into the sample holder, and placed inside the cell. All *in situ*-measurements were collected under a blue laser (488 nm).

The spectra collected using the blue laser was recorded with a Horiba LabRamanHR microscope equipped with a Coherent Sapphire laser. The signal was dispersed over 1800 lines/mm grating onto a CCD detector, which was cooled thermoelectrically.

To compare the resonance effects of different wavelengths, spectra of the capillaries were also collected using a red laser (632 nm), which was done with an older version of the Horiba LabRam microscope equipped with a laser from Melles Griot.

For the capillaries, a 50x objective lens was used to focus the excitation beam at the sample. When measuring *in situ* with the Linkam-cell, the excitation beam focus was varied between a 10x and a 50x objective lens in order to avoid the fluorescence effects.

For the *in situ* system, an online Pfeiffer MS was connected after the Linkam cell to measure the effluents of the reaction. The gases were controlled by automatic mass flow controllers and 4-way valve number two (See Figure 20) was used to switch between the dry gases and the saturated helium stream. All the lines from the saturator to the MS were wrapped with heating cords and kept at T>85 °C. For the last experiment, the temperature of the heating cords was raised to 120 °C, to make sure that no water was condensing in the lines. The test conditions were the same as described in test #3 in Table 3 in chapter 4.3.2, with the O_2 activation temperature at 600 °C.

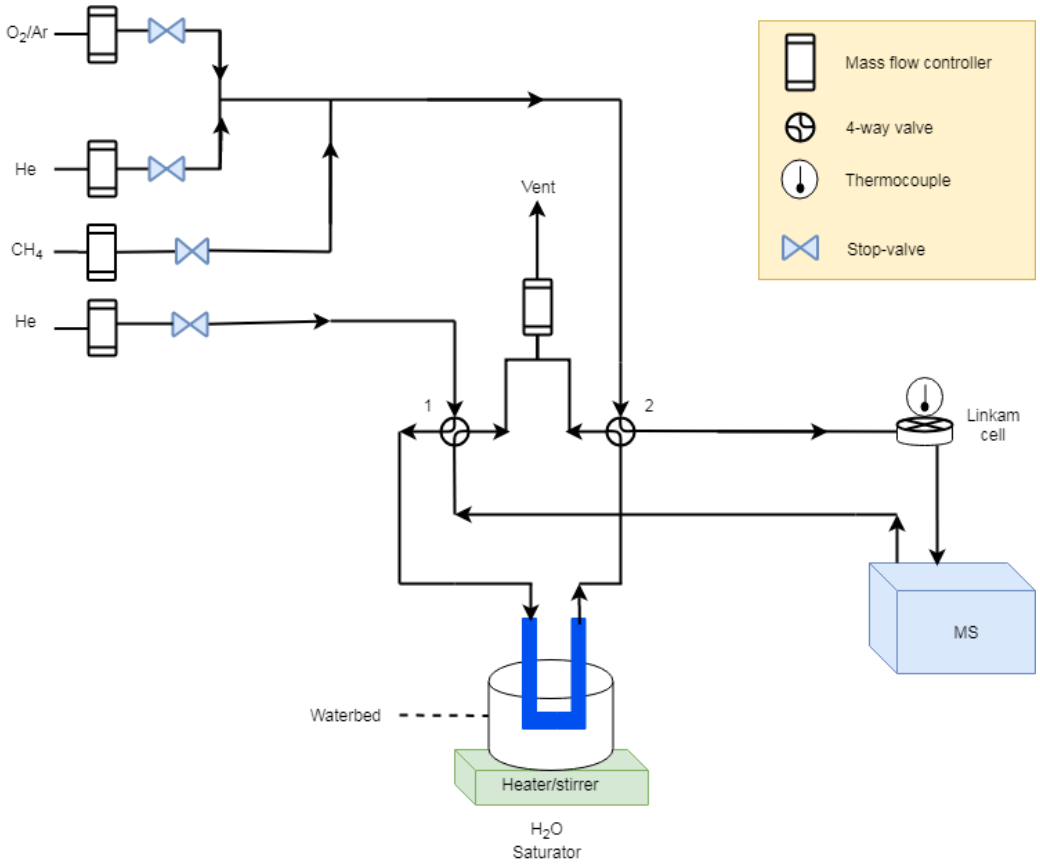

Figure 20. Schematic design of the set-up built at Haldor Topsøe for the M2M-reaction

4.2.8 X-ray Absorption Spectroscopy

In situ X-ray absorption spectroscopy was used to investigate the average electronic and structural properties of Cu ions. The measurements were performed on two of the SAPO-34-materials (0.22CuSAPO-34/SSIE and 0.25CuSAPO-34/3xWIE) at BM23 beamline of the European Synchrotron Radiation Facility [59] by Kirill Lomachenko. The two materials were chosen because they were the samples with the highest yield at the standard conditions (test #1) out of the three samples with high Cu/Si ratio. XAS measurements were performed using a Microtomo reactor cell (Figure 21), designed by the ESRF Sample Environment Group [60],

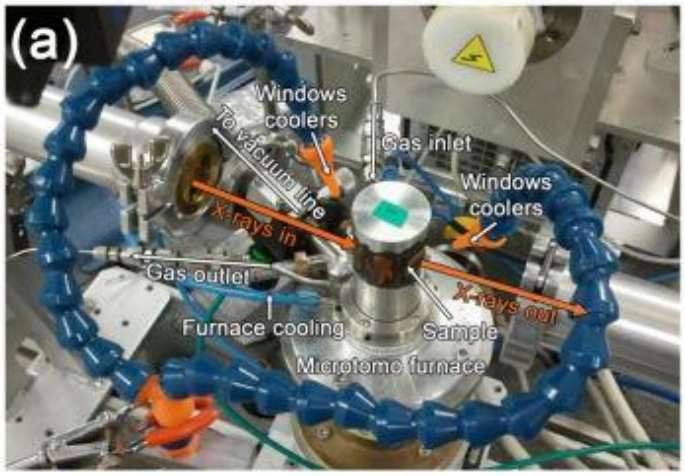

Figure 21. Microtomo reactor cell [2]

integrated in a devoted gas-flow setup, as described by Lamberti and coworkers [2, 61]. The samples were measure in the form of self-supporting pellets of optimized weights of ca. 110 mg and 1.3 cm^2 area, resulting in edge jumps in the 0.4 – 0.9 range for a total absorption after the edge of $\mu x = 2.5$. The *in situ* experiments were executed in the same manner as Pappas et al. [11]. Initially, the samples were activated at 500 °C in pure He for about 60 min (heating rate 5 °C and a total flow rate of 100 ml/min). The He-activated materials were then exposed to 100 ml/min of O_2 at 500 °C and kept at that temperature for ca. 180 min. Finally, the temperature was raised to 600 °C and the materials were maintained at 600 °C in the same O_2 atmosphere for ca. 120 min.

Cu K-edge XAS spectra were collected in transmission mode using a LN_2-cooled flat Si(111) double-crystal monochromator. The incident (I_0) and transmitted ($I_{1,2}$) X-ray intensities were detected using ionization chambers filled with a mixture of He and Ar. The third ionization chamber (I_2) was used for the simultaneous collection of the XANES spectrum of a Cu metal foil for the energy calibration of each spectrum [62]. High quality EXAFS scans were collected to characterize the samples under static conditions after stabilization at constant temperature. These scans were acquired in the 8800 – 9955 eV range with an energy step of 5 eV in the pre-edge region, 0.3 eV in the XANES region and

a constant k step of $\Delta k = 0.035$ Å^{-1} in the EXAFS region. Integration time was 1 s/point for the whole spectrum, resulting in ca. 20 min/scan.

Analysis of the XAS spectra was performed by Elisa Borfecchia. All XAS spectra were normalized to the unity edge jump and aligned in energy using the Athena software from the Demeter package [63]. To characterize each static state of the two samples, three/four consecutive XAS scans were collected and averaged to the corresponding μx(E) curves after checking for signal reproducibility. The χ(k) EXAFS functions were also extracted by using the Athena program. Fourier-transform (FT) EXAFS spectra were obtained by transforming the $k^2\chi(k)$ functions in the range of 2.4-13.0 Å^{-1}.

XANES linear combination fit (LCF) analysis of the XAS spectrum of the hydrated 0.22CuSAPO-34/SSIE material was performed using the Athena software from the Demeter package in the 8972 – 9022 eV energy range. The experimental XANES, $\mu^{EXP}(E)$, based on the qualitative analysis of the observed spectra features, was fitted to a linear combination of two reference XANES spectra ($\mu_i^{REF}(E)$). i.e.: $\mu^{LCF}(E) = \Sigma_i \left(w_i \cdot \mu_i^{REF}(E)\right)$, where $i = 1{,}2$, by optimizing the weights w_i for each reference spectrum. XANES spectra of hydrated 0.25CuSAPO-34/3xLIE (consisting of mobile Cu(II) aqua complexes) and of bulk CuO, both acquired on the BM23 beamline with data collection parameters equivalent to the one described above, was used as references. LCF was performed by setting the total sum of the weights to unity; $\Sigma_i(w_i) = 1$. The corresponding LCF R-factor was ~1×10^{-4}, indicating an excellent fitting quality. The R-factor was computed as $(\Sigma_j[\mu_j^{EXP}(E) - \mu_j^{LCF}(E)] \cdot 2)/\left(\Sigma_j\left[\mu_j^{EXP}(E)\right] \cdot 2\right)$, where j denotes each experimental point in the fitted energy range.

4.3 The Stoichiometric Process for Testing the Direct Methane to Methanol Conversion (DMTM)

4.3.1 Experimental Setup

All tests of the DMTM conversion were performed using a dedicated test-rig. The Cu-zeotype material was pressed, crushed and sieved into a fraction of 425 – 250 µm. 100 mg powder were transferred to a straight quartz tube with a porous plug, which was placed inside a tubular oven and connected to the gas manifold. The quartz tube had an inner diameter of 6 mm. A thermocouple was placed inside a quartz sheath, which was further introduced on top of the bed in the quartz reactor to monitor the temperature during reaction. The set-up is displayed in Figure 22. CH_4, He, O_2 and 10% Ne in He flows were controlled by four different Mass Flow Controllers, and fed to the reactor systematically by the use of stop-valves and 4-way valves. The Ne/He-mixture was bubbled through water, which was heated to 45 °C in an oil bath. The estimated vapor pressure of water at this temperature is 71.9 mmHg [64], which means the Ne/He-stream was saturated with approximately 10 % water, when introduced to the reactor.

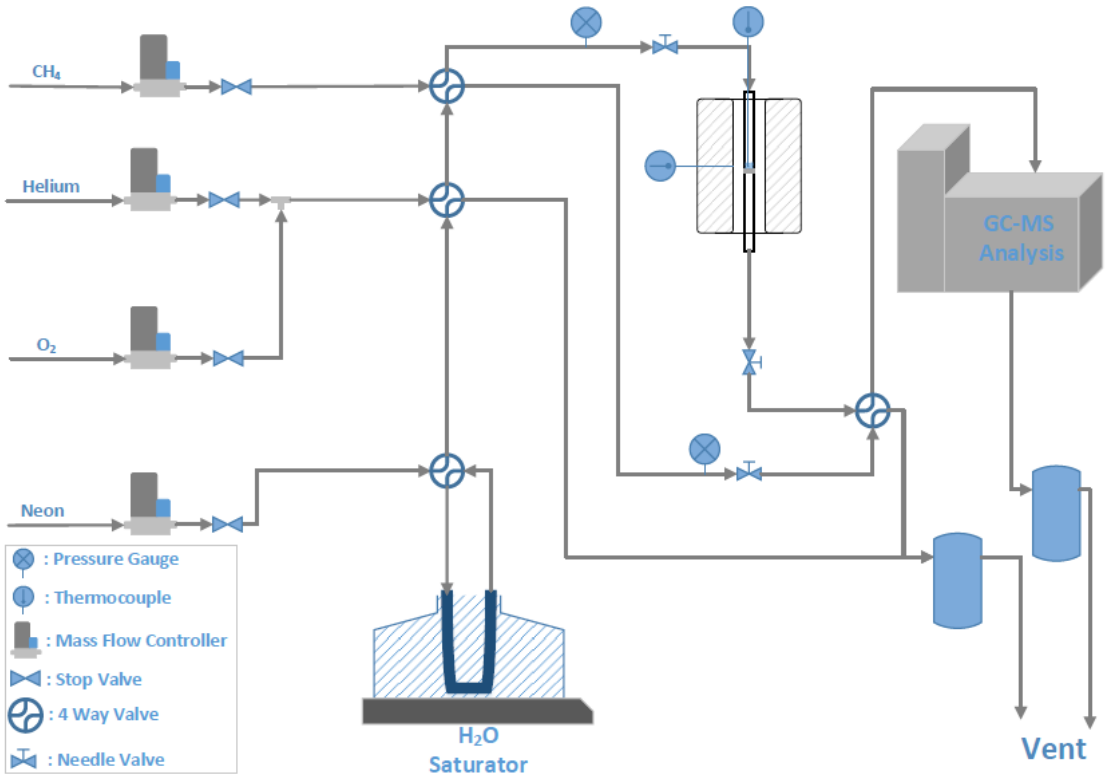

Figure 22. Schematic design of the test rig. The figure is created by Dimitrios Pappas.

4.3.2 Test Conditions

The initial reaction conditions were as follows: The material was slowly heated in He to 150 °C and then de-hydrated at this temperature for > 2 hours. Then the flow was switched to pure O_2, and the temperature increased to 500 °C with a rate of 5 °C/min. The bed was kept under O_2 flow for 8 hours before the temperature was decreased to 200 °C. The flow was then switched to He again for 45 min to remove all excess O_2 from the material and lines before a CH_4 flow was set for 3 hours. After purging with CH_4, the lines were again flushed with Helium for 45 min to remove excess CH_4. Finally, a gas mixture of 10% Ne in He saturated with deionized water was sent over the bed to extract methanol. All flows were set to 15 ml/min, except the saturated Ne/He stream, which was either 13.6 or 14.9 ml/min, depending on the saturator.

In addition to the standard conditions reported above, three changes to the parameters were also tested, which is displayed in

Table 3 below. Test #4 was repeated three times to test if it was possible to regenerate the material.

Table 3: Overview of the different test conditions. The flow time was kept the same for all experiments, and was 8 h in O_2, 3 h in CH_4 and 2 h of extraction. The total flow over the material was always 15 ml/min.

	O_2 activation temperature (°C)	**CH_4 loading temperature (°C)**	**H_2O-assisted Methanol extraction temperature (°C)**	
Test #1	500	200	200	
Test #2	500	200	140	
Test #3	600	200	200	
Test #4	600	200	140	Repeated 3 times

Effluent Analysis

By using gas chromatography combined with mass spectrometry, it was possible to both qualitatively, and quantitatively analyze the effluents of the reaction. The different species will elute from the column of the GC at different times, depending on the characteristics of the material and the column used. When the components elute, they will be ionized, and further break into charged ions derived from the original compound. The mass spectrum functions as a fingerprint of the compounds. By combining the two methods, it was possible to separate and identify each individual compound and also determine the concentration of each component [65].

The effluents were analyzed with a Hewlett Packard 6890/6972 GC-MS system, equipped with a Supel-Q PLOT capillary column, and He was used as carrier gas. The method was programmed to sample isothermally at 125 °C, over a period of 3.5 minutes. A sample was therefore collected approximately every fourth minute over a period of 2 hours during extraction.

Qualitative analysis

All mass spectra of the expected products were found in the NIST Chemistry WebBook. By comparing these, the m/z fragments of the different compounds were selected not to overlap with the other products. Table 4 gives an overview of the m/z fragments used to trace the various species in the effluent.

Table 4. Overview of the m/z fragments traced with the GC-MS.

H_2O	Ne	CO	CH_3OH	CO_2	CH_3OCH_3
18	20	28	31	44	46

Quantitative Analysis

This method relies on using excess amounts of O_2 and CH_4 to make sure that all active sites are covered. Therefore, it is not pertinent to talk about turn-over-frequencies and turn-over-

numbers, which rely on known amount of reactant. Instead, the yield (mol of methanol/g of zeolite), productivity (mol of methanol per mol of Cu) and the selectivity are reported.

Selective Ion Monitoring (SIM) was used to quantify the yield of the products. The mass spectrum during extraction was plotted as abundance vs time. The abundance was calibrated to a gas mixture with a known amount of the product to give quantitative data. This was done by making a calibration curve for the abundance vs the ppm-values of various amounts of the known gas mixture (See Appendix 7.4). The slope of the curves are the calibration factors, which are multiplied with all data collected.

During extraction, 30 analyses were carried out over a period of two hours. The integrated areas are were then normalized to the area of the Neon, which acts as the Internal Standard of the system.

$$A(x)_{normalized} = A(x)_{extracted} \cdot Ne_{ratio} \quad (7)$$

, where $\mathrm{Ne_{ratio}}=\mathrm{A_{Ne}}\cdot\mathrm{A_{Ne,\,cal}}$

$\mathrm{A_{Ne,\,cal}}$ was the abundance of Neon when the calibration factors of the other products were collected.

After subtracting the background, the area of the products, X, are multiplied by the calibration factors ($\mathrm{A_{x,cal}}$) to achieve the ppm-values.

$$X_{ppm} = (A(X)_{normalized} - A(X)_{background}) \cdot A_{X,cal} \quad (8)$$

$$X_{\%} = X_{ppm}/10000 \quad (9)$$

From the %-amount of X, and by knowing the flowrate of the extraction feed, the volume of X can be found:

$$V_X = \frac{X_{\%} \cdot ex.feed}{100} \quad (10)$$

By knowing the density of X (ρ_X) at the temperature of which the lines are kept at (~145 °C), the chemical amount of the product (n_X) are determined.

$$n_X = \frac{V_X \cdot \rho_X}{M_X} \quad (11)$$

Finally, the yield can be calculated by dividing the amount of X by the dry weight (m_X), which is calculated from the mass of the material and the water content found with TGA:

$$yield_X = \frac{n_X \cdot 1000000}{m_X} = X\ \mu mol/g \quad (12)$$

By using Origin software, the yield is plotted, and the integral of each plot gives the total yield of each material (See an example in Appendix 7.3). DME is included in the total yield of methanol by considering the molecule as two times a methanol molecule, as shown in the chemical equation below.

$$2CH_3OH \leftrightharpoons H_3COCH_3 + H_2O \quad (13)$$

The total yield then becomes:

$$Yield_{MeOH,total} = yield_{MeOH} + (2 \cdot yield_{DME}) = x\ \mu mol/g \quad (14)$$

The selectivity was calculated from the total methanol yield divided by the total yield of all products.

$$Selectivity = \frac{yield_{MeOH,total}}{yield_{MeOH,total} + yield_{CO} + yield_{CO_2}} \cdot 100\% \quad (15)$$

The amount of methanol produced is directly correlated to the amount of active sites in the zeolites. Since the active sites are at the Cu-centers, these govern the productivity of the material. Based on this, the productivity was presented as amount of methanol divided by amount of Cu.

$$Productivity = \frac{mol_{MeOH,total}}{mol_{Cu}} \quad (16)$$

The amount of Cu was calculated from the atomic percent found with EDX (See calculations in the Appendix 7.2).

5 Results and Discussion

5.1 NH_3-facilitated Cu-incorporation

The idea of performing Cu-incorporation into zeolites in the presence of ammonia comes from a study by Vennestrøm and coworkers [56, 66]. In that work, the authors subjected a physical mixture of copper oxides (Cu^{I}_2O and $Cu^{II}O$) and zeolites (MFI, *BEA and CHA) to gases involved in the NH_3-assisted Selective Catalytic Reduction of Nitrogen Oxides (NO, NH_3, O_2 and H_2O). They observed that NO facilitated the reduction of Cu^{II} to Cu^{I}, which upon interaction with NH_3 formed mobile complexes ($[Cu^{I}(NH_3)_x]^+$, ($x \geq 2$)), that could migrate to ion exchange positions in the zeolite frameworks. The temperatures were varied between 250 and 550 °C, and for MFI and *BEA, the Cu can be ion exchanged already at 250 °C. Higher temperatures (450 °C) were required for CHA, which was correlated to the narrower pores in this framework. In the article, they also used Cu^{I}_2O as the Cu precursor and performed the ion exchange without the presence of NO. All the experiments in the aforementioned study were performed *in situ* prior to the SCR reaction. In our case, we aimed to investigate if it was possible to perform this Cu-exchange *ex situ* in order to produce active materials for the DMTM conversion. Mordenite was used in this study due to it being readily available in large quantities at that time.

Shwan et al. [56] used a small fixed-bed reactor (i.d. = 2 mm), and 10 mg of zeolite mixed with Cu_xO for the *in situ* exchange procedure. A total flow of 225 mL/min (500 ppm NO, 530 ppm NH_3, 5 % H_2O and 10 % O_2 in N_2) was applied. For the pure NH_3-exchange, a flow of 530 ppm of NH_3 in N_2 was used. The temperatures were varied between 250 and 550 °C, and treated for either 5 or 10 h.

As seen in Table 5, the NH_3-facilitated Cu incorporation into zeolites was tested, utilizing a wide variety of experimental conditions, such as Cu-content, temperature and time. The purpose was to make an active material for the direct conversion of methane that could be tested and characterized; therefore, an amount of approximately 4-5 grams of zeolite was used. Initially, the total flow was set to 120 mL/min, due to limitations of the manual flow controllers, and the gas mixture used was 200 ppm NH_3 in N_2. The starting temperature was 250 °C, and the exchange time was set to 16 h. When low amounts of Cu as well as a deposited white powder was observed on the surface of the tube during exchange after the

first experiments, a hypothesis was made that the temperatures facilitated for the Cu to be extracted with the NH_3-flow. Despite multiple short tests with lower temperatures and higher Cu-amounts in the samples, the Cu/Al ratio did not improve. An observation was made with EDX in which the Cu content was significantly different, depending on which spot was being analyzed, despite being on the same pellet. This lead to the observation that the Cu agglomerated instead of being ion exchanged by the presence of ammonia. After performing a blind test without NH_3, where the same Cu-agglomerates were observed with EDX mapping, an attempt was made to obtain similar conditions to Shwan et al. [56]. The exchange was performed in a fixed-bed reactor (FBR), where 0.300 g material were used, and the temperature was set to 250 °C. The manual flow controllers allowed for a total flow of 50 ml/min. A gas mixture with 2000 ppm NH_3 in N_2 was used to observe if an excess amount of NH_3 would affect the results. However, the change to FBR did not improve the Cu/Al ratio of the exchange, and the same agglomerates were observed with mapping.

Table 5. Experimental conditions performed, and Cu/Al ratios obtained after the NH_3-facilitated incorporation of Cu in Mordenite.

		Flow (ml/min)	Calculated Cu/Al*	Temp. (°C)	Time (h)	Mass (g)	Cu/Al**	Si/Al**
MOR_101	Tube	N_2(120)+NH_3(<5)	0.1	250	16	5	-	-
MOR_102	Tube	N_2(108) + N_2/NH_3(12)	0.35	200	1	4	0.14	11.4
MOR_103	Tube	N_2(108) + N_2/NH_3(12)	0.35	110	1	4	0.13	11.6
MOR_104	Tube	N_2(108) + N_2/NH_3(12)	0.56	110	1	4	0.02	8.04
MOR_105	Tube	N_2(108) + N_2/NH_3(12)	0.56	200	1	4	0.14	11.1
MOR_106	Tube	N_2(120)	0.35	200	2	4	0.08	11.5
MOR_201	New tube	N_2(120)	0.56	200	10	4	0.03	11.6
MOR_202	New tube	N_2(108) + N_2/NH_3(12)	0.5	200	10	4	0.05	11.5
MOR_301	FBR	N_2/NH_3(50)	0.5	250	16	0.3	0.02	11.5
MOR_302	FBR	N_2/NH_3(50)	0.5	250	10	0.3	0.03	11.3

**Example of the calculations performed to obtain the theoretical Cu/Al ratio is presented in Appendix 7.1.*

***Si/Al and Cu/Al are calculated from EDX.*

Figure 23 depicts mapping with EDX over a large area of a pressed slab of one of the samples that showed the highest Cu/Al ratio (0.14). This mapping shows how Cu_2O was mixed with the zeolite, forming agglomerates instead of being ion exchanged by the formation of mobile $CuNH_3$-complexes, which was the expectation. From the BSE images, it becomes evident that Cu did not diffuse into the material, as Cu-nanoparticles are visible on the surface of the crystals/agglomerates. This was further supported by visible black particles in the exchanged material. The material (MOR_102) was eventually tested, using the optimal reaction conditions found by Pappas et al. [11]. The conditions employed were 8 hours of activation in O_2 (500 °C), 6 hours in methane at 200 °C, and finally, an extraction step with 10 % H_2O in Ne/He at 200 °C. A flushing with He was performed between each step. The total yield of methanol obtained from this reaction was 1.25 $\mu mol_{MeOH}/g_{zeolite}$. A Cu-exchanged Mordenite sample (Cu/Al = 0.13), prepared with liquid ion exchange was also tested for comparison under the same conditions. The results for the latter are published in our recent study in ACS Catalysis [9], and the total methanol yield was 39 $\mu mol_{MeOH}/g_{zeolite}$, proving that NH_3-facilitated exchange did not lead to a significant amount of active Cu_xO_y-species in the material.

Based on the results obtained in this preliminary study, it is clear that under the conditions employed, Cu is not able to form active sites with the particular exchange method. A future approach to test the exchange method further could be to introduce NO in the reaction gas. We decided not to test that in this study due to practical limitations in the laboratory. and because it went beyond the purpose of the experiment, which was to investigate the possibility of low temperature incorporation of Cu in zeolites in the presence of NH_3 in a simple setup. The highest temperature used was 250 °C. Without NO in the reaction mixture, Cu might need higher temperatures in order to preferentially bind with ammonia instead of oxygen. It is however important to keep in mind that too high temperatures would facilitate bond breakage between NH_3 and Cu. Another explanation could be that NO is necessary in the gas mixture to keep Cu in its reduced form. To further investigate the specific exchange method, it is suggested to use the exact conditions employed by Shwan et al. [56]; i.e. utilizing zeolites with smaller sized pores, and performing the reaction using the same gas flows and temperatures.

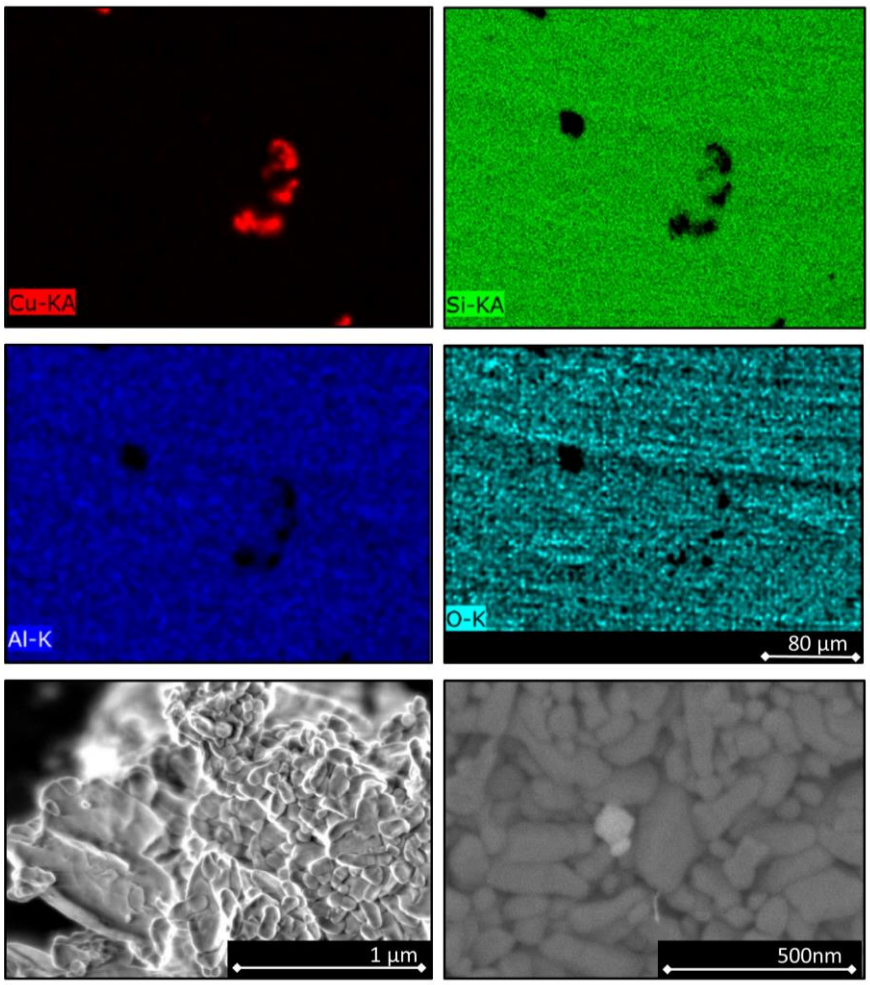

Figure 23. The top four images show a mapping performed over a large surface area of a pressed pellet of the material, MOR_102. It is evident that no Cu was dispersed in the material, but rather formed large agglomerations. The bottom left image is a SE image of the Mordenite surface and the bottom right image is collected in BSE mode, where Cu-nanoparticles are observed.

5.2 Standard Characterization of (Cu-)SAPO-34

Based on the poor results obtained by the NH_3-facilitated Cu exchange, more standardized zeolite ion exchange methods were performed in order to incorporate Cu into the SAPO-34 material. Due to the small pores and polar framework of SAPO-34, the introduction of Cu from liquid ion exchange has proven to be difficult. Often the exchange procedure has to be repeated several times to obtain the desired amount of Cu in the material [41, 57]. However, since Pappas et al. [11] were able to introduce the desired amount of Cu into SSZ-13 with only one exchange, it was reasonable to follow this approach. Both single and multiple ion exchange approaches were executed and compared. Solid-state ion exchange was also applied in order to compare how the various exchange procedures would impact the activity of the materials in the DMTM-conversion.

5.2.1 Physico-chemical characterization

Table 6. Physico-chemical data of the samples by SEM/EDX, N_2-physisorption and TGA.

	Exchange conditions	[Al+P]/Si / (Si/Al)*	Cu/Si / (Cu/Al)*	Cu (µmol/g)	Water content** (%)	Specific Surface area*** (m^2/g)
H-SAPO-34	-	14.9	-	-	16.4	698
0.08CuSAPO-34/LIE	LIE	13.5	0.08	87	13.8	690
0.23CuSAPO-34/LIE	LIE	14.2	0.23	234	7.1	662
0.25CuSAPO-34/3xLIE	3xLIE	14.7	0.25	249	17.7	616
0.02CuSAPO-34/SSIE	SSIE	13.8	0.03	34	11.7	670
0.22CuSAPO-34/SSIE	SSIE	14.8	0.22	224	6.9	579
0.3CuSSZ-13(12)****	LIE	(12.1)	(0.34)	420	12.7	766

*All elemental analysis data are collected with EDX spectroscopy.

**Calculated from TGA.

***Calculated from BET analysis of N_2-adsorption data.

****The SSZ-13 material is received from Haldor Topsøe A/S, and Michael Dyballa has performed all standard characterizations on the material.

The water content was measured by TGA in order to obtain the weight of the dry sample, which is used in the analysis of the activity test data. It appears that the water content varies a lot in the different materials. A loose trend can be observed, however, that when the amount of Cu that is ion exchanged into the material increases, the water content also increases. The two high loading samples (solid state and liquid ion exchange), deviate from this trend. These samples have extra nanoparticles of CuO, as is shown above, which may lead to less water in the framework. No pretreatment was performed on the materials before the TGA-measurements, so there is also an error that arises from the daily changes in humidity. The weight loss of the template-containing SAPO-34 was also measured by TGA. Three measurements were collected in order to obtain an average value. The average value was then compared to the weight loss of the material after a calcination process utilized to remove the template. The value obtained from TGA was 16.8 %, while the weight loss measured after calcination was 17.5 %, indicating that all the template was removed from the SAPO-34 material during calcination.

The surface area was measured by N_2-adsorption, and then calculated from the BET isotherm. The results presented in Table 6 indicates that the samples retained their high specific surface area, and that no significant changes by any of the heat treatments during the various ion exchange methods were observed. The surface area measured by BET is not a quantitatively meaningful value when working with microporous materials, but it is still a good characteristic to use for comparison of similar materials.

5.2.2 SEM/EDX

The parent material, as well as all the Cu exchanged materials, were analyzed with scanning-electron microscopy. By collecting the images in deconvolution mode, it was possible to overcome brightness and blurring that appeared in the images. Deconvolution reduces systematic errors in the instrument, which affects the resolution and therefore the contrast. All samples had, as expected, similar morphology and crystal size indicating that the ion exchange did not affect the crystals. Secondary electron (SE) images in deconvolution mode of the parent material is depicted in Figure 24.

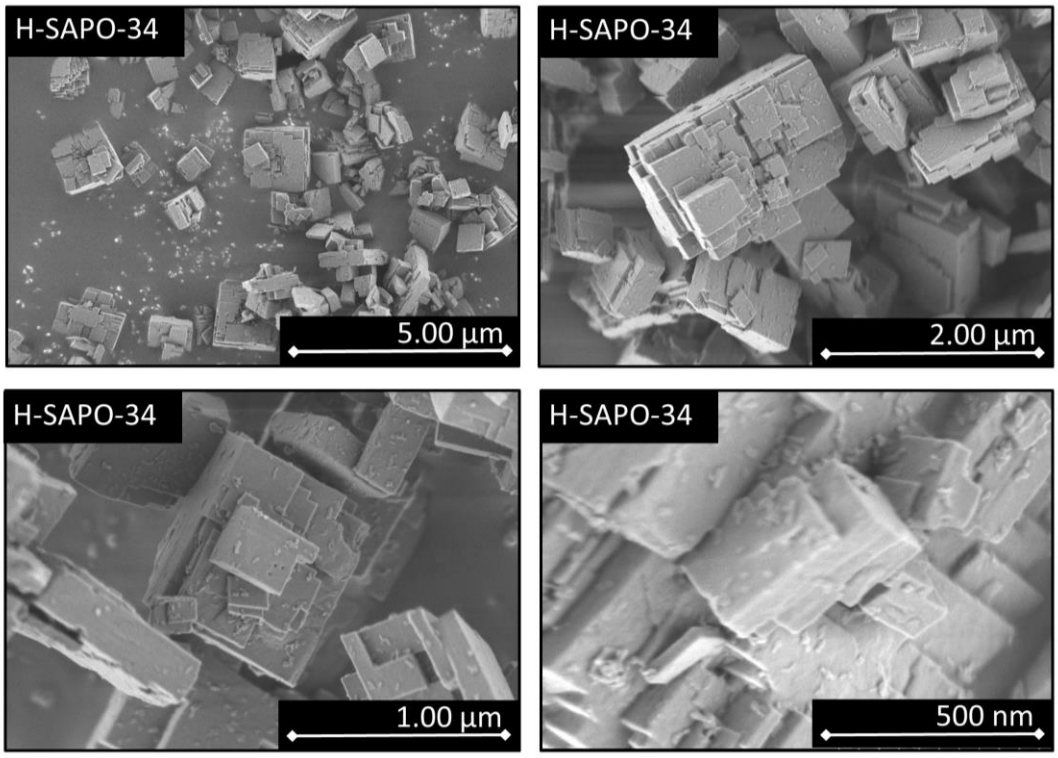

Figure 24. Pictures of the SAPO-34 crystals at different distances.

The crystals have the typical Chabazite structure (cubic), though they seem to have grown as layered plates. This can appear in pure SAPO-34 because of various growth mechanisms in crystals [67], and has most likely to do with the choice of template, as well as the time used for synthesis and aging. According to a study by Smith et al. [68], the layering we see in the SEM pictures suggests it is actually an intergrowth between SAPO-34 and AlPO-18, which will be further analyzed and discussed utilizing PXRD patterns in section 5.2.3.

0.22CuSAPO-34/LIE had a grey color, indicating the presence of CuO nanoparticles in the sample. By examining the material with BSE (Figure 25), bright spots were observed, indicating heavier atoms (in this case; Cu). The other materials made with LIE had a light blue color, and no bright spots were observed when the materials were examined by BSE.

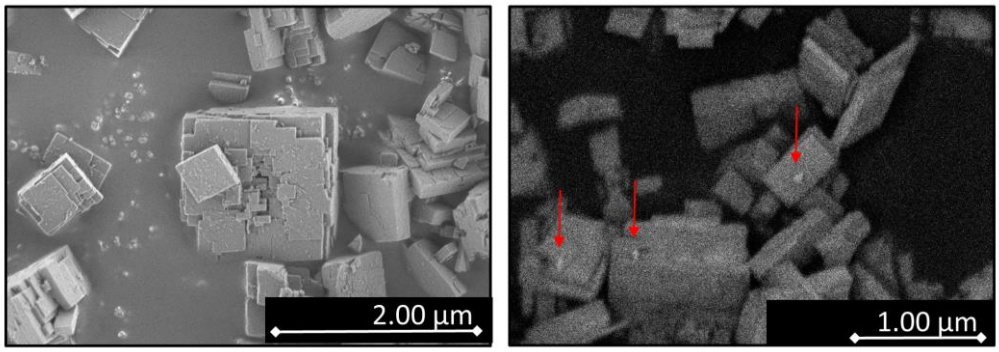

Figure 25. Single crystal of the high loaded LIE sample (left), BSE image of the same material (right). Red arrows indicate CuO nanoparticles.

The solid-state ion exchanged samples had small dark particles mixed in with the light blue-colored SAPO-34. By examining the high loaded material with BSE (Figure 26), it was evident that the material had a high content of CuO-particles. The pure CuO particles were mostly present as large agglomerates, so large in fact, that they were even visible as an extra phase in the SE microscope. However, after collecting a mapping of a single crystal as shown in Figure 27, it is also apparent that in addition to the formation of CuO, due to an intended excess of Cu during synthesis, the Cu had also migrated partially into the pores of the material and was well dispersed in the material. Nevertheless, the total amount of Cu exchanged into the SSIE samples was not quantitative.

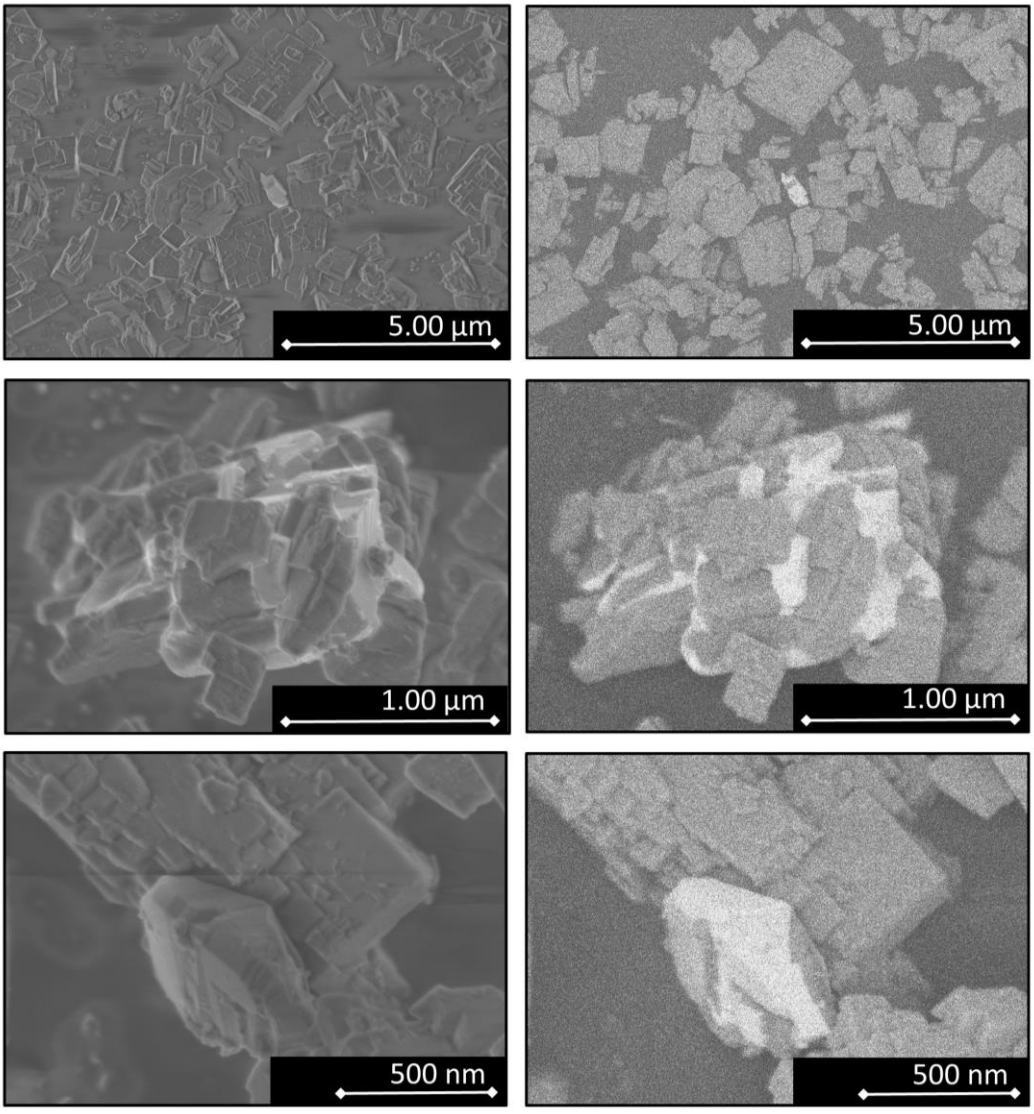

Figure 26. Column on the left are Secondary electron image of the high loaded SSIE sample. Column on the right are the same spots collected with BSE mode. The bright spots indicate CuO-particles.

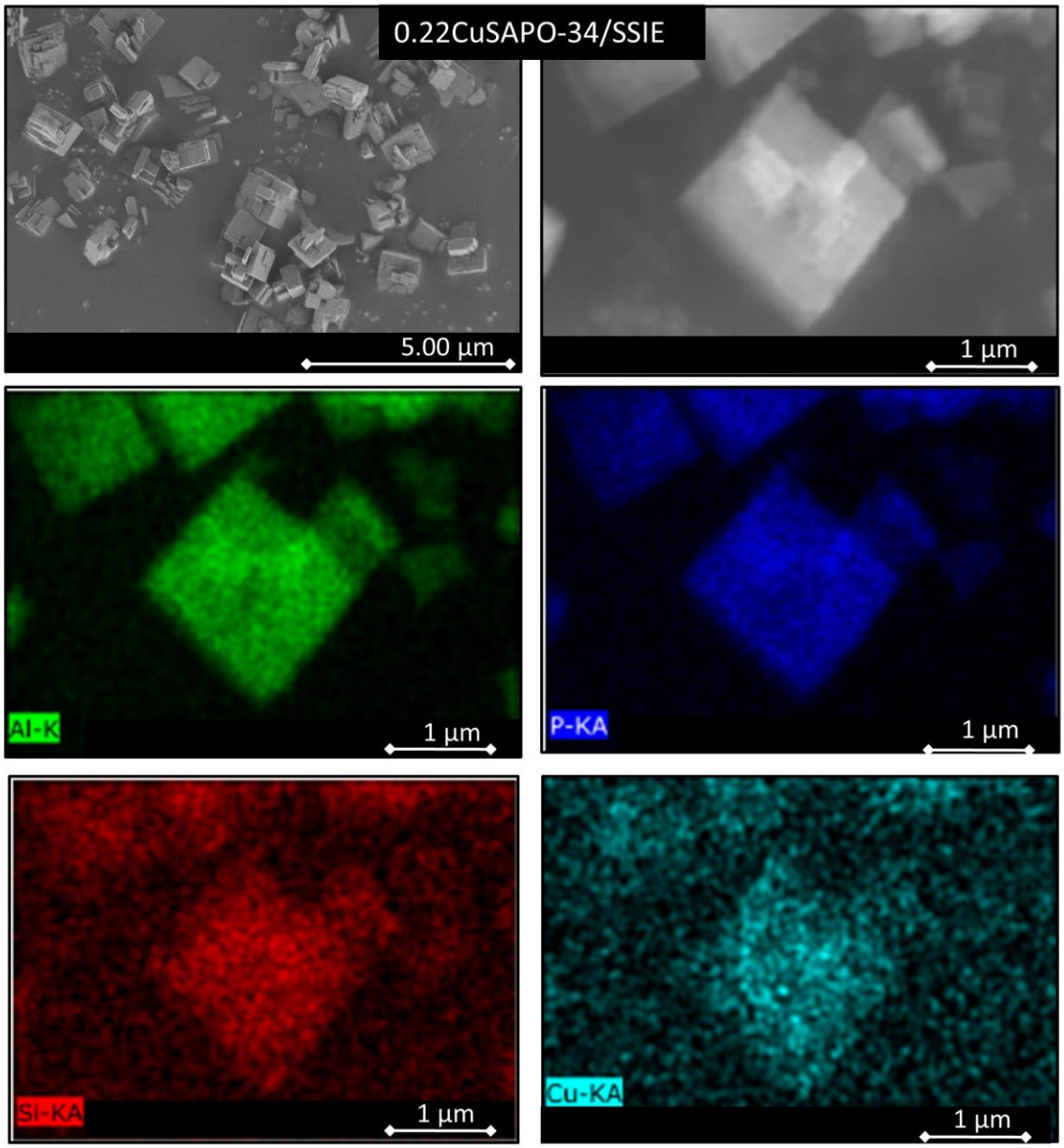

Figure 27. Mapping of a single crystal of the high loaded SSIE material (0.22CuSAPO-34/SSIE).

Elemental analysis was performed on the materials, using energy dispersive X-ray microscopy. With this technique, it was possible to determine the atomic percentage (at%) of P, Al, Si and Cu in the material, which is presented above in Table 6 as the ratios (P+Al)/Si and Cu/Si. The (P+Al)/Si ratio is an important parameter to measure because it indicates the density of acid sites. The (P+Al)/Si ratio of the materials varied between 14 and 15. No variation in this value was expected as a consequence of the various Cu introductions, and the small differences could be caused by inaccuracies in the measuring method. The value obtained for the parent sample was 14.9, which was the value used

throughout this study for all calculations of the stoichiometry. For an ideal material, a (P+Al)/Si ratio of 11 corresponds to exactly one acidic site per cage. However, this might not always be the case for SAPO-materials since the silicon atoms can follow different mechanistic pathways when it is exchanged into an AlPO-framework, as explained in Chapter 2.2.1.

5.2.3 PXRD

Powder X-ray diffractograms were measured for all samples to make sure that the materials had maintained their crystallinity after the various treatments. All of the sample patterns are shown in Figure 28. It is evident that the zeolites did not have the typical pattern that correlates with a pure SAPO-34, and is instead an intergrowth between SAPO-34 and SAPO/AlPO-18. The latter has an AEI framework type, and the structure is very similar to the Chabazite (CHA) framework of SAPO-34, as explained in Chapter 2.2.3. Intergrowth between the two framework types is very common, and is dependent on the synthesis method used, as well as the template [69-70]. The patterns of SAPO-34 and the exchanged materials are shown in Figure 28.The patterns are also compared to two other SAPO-34 diffractograms, made with the same synthesis method [29, 55], in order to determine the intergrowth (Figure 30).

Sławiński et al. [29] found that displacement and growth stacking fault provide different alterations to the PXRD patterns. By comparing the patterns obtained in this work with a thorough refinement they did on an intergrowth material synthesized in the same manner, it is evident that the stacking fault type in the herein materials derive from a displacement type fault due to the very similar shape of the patterns.

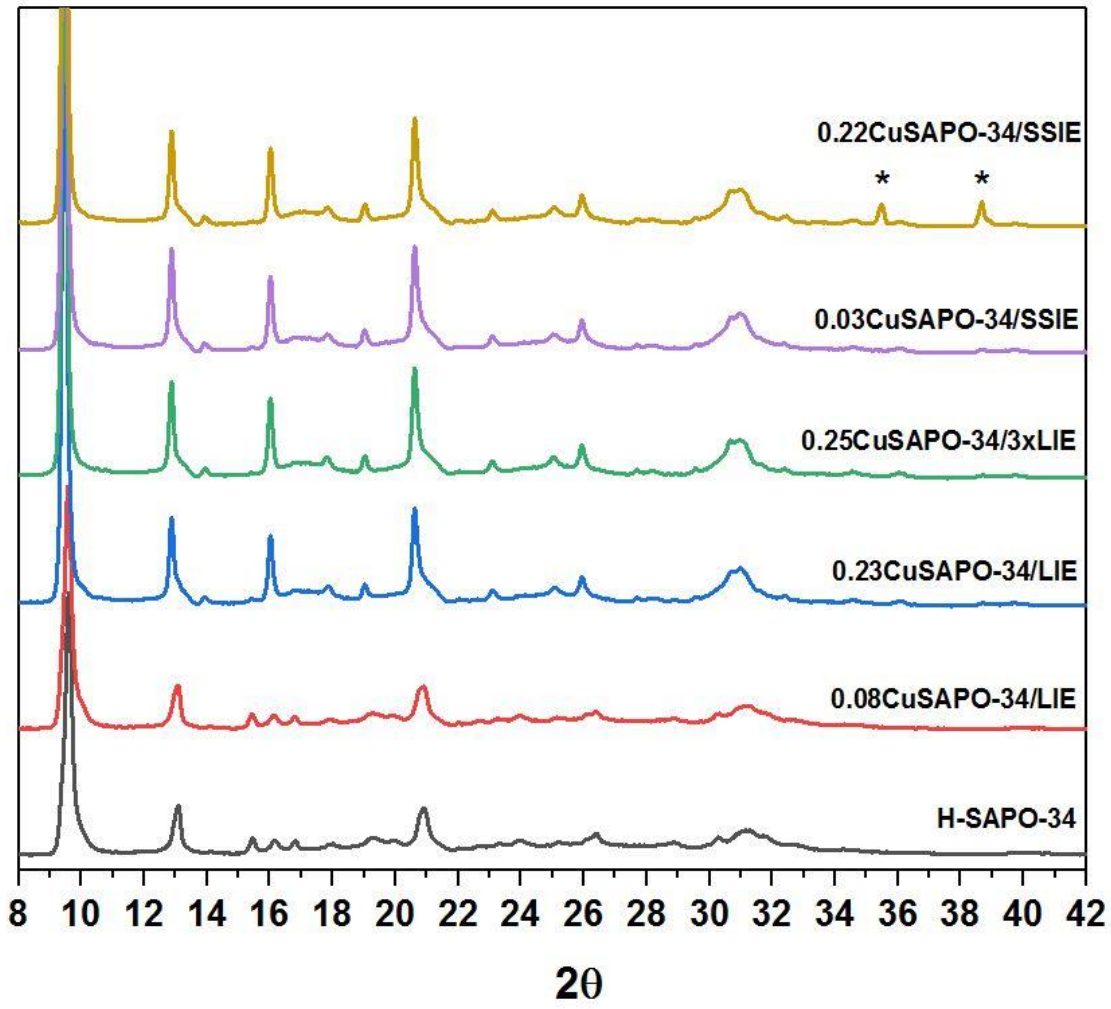

Figure 28. PXRD patterns of the calcined parent material as well as all the Cu exchanged samples. In the high loaded Cu SSIE sample (yellow line), there are two extra peaks at 35.5 and 38.7, which have been assigned to the (-111) and the (111) reflection of CuO. In addition there is also a peak at 15.4 in all the samples, which is probably a minor phase formed during synthesis.

Another interesting observation is that either heat treatment or Cu-content in the ion exchanged materials affected the crystallinity of the crystals to some extent, and restored the collapse of the framework that occurred during template removal. This can be observed from the higher intensities of the peaks in the materials treated with high temperature and/or loaded with high amounts of Cu in Figure 28. The collapse of the framework after template removal can be seen from the lower intensities of the peaks in H-SAPO-34 compared to the as-synthesized material, which is shown in Figure 29.

In all materials, there is one extra peak at 15.4. A peak at this angle is not found in the CHA nor the AEI type structure, and is a minor phase that it was not possible to determine. Since the peak exists in all samples, it is seemingly a minor phase formed during synthesis.

After a peak search, the peak does not seem to correlate to any impurities that could affect the reaction. In the high loaded SSIE sample there are two extra peaks, which from literature can be correlated to CuO from similar studies [41], indicating that the sample has an excess of Cu that was not able to diffuse into the material. This supports the findings from the SEM images above.

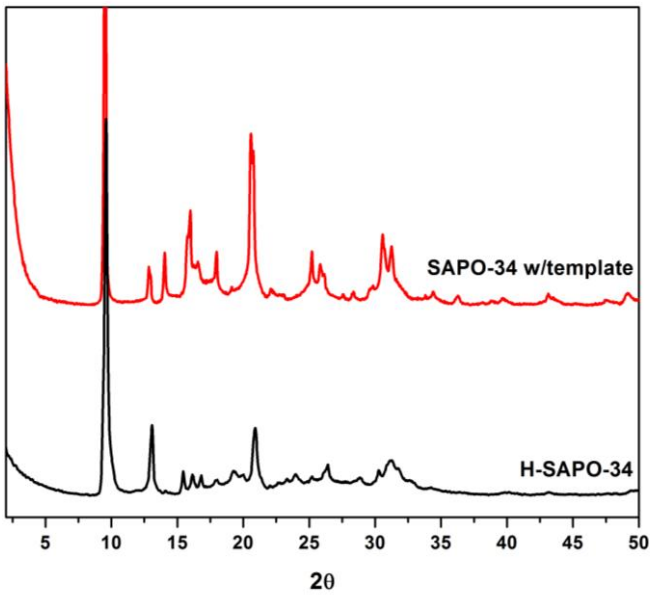

Figure 29. PXRD pattern of the template containing SAPO-34 (red), and the calcined SAPO-34 (black). The decrease in intensity indicates a slight collapse of the framework due to template removal.

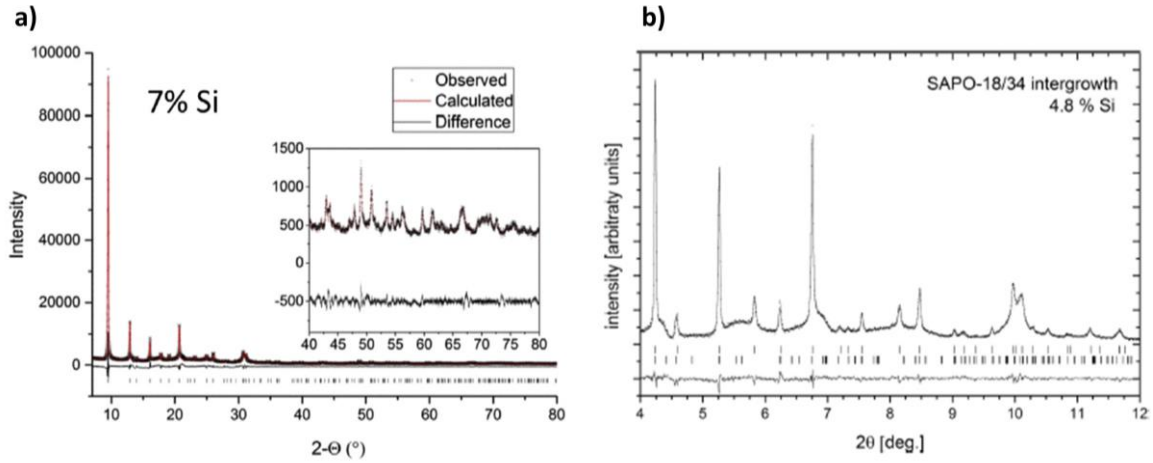

Figure 30. SAPO-34 PXRD patterns for comparison. a) Pawley fit for freshly calcined 7% (left). SAPO-34 at 250 °C. Tick marks indicate Bragg peak positions. The quality of fit at high angles is shown in inset. Figured published in [55]. b) Synchrotron radiation powder diffraction pattern (λ = 0.50575Å) for a 4.8% Si content member of the SAPO-18/34 intergrowth family. The sample is fitted against a structural model with defect free SAPO-34 and an intergrowth phase of AlPO-18. Bragg peak positions are indicated by tick marks below the profile for pure SAPO-34 (top) and AlPO-18 (bottom). The difference curve is shown below the tick marks. Figure published in [29].

5.3 Performance Tests

Following the verification of successful synthesis in that the framework and crystallinity of the SAPO-34 materials remained intact after the Cu-exchange, the materials were evaluated on their performance in the direct methane to methanol conversion. Based on a study by Pappas et al. [11] on Cu-SSZ-13 zeolites, a standard experiment was set as a foundation for the tests used in this study in order to maximize the CH_3OH yield, as explained in Chapter 4.3.2. The optimal conditions reported by Pappas et al. have given the highest methanol yield reported thus far for Cu-Chabazite materials (0.172 mol_{MeOH}/mol_{Cu} (107 μmol/g)). In the article by Pappas et al. [11], a 6 hours methane activation step was used. However, from the results of methanol yield vs methane activation time, it is apparent that the increase in productivity is reaching a plateau after approximately 3 hours. On this basis, we decided to use 3 hours for time efficiency, as the test procedure is rather lengthy and awkward to execute within reasonable working hours.

5.3.1 Standard Tests

Figure 31 illustrates the results of the standard tests. The left graph shows the normalized productivity vs the Cu/Si ratio of the different materials. The graph on the right shows the total yield of methanol of each reaction plotted as a function of the Cu/Si ratio. It appears the methanol yield increases with increasing Cu-loading, which is reasonable due to the increased amount of possible reaction sites in the material. The opposite trend is observed for the productivity, where the amount of methanol is normalized on the Cu-content. In this graph, the productivity decreases with increasing Cu-loading. This shows that an increase of Cu in SAPO-34 is not directly correlated to an increase in active Cu-sites for the direct conversion of methane to methanol. The material with the lowest Cu-content (Cu/Si = 0.03), exhibits a high productivity since it is normalized to the Cu content indicating a higher concentration of active sites. However, it is evident that the yield is low when looking at the graph on the right, due to the low Cu loading. From the materials with a higher Cu loading than the latter, it seemed that the best performing materials were the 0.08CuSAPO-34/LIE, 0.22CuSAPO-34/SSIE and 0.25CuSAPO-34/3xLIE when looking at the yield per gram of sample. At first sight, it was somewhat puzzling that 0.22CuSAPO-34/SSIE performed so well, after proving with SEM/EDX and PXRD that large amounts

of the Cu in this material exists as CuO. However, since the material was made with an excess amount of Cu, and as seen from the mapping in Figure 27, it seems that some Cu has also properly migrated to the exchange sites. A blind test on H-SAPO-34 produced a small amount of CO_x, but no traces of methanol were detected in the effluents. This observation suggests that all CH_3OH produced from the Cu-loaded materials, comes from activated Cu_xO_y. The CO_x produced by H-SAPO-34 most likely comes from methane being physisorbed in the framework, which is then oxidized and desorbed when reacted with water during the extraction step. The CO_x produced from the framework appears to be an explanation for the low selectivity of the Cu-materials. All performance data of the materials are presented in Table A3 in Appendix 7.3.

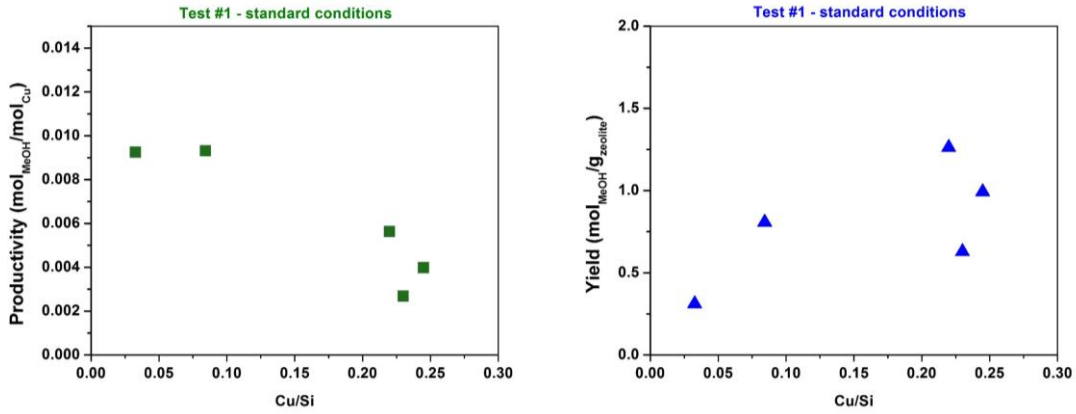

Figure 31. Graph on the left shows the comparison of normalized productivity of all the samples. Graph on the right shows the total yield of methanol obtained from the reaction. The test conditions applied here was O_2 activation @500 °C (8 h), CH_4-dosing @200 °C (3 h), and methanol extraction with 10 % H_2O in Ne/He @200 °C (2 h).

The productivities of all the samples lie between 0.003 – 0.009 mol_{MeOH}/mol_{Cu}. In Figure 32, the performance of the SAPO-34 samples is compared to a similar Cu-loaded SSZ-13, which has a Cu/Si ratio of 0.34, and Si/Al =12. As seen in Figure 32, the Cu-SSZ.13 has a performance that is nearly ten times better than SAPO-34 under the same reaction conditions. Oord et al. investigated a set of Cu–incorporated Na-SSZ-13 for the methane to methanol reaction, with similar weight percentage of Cu introduced, and obtained productivities in the same range as the SSZ-13 material tested in this study (0.03-0.045 mol_{MeOH}/mol_{Cu}). Wulfers et al. studied the performance of a number of small pore zeolites incorporated with Cu for the DMTM-conversion, including SSZ-13 and SAPO-34. The SSZ-13 materials that Wulfers et al. tested also had approximately the same productivity

as the other SSZ-13 materials mentioned (0.03-0.06 mol_{MeOH}/mol_{Cu}). With respect to SAPO-34, they also see a significantly lower productivity. During the *in situ* solid-state ion exchange procedure they performed (presented in chapter 2.3.2), which had a high excess of Cu_2Cl, they obtained a productivity of 0.01 mol_{MeOH}/mol_{Cu}. For their LIE exchanged sample, they obtained a productivity of < 0.001 mol_{MeOH}/mol_{Cu}, which is significantly lower than what was obtained in this study. The process conditions were however, not optimized in this study, as it was a preliminary study to show that it was possible to activate methane over the small pore zeolites.

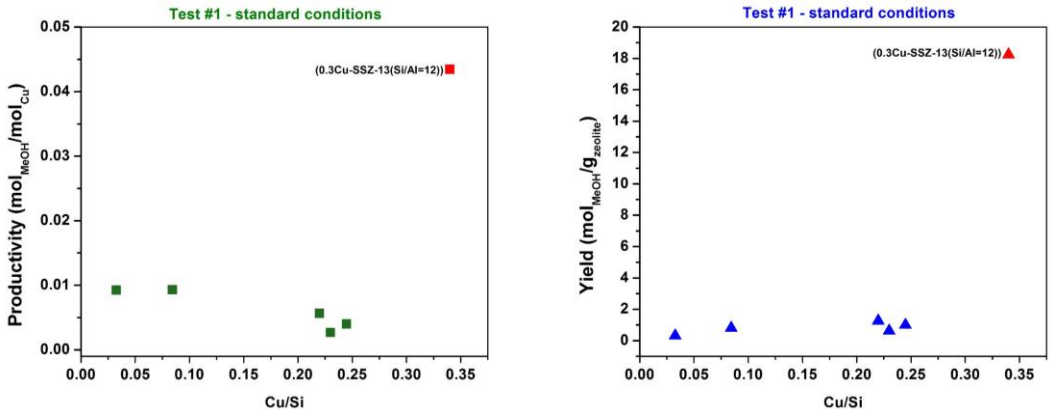

Figure 32. Productivity and yield of SAPO-34 compared with 0.3CuSSZ-13/LIE (Si/Al=12), measured under the same conditions.

This enhanced performance in Cu-SSZ-13 can be attributed to different factors. Most of the framework in SSZ-13 is mainly built from SiO_4 tetrahedra, while SAPO-34 consists of the same structure. However, with Al and P based tetrahedra instead, one possible explanation is that the difference in the polarity of the framework affects the probability of the activation of methane at the Cu-sites. In addition, it may be that the reaction conditions based on optimal conditions for the activation of methane over Cu-SSZ-13 are not facilitating the reaction in SAPO-34. It is also possible that the ion exchange sites are not situated in the same places in SAPO-34 as it is in SSZ-13, which is likely, since the dispersion of Brønsted acid sites in SAPO-34 are more restricted than in SSZ-13. In SSZ-13, two Brønsted acid sites can be separated by one or more Si-atoms. However, in SAPO-34, it is only possible with an odd number of Si-atoms between the acid sites, leading to fewer possible formations of the activated Cu_xO_y moieties in the framework. It is also possible that the Cu-sites formed in the material are inactive in the reaction – either as redox

inactive sites, or as sites that are not able to form methyl groups. This will be further discussed in Chapter 5.5, where the materials were investigated with various spectroscopy techniques.

5.3.2 Normalized Activity

Based on the results above, it was evident that more testing was required to come to any conclusions about the performance of Cu-loaded SAPO-34. Wulfers et al. [41] performed the selective oxidation of methane to methanol over a series of small pore zeolites, including SAPO-34. Here they showed that the methanol was released from the pores much faster in SAPO-34 than in the other materials. This could suggest that the Cu-sites in SAPO-34 do not hold the methyl groups as strongly as in aluminosilicate based zeolites. Therefore, we decided to reduce the temperature of the extraction step in order to see if it would be possible to slow down the reaction and make it possible to detect more of the methanol released from the reaction with the GC-MS. In addition, based on findings from Raman, which will be discussed in section 5.5.2, it could appear that the activated Cu_xO_y moieties are more pronounced at 600 °C compared to 500 °C. Based on these findings, three more test conditions were employed (Figure 33), and tested on the three highest performing materials from the standard conditions. All the results are displayed in Figure 33.

The performance of the three samples during the four different tests are plotted as bars for an easy comparison. The extra point on 0.08CuSAPO-34/LIE in the first test and on 0.25CuSAPO-34/3xLIE in the third test are reproducibility tests performed on the samples. Especially in 0.08CuSAPO-34/LIE, the difference in productivity appears to be significant. However, when the values obtained are so small, even minor changes in the experimental procedure or analysis of the data will have a great impact on the productivity. Based on this, more data points would be necessary to come to any tangible conclusions about the differences in productivity between the samples and tests. Nevertheless, some trends are observed, and are discussed briefly below.

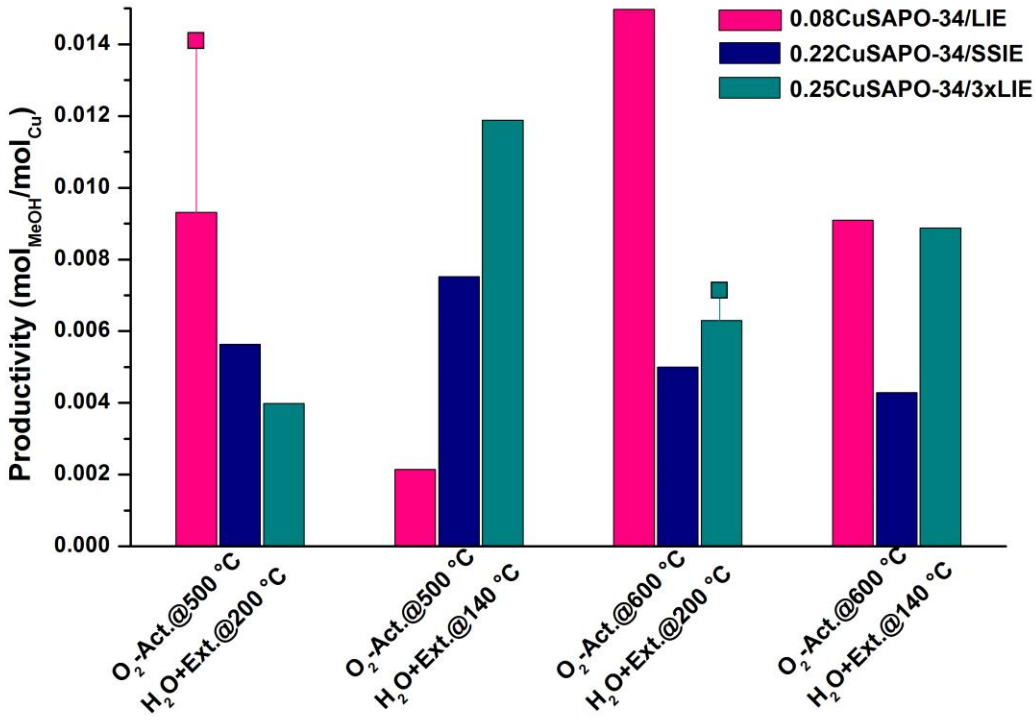

Figure 33. Total normalized methanol yield of 0.08CuSAPO-34/LIE, 0.22CuSAPO-34/SSIE and 0.25CuSAPO-34/3xLIE for different reaction conditions. Test#1 is O_2 activation @500 °C with extraction @ 200 °C, test#2 is O_2 activation @500 °C with extraction @ 140 °C, test#3 is O_2 activation @600 °C with extraction @ 200 °C and test #4 is O_2 activation @600 °C with extraction @ 140 °C. The two points are reproducibility tests performed on two of the materials. The CH_4 loading step was performed at 200 °C for 3 h during all the tests.

From Figure 33 we see that the performance of 0.08CuSAPO-34/LIE was better when the extraction step was performed at 200 °C, while 0.25CuSAPO-34/3xLIE seems to be better performing with an extraction step at 140 °C. 0.22CuSAPO-34/SSIE was the lowest performing material overall when considering the normalized yield of the three samples. It appears that this material was more dependent on the activation temperature, and that the productivity slightly decreased when the activation temperature was 600 °C. Reasons for this will be discussed further in the next section.

5.3.3 Stability Tests

It is important to observe how the materials would behave over multiple reaction cycles. As seen in Figure 33, it is not straightforward which test conditions are the optimal for all

the materials. A more thorough investigation into all sets of parameters would be necessary in order to settle on the optimal conditions. Three consecutive tests over the three best performing materials were performed to evaluate the stability of the samples. For the multiple process cycles, the conditions from test #4 were applied, with activation in O_2 at 600°C (8 h), methane loading at 200 °C (3 h) and H_2O-assisted extraction of methanol at 140 °C (2 h). After each reaction cycle, the materials were kept in a He flow at 160 °C, and then subjected to a new full cycle. 0.08CuSAPO-34/LIE exhibits a slight increase in productivity, as has been observed previously for Cu-exchanged SSZ-13 [11] and MOR materials [9]. 0.25CuSAPO-34/3xLIE seems to lose some of its productivity after the first cycle, before it stabilizes. Last, 0.22CuSAPO-34/SSIE, that overall has proven to be the

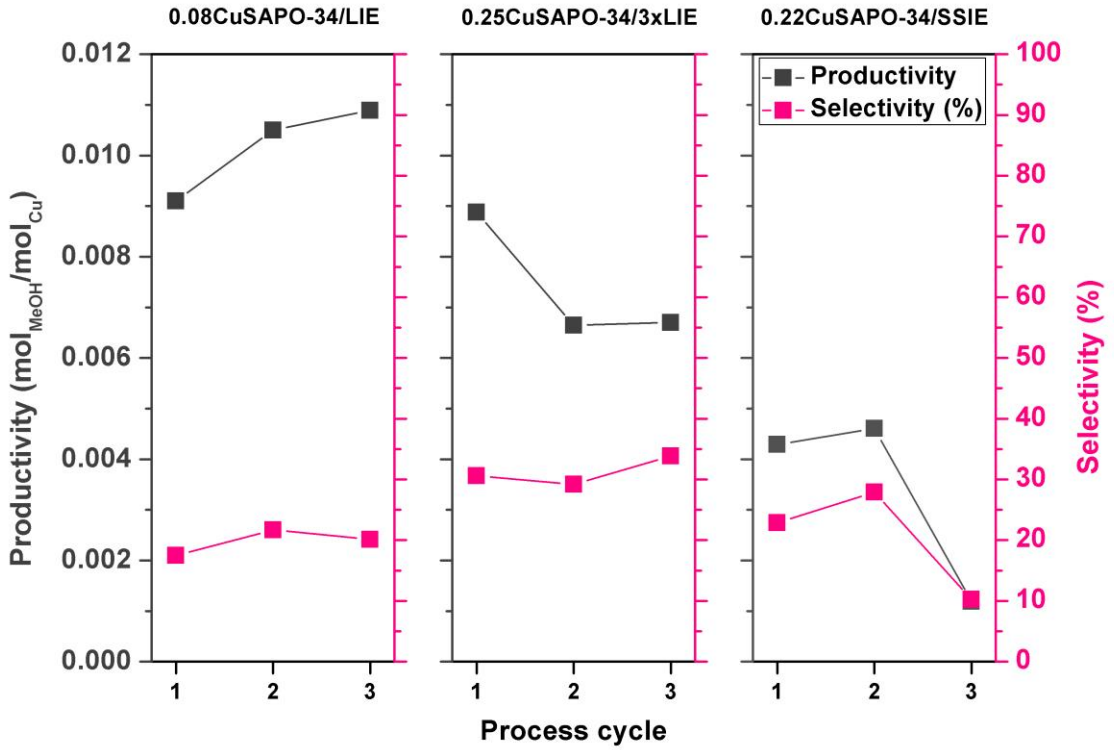

worst performing sample, appears to lose its productivity after the second cycle.

Figure 34. Stability tests of 0.08CuSAPO-34/LIE (left), 0.25CuSAPO-34/3xLIE (middle) and 0.22CuSAPO-34/SSIE (right) performed over three reaction cycles. Activation in O_2 was performed at 600 °C (8 h), Loading of methane was done at 200 °C (3 h), while H_2O-assisted extraction of methanol was performed at 140 °C (2 h). Flushing with He (45 min) was done between each reaction step.

A general trend observed is that the LIE materials have more stable Cu-species, as seen from the decrease in productivity of 0.22CuSAPO-34/SSIE at 600 °C in Figure 33 as well

as the multiple reaction cycles tests (Figure 34). This decline in performance can possibly be attributed to CuO particles in 0.22CuSAPO-34/SSIE that become mobile under the reaction conditions, and migrate inside the pores in such a way that they eventually block the active sites from reacting with methane.

5.4 Spectroscopic Characterization of the Acidity and Framework

SAPO-34 has acid characteristics as a result of the polarizable surface hydroxyl groups and the incorporation of silicon into the framework. When introducing Cu to the framework, the Brønsted acidity should decrease, as Cu ideally replaces protons in the material. There are several different techniques that can be employed in order to investigate the acidity of a zeolite. In this study, FTIR of adsorbed CO at 77K was applied to monitor the change in the OH-stretching region in order to investigate the decrease in Brønsted acid sites. The results and discussion of the CO-stretching region are presented in section 5.5.1 as a part of the discussion on possible Cu_xO_y species in the material. For more acidity characterization, the materials were investigated with FTIR during probing with acetonitrile to get an indication of the density of Lewis and Brønsted acid. Finally, ^{27}Al and ^{31}P MAS-NMR spectroscopy was used to investigate the nuclear environment of the respective nuclei and thus the stability and integrity of the framework at an atomic level.

5.4.1 CO Probing of Acid Sites with FT-IR Spetroscopy

Figure 35 illustrates the –OH stretching region of (a) the parent material, and (b-d) the three Cu-containing samples. The spectra have been normalized to the zeolite framework vibration at 1853 cm^{-1}, and vertically translated for better visual representation. The two bands at 3632 and 3604 cm^{-1} is assigned to two different Brønsted sites (Si(OH)Al) of the materials. Martins et al.[71] showed with deconvolution of the spectra, that there are in fact three peaks in this region. The third band is hidden under the first two at around 3614 cm^{-1}. This band is present in a minor concentration, and are assigned to Brønsted sites situated on the edge of Si-islands in the material, derived from SM3 substitution of Si into the

material [71]. The assumption that this band is present is necessary to assign all features found in the CO-adsorbed spectra. The bands at 3632, 3604 and 3614 cm^{-1} are labeled OH_A, OH_B and OH_C, respectively. The low frequency of the OH_C band is due to perturbation of the proton by hydrogen-bonding interactions with framework oxygen atoms in the six ring windows [71]. OH_A and OH_B are presumed to be unperturbed sites, implicating that their frequencies are only affected by structural and chemical factors of the framework. The intensity of the Brønsted stretching region decreases significantly when Cu is introduced to the framework, indicating that Cu was exchanged with protons to form the Brønsted sites. Comparing the Cu-exchanged samples, it is apparent that the sample with the least amount of Cu also is the sample with highest intensity of the Brønsted acidity, which is reasonable since Brønsted acidity should decrease with increasing Cu loading.

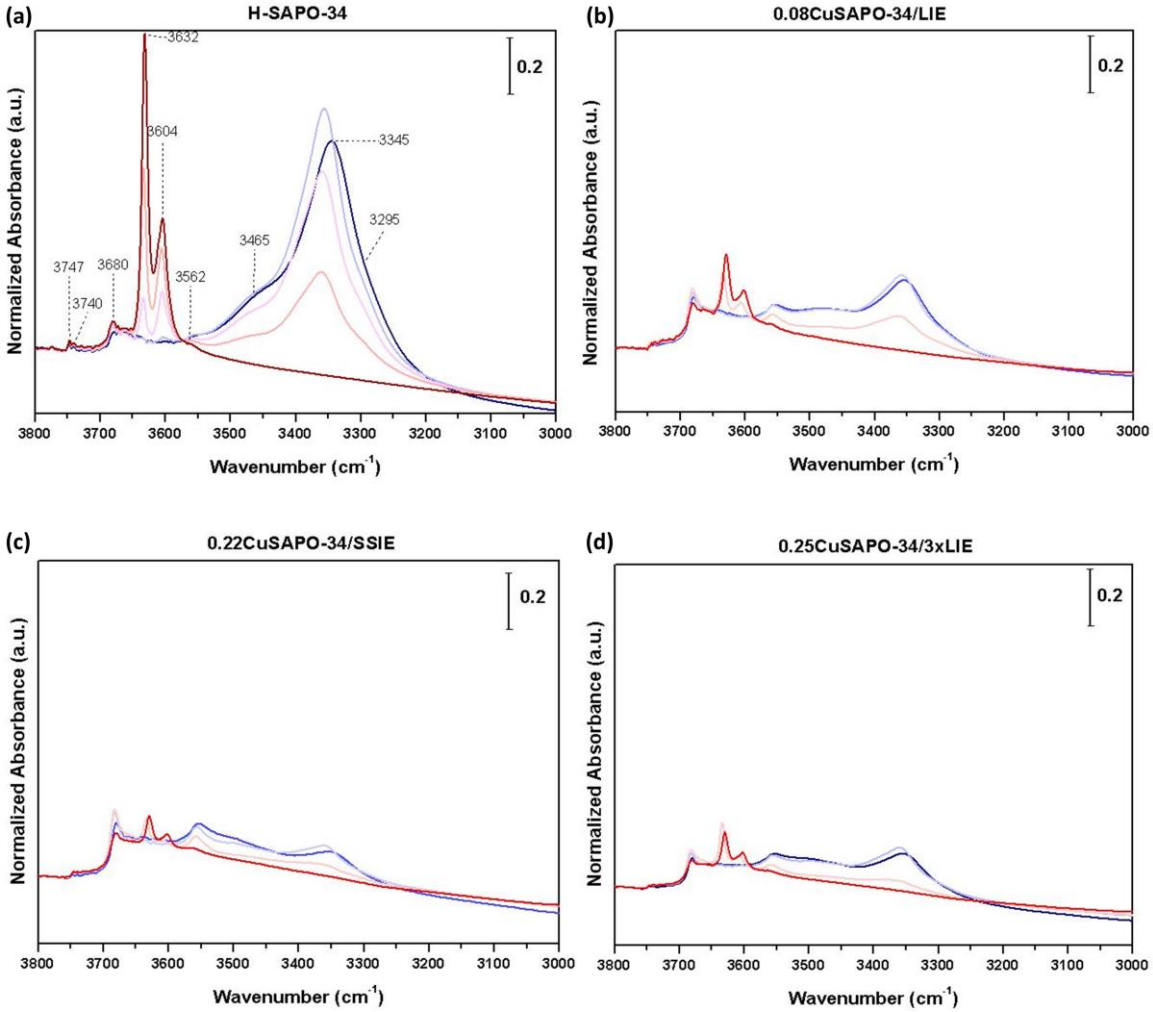

Figure 35. Spectra of the OH-stretching region of (a) H-SAPO-34, (b) 0.22CuSAPO-34/SSIE, (c) 0.08CuSAPO-34/LIE and (d) 0.25CuSAPO-34/3xLIE during desorption of CO at -196 °C.

Upon interaction of CO with the OH vibrations, the OH_B band clearly has the strongest acidic character of the three, with a downward shift of ~319 cm^{-1}. OH_A and OH_C have a milder acidity, with a shift of ~287 and ~139 cm^{-1}, respectively. In the comparison of H-SAPO-34 with the Cu-containing material, a decrease in acidity of the various Brønsted sites was observed. The corresponding values are listed in Table 7.The acidity of the OH_C species decreases the most and appears to be highly affected by the presence of Cu. The small band at approximately 3745 cm^{-1} is the stretching of Al-OH and Si-OH, which are essentially unaffected by the presence of CO. The band at 3680 cm^{-1} is due to P-OH vibrations in the materials. This band appears to be slightly reduced in the presence of CO, and might be correlated to the band appearing at 3562 cm^{-1} with increasing CO-loading. The peak at 3562 cm^{-1} seems to be affected by the presence of Cu in the sample, which is especially apparent in 0.22CuSAPO-34/SSIE. No assignment of the peak observed at 3562 cm^{-1} has been found in literature, and further investigation is required for proper assignment.

Table 7. Overview of all peaks observed in the –OH stretching region of (Cu-)SAPO-34.

CO pressure	ν_{OH} (cm^{-1}) observed for H-SAPO-34	ν_{OH} (cm^{-1}) observed for 0.08CuSAPO-34/LIE, 0.25CuSAPO-34/3xLIE and 0.22CuSAPO-34/SSIE	site	reference
	3745	3745	Si-OH	Akolekar et al. [72]/ Martins et al. [71]
	3680	3680	P-OH	Martins et al. [71]
	3632	3630	Si(OH_A)Al	Martins et al. [71]
	3604	3602	Si(OH_C)Al	Martins et al. [71]
high	3562	3559	shift of P-OH	-
high	3465 (broad)	3478, 3493, 3500 (broad)	shift of Al(OH_C)Si	Martins et al. [71]
high	3345	3353	shift of Al(OH_A)Si	Martins et al. [71]
high	3295	3305, 3315,3315 (sh)	shift of Al(OH_B)Si*	Martins et al. [71]

* Species detected by Martins et al. after performing a deconvolution of the peaks.

5.4.2 Acetonitrile Probing of Acid Sites with FT-IR Spectroscopy

Several bases can be used to probe quantitatively the acid site density of zeolites using FTIR spectroscopy. Among them, NH_3 and pyridine are used extensively. However, with NH_3, it is complicated to differentiate between Lewis and Brønsted acid sites, because of its strong basic character. Pyridine, however, is too bulky to enter the small pores and cavities of SAPO-34 [71]. Therefore, the best choice in this case was acetonitrile [24]. Upon adsorption of deuterated acetonitrile at room temperature and subsequent degassing for 10 min, the bands in the OH-stretch region were completely gone. The depletion of these bands was due to the lone pair-electrons in CN groups interacting with the protons. Since all acid sites appear to be accessible to CD_3CN, it indicates that the pore system, and thus the Cu-sites, should also be accessible for methane to react and methanol to desorb during the DMTM conversion. The adsorption of acetonitrile gives rise to several bands in the 2400 – 2100 cm^{-1} region of the four samples that have been analyzed, and are depicted in Figure 36. The strongest bands at ~2317 cm^{-1} and ~2293 cm^{-1} are caused by CN groups interacting with Lewis and Brønsted sites, respectively [58]. The slight blue shift in the position of the latter band of the two materials with a high loading of Cu is likely due to an overlap of multiple bands, and the fact that it is positioned on the right shoulder of a much stronger band. The Brønsted band of the parent material is positioned at 2293 cm^{-1}, and 0.25CuSAPO-34/3xLIE has the highest shift with a band at 2298 cm^{-1}.

Deconvolution of the spectra were performed to investigate the concentration of the acid sites. These spectra and all related calculations are presented in Appendix 7.6. In order to get a reliable fit when performing deconvolution of the spectra, two additional shoulders were also detected, one at approximately 2283 cm^{-1} and one in the 2251 – 2256 cm^{-1} region. The latter is assigned to asymmetric stretching mode of CD_3 groups, together with a symmetric stretching mode found at 2114 cm^{-1} [24]. The band at 2283 cm^{-1} is assumed to correspond to CN groups interacting with terminal Al-/P-/Si-OH groups or defect sites [58].

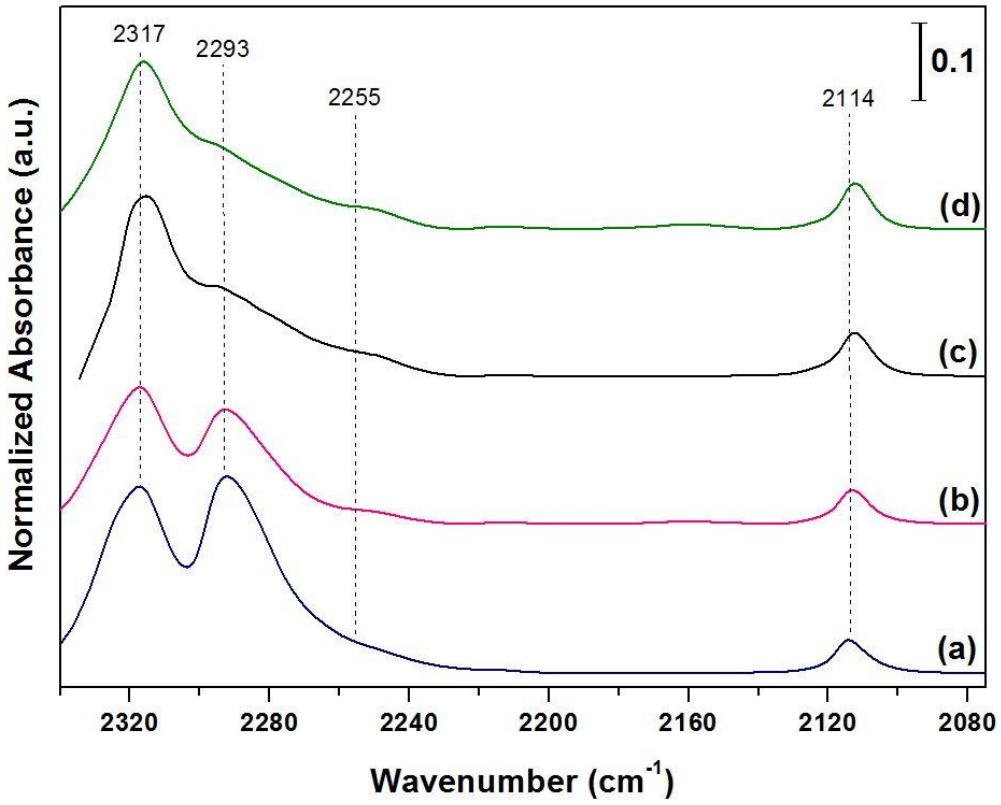

Figure 36. Spectra collected after acetonitrile dosing at RT for 20 min (~20mbar), and degassing for 10 min. (a) H-SAPO-34, (b) 0.08CuSAPO-34/LIE, (c) 0.25CuSAPO-34/3xLIE and (d) 0.22CuSAPO-34/SSIE.

The concentrations of Lewis and Brønsted acid sites are tabulated in Table 8. The concentration values herein will only be discussed relative to each other, because the value of the extension coefficient is questionable, especially evident when Cu present is present, as it can affect the various sites found. Cortés-Reyes et al. [16], have previously performed acetonitrile probing with FTIR on Cu-SAPO-34 samples; they observed a band at ~2328 cm^{-1}, which they assigned to acetonitrile coordinated over Cu ions. In Figure 36, no such bands are seen. However, after degassing, the materials were reheated to 200 °C, and a small band was then observed at 2312 cm^{-1}, which was not present in the parent material. This indicates that the band corresponding to CN groups interacting with Cu are hidden under the large absorbance intensities of CN groups interacting with Lewis and Brønsted acid sites. Because of this, it is apparent that the procedure employed is not precise enough to distinguish between the concentration of Cu-, Lewis and Brønsted sites. Since the Cu seems to have a stronger interaction with acetonitrile, a way to improve the procedure would be to slowly heat the material, and use the spectra from the various temperatures to separate between the different acid sites.

The three Cu-samples appear to have approximately a third of the total acid sites of the parent sample. This could indicate that even though some of the Cu in the materials have Lewis acidity, some of the sites might be blocked due to the presence of CuO agglomerates, or that the various ion exchange treatments have slightly altered the framework.

Table 8. Concentration of Lewis and Brønsted acid sites, determined by FTIR spectroscopy of adsorbed CD_3CN.

	Lewis sites* (mmol CD_3CN/g)	Brønsted sites* (mmol CD_3CN/g)	Total concentration of acid sites (mmol CD_3CN/g)
H-SAPO-34	0.19	0.11	0.30
0.08CuSAPO-34/LIE	0.13	0.06	0.19
0.25CuSAPO-34/3xLIE	0.13	0.09	0.22
0.22CuSAPO-34/SSIE	0.16	0.03	0.19

*The deconvoluted spectra, as well as all calculations used to obtain these numbers are presented in the appendix.

5.4.3 SAPO Framework Investigation by ^{27}Al and ^{31}P MAS-NMR Spectroscopy

Figure 37 shows the ^{27}Al and ^{31}P MAS NMR spectra of the three SAPO-34 samples. In the ^{27}Al spectrum of the templated material, a strong peak is observed at 39 ppm, a broader one at 9 ppm, and a minor peak -7 ppm. In the ^{31}P spectrum of the same material, the strongest peak is observed at -28 ppm, with minor peaks at -13 and -7 ppm. All of these shifts are typical for a TEAOH templated trigonal SAPO-34 [55]. After removal of the template, the peak at 39 ppm (assigned to tetrahedrally coordinated Al) shifts to 35 ppm, and the two other peaks are almost absent. However, there is a very small peak at -10 ppm that is assigned to octahedrally coordinated Al, meaning that these sites are coordinated to two extra water molecules. In the hydrated sample, a very small shift at 15 ppm is visible and a small peak appeared at -13 ppm, which is likely a shift of the peak at -10 ppm. The peak at a chemical shift of 15 ppm is pentacoordinated aluminum atoms (framework Al

coordinated to one water molecule). After template removal, the peak at -28 ppm in the ^{31}P spectrum is shifted to -30 ppm, and is assigned to tetrahedrally coordinated Phosphorous atoms bound to four Al atoms ($P(OAl)_4$) [73].

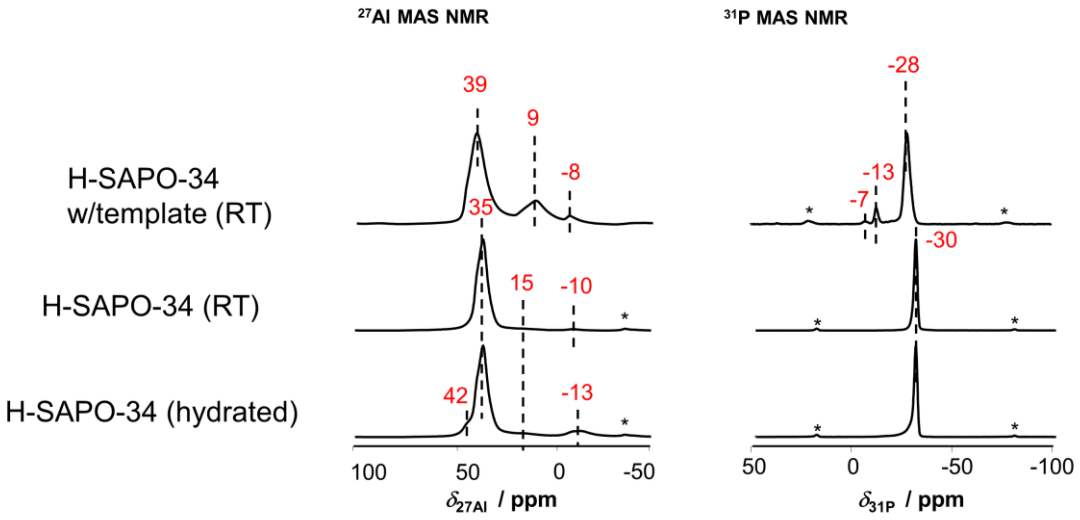

Figure 37. ^{27}Al (left) and ^{31}P MAS NMR spectra (right) of template-containing SAPO-34, H-SAPO-34 and hydrated H-SAPO-34. All spectra are measured at T = 298 K. The asterisks indicate spinning sidebands.

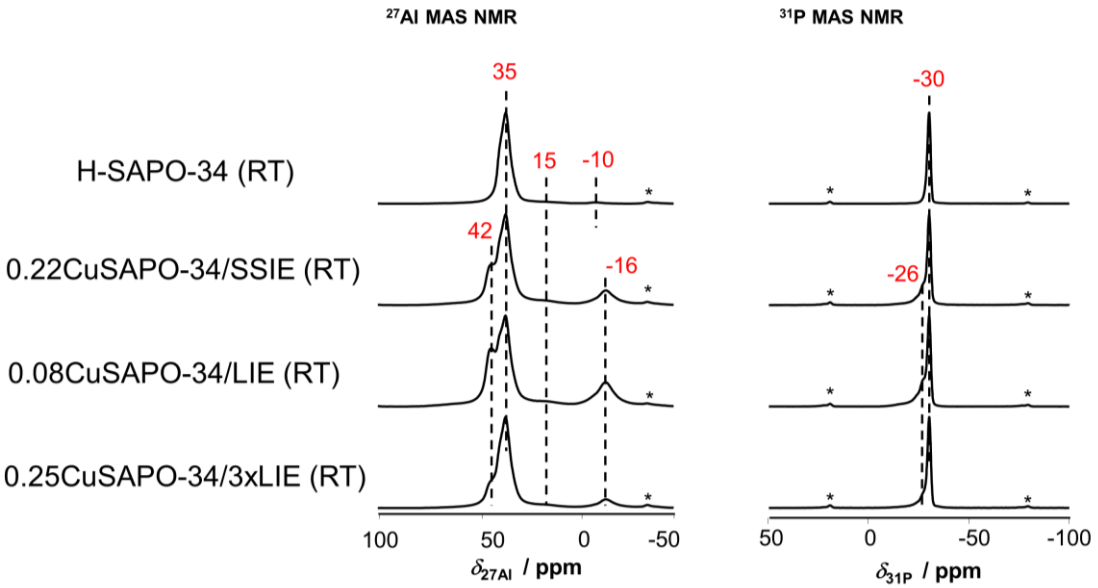

Figure 38. ^{27}Al (left) and ^{31}P MAS NMR spectra (right) of SAPO-34, 0.22CuSAPO-34/SSIE, 0.08CuSAPO-34/LIE and 0.25CuSAPO-34/3xLIE. All spectra are measured at T = 25°C. The asterisks indicate spinning sidebands.

Figure 38 shows the ^{27}Al and ^{31}P MAS NMR spectra of the Cu-loaded samples in comparison to the parent material. In the ^{31}P spectra, there are not a lot of differences, with

the exception of a shoulder at -26 ppm. Since this peak is only present in the Cu-loaded samples, it might be due to a de-shielding effect of P nuclei close to Cu(II)-ions, or coordinated water molecules towards P-O-Al units. The absence of a peak at around -15 ppm suggests that no broken Al-O-P bonds exists in the material even after the various exchange procedures, as suggested by Buchholz et al. [74].

In the ^{27}Al spectra of the Cu-loaded samples, a shoulder at ~ 42 ppm, as well as a broad peak at -16 ppm appears. The peak at -10 ppm, assigned to extra-framework Al, could be hidden under the broad shift at -16 ppm. The broad peak at -16 ppm is assigned to strongly hydrated octahedrally coordinated Al atoms [75], and is most likely a shift of the peak observed at -13 ppm in the hydrated sample due to distortion of the Al from the Cu-environment. When SAPO-34 is fully hydrated at RT, the peak at 35 ppm usually shifts to 42 – 43 ppm due to distorted tetrahedrally coordinated Al [75-76]. Since the materials in this case have been measured post exchange, without any hydration/ dehydration measures taken, they are only partially hydrated which could explain why the shift to 42 ppm only appearing as a shoulder, and not a complete shift of the peak. Buchholz et al. followed the hydration of SAPO-34 from a complete dehydrated state by treating it with steam. They propose that the water first attacks the Brønsted sites in the material, and that the shift from 35 to 43 does not occur until all Brønsted sites have been covered by water [74]. This effect could explain why we do not see this peak in the parent sample at RT, and only see it after the sample has been hydrated. However, since the material with the least amount of Cu also shows the highest intensity of the shoulder at 42 ppm, the shift is most likely affected by the various treatments performed on the samples. Another factor is the different hydration states of the materials, which can be induced by the presence of the Cu in the samples. In fact, Gao et al. [77], has previously proposed that the shoulder at 42 ppm could be due to extra framework Cu^{2+} ions in close proximity to the tetrahedrally coordinated Al. More data is necessary to form any conclusions about this, but at least it appears as though there was no strong damage to the samples after the various treatments, and negligible amounts of extra-framework aluminum in the samples.

5.5 Cu_xO_y Species Characterization

5.5.1 Adsorption of CO on Vacuum-Activated Cu-SAPO-34

By probing the Cu-samples with CO in a controlled manner at RT, it is possible to follow the interaction of CO with Cu^+ sites in the sample and avoid the contribution from Brønsted acid sites, after it has been activated in vacuum at 450 °C. Figure 39 (a-c), shows the evolution of the mono- and dicarbonyl species on Cu. The band evolution at 2153 cm^{-1} is due to the vibration of monocarbonyl adducts ($Cu^+(CO)$). As the amount of CO increases, there is a development of bands at 2176 cm^{-1} and 2148 cm^{-1}, which are assigned to the symmetric and antisymmetric stretching vibration of dicarbonyl adducts ($Cu^+(CO)_2$) [39, 78]. The band at 2135 cm^{-1} is assigned to a $Cu^+(CO)$ stretch in a more constrained environment, while the band at 2111 cm^{-1} is assigned by Bulanek et al. [79] to be the ^{13}CO stretch of the band observed at 2153 cm^{-1}. Bulanek et al. [79] also assigned the two bands at 2135 cm^{-1} and 2111 cm^{-1} to a heterogeneous, dual cationic site in their study of Cu,M-FER zeolites. However, in the case of Cu-H-FER, Bulanek et al. [79] did not observe the band at 2135 cm^{-1}, making it complicated to assign these species observed in SAPO-34 to a dual catalytic site. Although, one could imagine that the two peaks are due to a homogeneous dual site, with two Cu-atoms in close proximity. If this is the case, it could be an indication that multinuclear sites exists in the material, which will be elaborated on later in this section and with complementary techniques in section 5.5.2.

The spectra of the three samples have been normalized to the Cu content of the samples, and it is clear that 0.22CuSAPO-34/SSIE (c) appears to have the ability to host more CO molecules, both as mono- and di- carbonyl adducts. These results suggest that the material made with solid state ion exchange has more accessible Cu(I) species that are under-coordinated by having only two or three oxygen framework neighbors [39]. This type of species are more prone to form the active Cu_xO_y moieties. Still, it is important to keep in mind that 0.22CuSAPO-34/SSIE is made with a different type of ion exchange than the other two, and the correlation between the materials are therefore not straightforward.

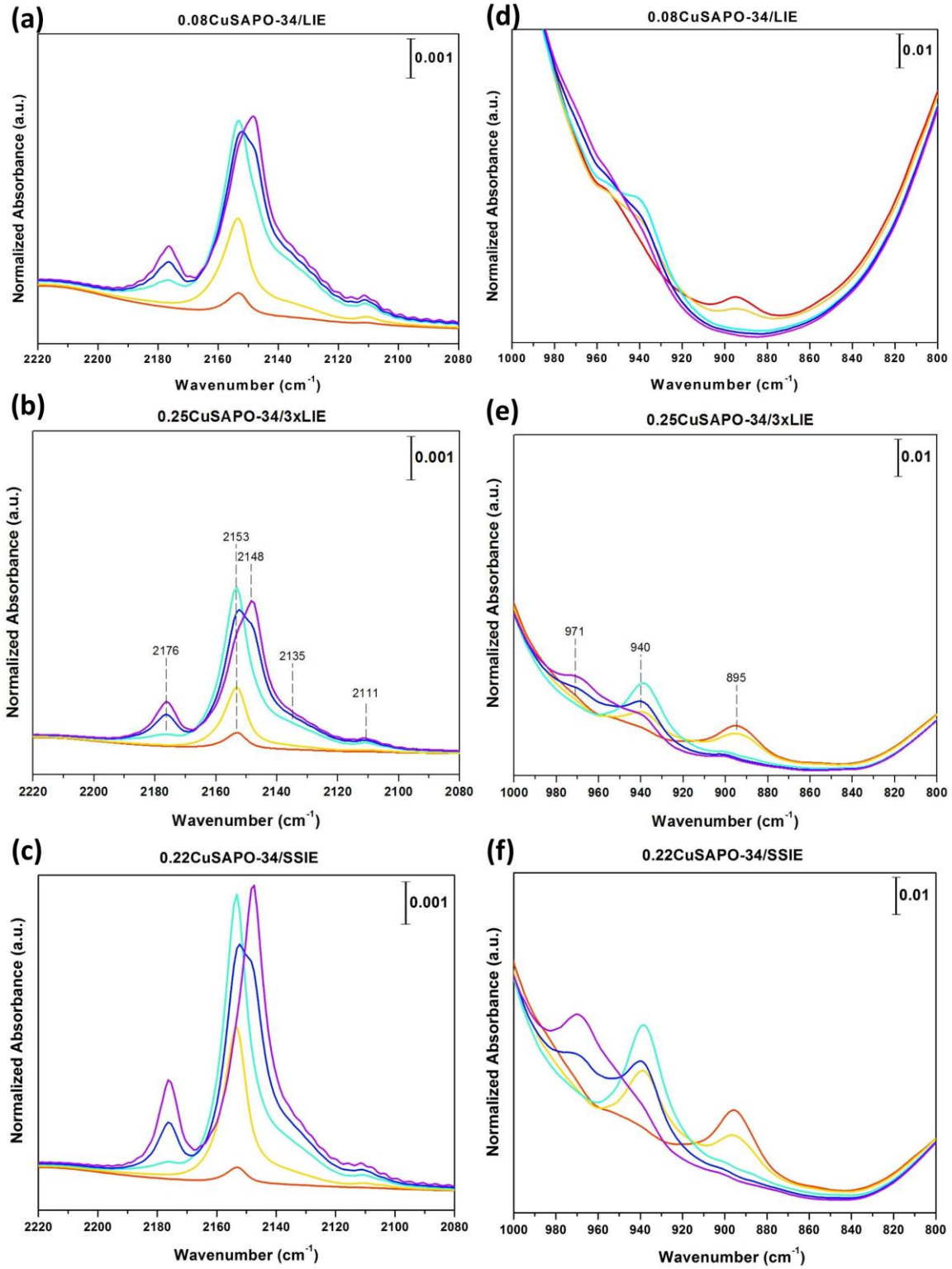

Figure 39. FTIR spectra of the samples 0.25CuSAPO-34/3xLIE (a+d), 0.22CuSAPO-34/SSIE (b+e) and 0.08CuSAPO-34/LIE (c+f) after probing with CO at RT. All samples was first activated at 450 °C in vacuum. For comparison, all spectra are normalized to the framework vibration as well as on the Cu-loading in the samples. (a-c) shows the typical CO-stretching region, where CO interacts with the Cu^{+} sites. (d-f) is from the typical region of framework vibrations, where it is clear that we have contributions from Cu species.

The two LIE-materials appear to be relatively similar. 0.08CuSAPO-34/LIE (a) seems to have slightly higher intensities corresponding to the $Cu^{+}(CO)$ band than 0.25CuSAPO-34/3xLIE (b). However, the $Cu^{+}(CO)_2$ species seem to be more pronounced in 0.25CuSAPO-34/3xLIE. Since 0.08CuSAPO-34/LIE has a lower Cu/Si ratio, these findings could indicate that Cu atoms are more prone to first form sites with a higher coordination to the framework. As the amount of Cu increases, these sites become saturated, and less coordinated Cu sites are formed.

The right column of graphs seen in Figure 39 (d-f) shows the region for T-O-T framework vibrations in the FTIR spectra. Before CO-probing, there is one band at 894 cm^{-1}, which is assigned to Cu^{2+} perturbating the framework in an oxygen bridge as $[Cu\text{-}O\text{-}Cu]^{2+}$ species [80-81]. For these to be present during the experimental conditions, it appears that activation at 450 °C in vacuum is not enough for these species to "self-reduce". This is supported with findings for Cu-MOR materials [82], where it is shown that di-nuclear species are less prone to "self-reduction". As the CO dosage increased, the band at 894 cm^{-1} decreased and a band at 940 cm^{-1} developed, leading to an isosbestic point. The band at 940 cm^{-1} is assigned to isolated Cu^{+} species formation as the CO facilitates the reduction of the $[Cu\text{-}O\text{-}Cu]^{2+}$ species [83]. At higher CO-loadings, a band at 971 cm^{-1} started to appear, which is most likely CO adsorbed on Cu^{+} [80]. When comparing the two LIE materials, it is apparent that the bands are more pronounced in the material with higher Cu content. Indeed, in 0.25CuSAPO-34/3xLIE (e), the higher Cu/Si ratio could facilitate a higher probability of two Cu atoms in close proximity forming a $[Cu\text{-}O\text{-}Cu]^{2+}$ species.

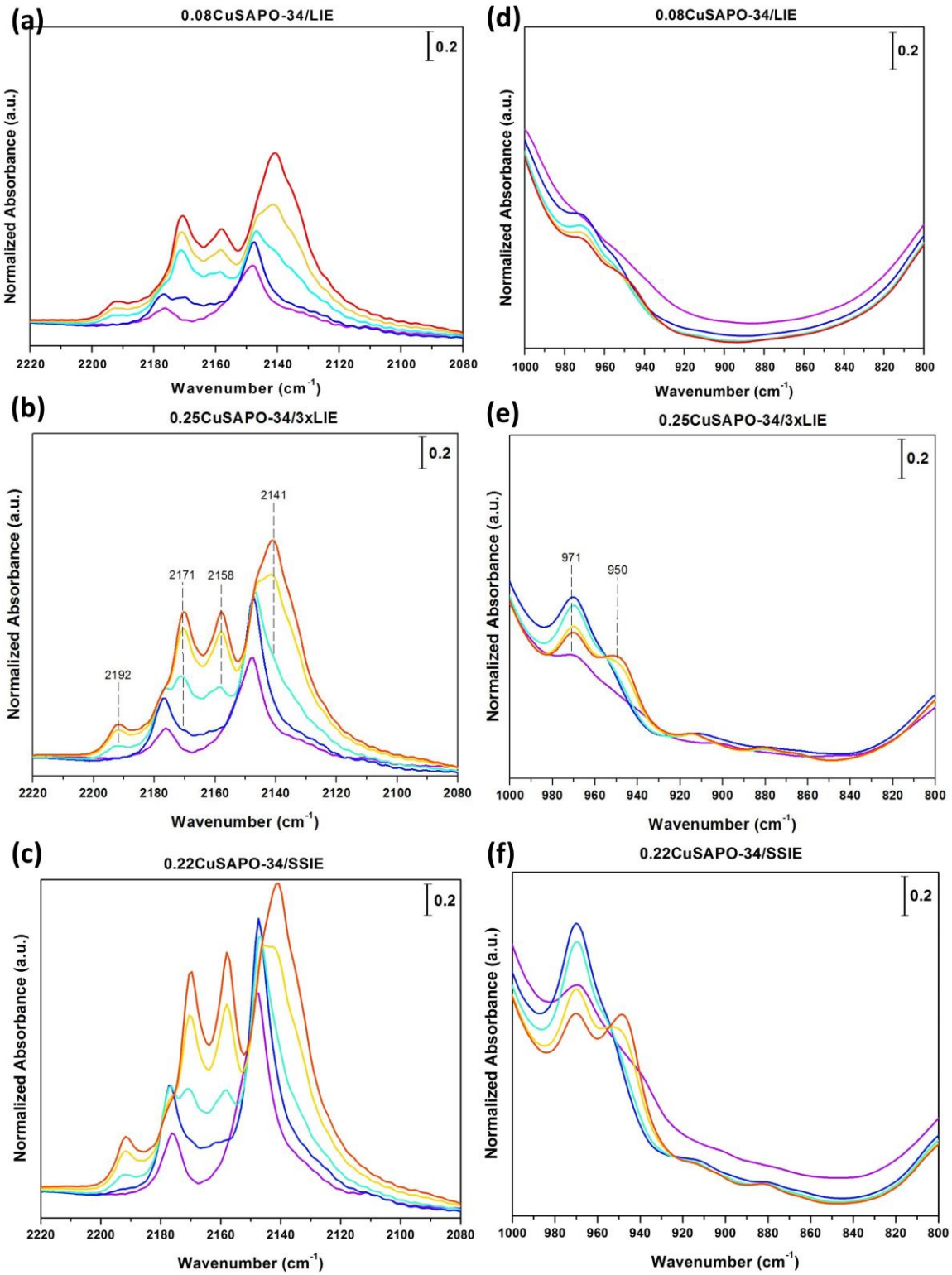

Figure 40. FTIR spectra of the samples 0.25CuSAPO-34/3xLIE (a+d), 0.22CuSAPO-34/SSIE (b+e) and 0.08CuSAPO-34/LIE (c+f) after cooling to -196°C. All samples was purged with ~20mbar of CO before cooling. For comparison, all spectra have been normalized to the framework. (a-c) shows the typical CO-stretching region, where CO interacts with the Cu^{+} sites. (d-f) is from the typical region of framework vibrations, where it is clear that we have interactions from Cu.

After CO probing at RT, the samples were degassed to around 20mbar of CO were left in the cell and cooled down to -196 °C. At this temperature, new features appeared in the CO-stretch region, and are presented in Figure 40 (a-c). Indeed, a band arising at 2192 cm^{-1} due to the formation of $Cu^{+}(CO)_3$ species was observed. In addition, bands at 2171 and 2158 cm^{-1}, which are CO interacting with Brønsted sites and silanols/phosphanols respectively, were also evident [78]. The band that is growing at 2141 cm^{-1} is liquid- like CO interacting with the framework. When comparing the two LIE samples, both the band at 2171 and the one at 2158 cm^{-1} appeared to be more pronounced in 0.25CuSAPO-34/3xLIE (b), than in 0.08CuSAPO-34/LIE (a). At first glance, this was a little puzzling, since the interaction of CO with Brønsted sites should be more pronounced in the material with the lowest Cu/Si ratio. However, as also seen from the acetonitrile experiment, the stretching interaction of molecules adsorbed on the Brønsted sites in 0.25CuSAPO-34/3xLIE appeared to be enhanced in the IR spectra. However, it is hard to clearly deconvolute the contribution of the Cu species and Brønsted sites to the intensity of the peaks, and thus no clear correlation to the acidity can be made.
Finally, in the framework vibration region (d-f), a band at 950 cm^{-1} appears as the material is cooled. This peak is likely due to a blue shift of the isolated Cu^{+} band at 940 cm^{-1} [80].

0.22CuSAPO-34/SSIE (c) has the highest intensity of all peaks in the CO-stretching region, as well as in the region for framework vibrations compared to the LIE samples. Since this material has been made with a different starting compound, as well as the high amount of CuO particles, it is not very likely that this material is more prone to forming the active Cu-sites, as suggested by Pappas et al. [39].

In Figure A11 in the appendix, the spectra from the OH-stretching region in addition to the framework vibration region of 0.08CuSAPO-34/LIE only partially hydrated (300 °C) *versus* the spectra that are fully hydrated (450 °C) are illustrated. The water is gone in the partially hydrated material, but there are still some OH- species left in the material. In the OH region, a band is present at ~3660 cm^{-1} that corresponds to a Cu-OH vibration, indicating the existence of Cu-OH species in the material. In the framework vibration region, the band correlating to $[Cu\text{-}O\text{-}Cu]^{2+}$ at 894 cm^{-1} is missing in the partially hydrated material. This suggests the oxygen is occupied by another species, which in this case is most likely an OH-group. The assignment of Cu- species will be further discussed in the next section.

5.5.2 Raman Spectroscopy

Capillary Measurements – Comparison to SSZ-13

Raman spectroscopy is an excellent technique to use for the detection of Cu_xO_y species in zeolites. This is due to the resonance effect that occurs when the materials interact with a laser in the blue light range of the electromagnetic spectrum. The Raman spectra of the four samples, H-SAPO-34, 0.22CuSAPO-34/SSIE, 0.08CuSAPO-34/LIE and 0.25CuSAPO-34/3xLIE, were collected after being activated in air at 550 °C over night (Figure 41). The two samples with the higher loading of Cu show several bands, neither of which were present in the parent sample, nor in the spectra collected with a red laser (Figure 42), proving the presence of oxygen-activated species. All the bands correlating to the Cu_xO_y species are marked in Figure 41. The strongest band at 549 cm^{-1} is assigned as the symmetric vibration of Cu-O in an end-on superoxo Cu(II) species. The O-O vibration is observed at 1006 cm^{-1}. These bands have earlier been assigned by Solomon and coworkers at 554 and 1043 cm^{-1} respectively [84].

The shoulders at 524 and 589 cm^{-1}, in addition to the band at 812 cm^{-1} are assigned to a $[Cu(trans\text{-}\mu\text{-}1,2\text{-}O_2)Cu]^{2+}$ species by comparison to similar positioned bands found on Cu-SSZ-13 by Pappas et al. and Ipek et al. [11, 85]. Here, the bands at 524 and 589cm^{-1} is assigned to the stretching vibration of the Cu-O bond, while the band at 812 cm^{-1} is the O-O stretching vibration of the peroxide.

The two broad bands observed at a resonance Raman frequency of 314 and 894 cm^{-1} seem to correlate well with a μ-1,1-hydroperoxo-bridged copper dimer. Root et al. [86] have used ^{16}O /^{18}O isotope Raman measurements to assign the bands. The band at 314 cm^{-1} is assigned to the Cu-(O_2H)-Cu metal ligand stretches, while the Raman band at 894 cm^{-1} is assigned as the intra-peroxide stretch of the hydroperoxide bridge. The observation of this hydroperoxo copper dimer supports the observations done with CO-probing in FTIR, that these species are the precursors to the "self-reduction" resistant $[Cu\text{-}O\text{-}Cu]^{2+}$.

Two bands in the Cu-loaded spectra at 265 and 864 cm^{-1} have not been assigned previously in the literature, and would need a deeper investigation, coupled with DFT calculations to be determined. Table 9 summarizes all the assigned bands, as well as values from literature.

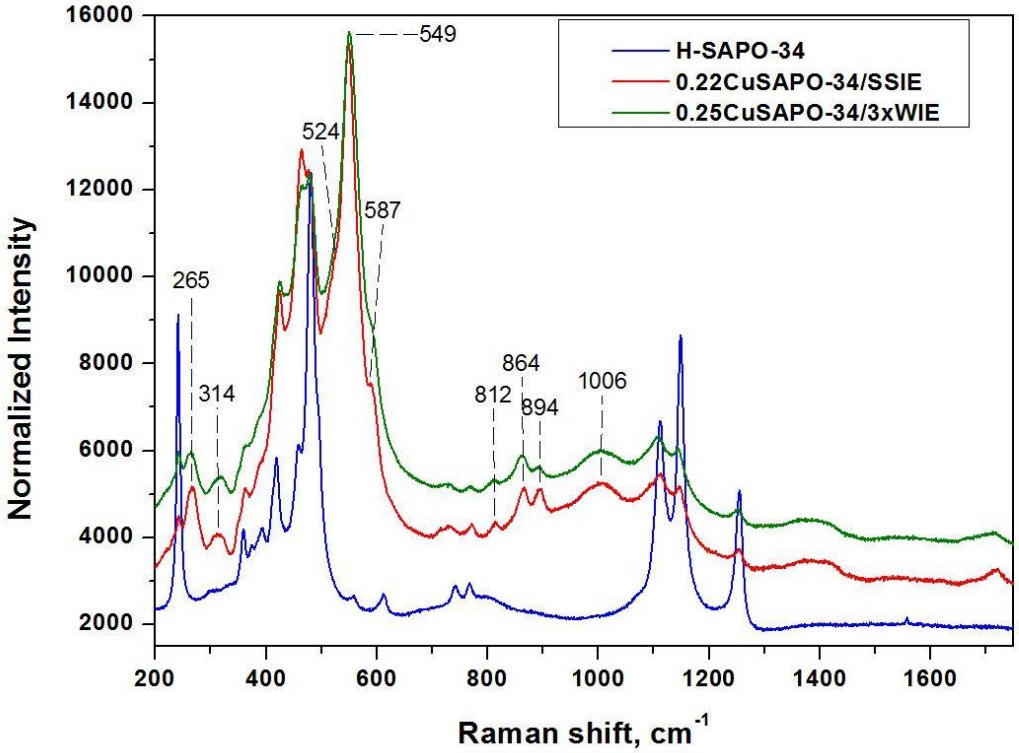

Figure 41. Normalized Raman spectra of samples in capillaries (488nm). The band assignments are for the bands not present in the parent material, and thus related to Cu. The spectra are normalized to the framework vibration at 479 cm^{-1}.

Table 9. Overview of bands correlating to Cu_xO_y species observed in this study, and their comparison to assignments found in literature.

SAPO-34 (this work)	Previously characterized species Ref: [87]	SSZ-13 Ref: [11]	Assignments	
314	322		μ-1,1-hydroperoxo dicopper(II)	
894	892			
524		510	Trans- μ-1,2-peroxo dicopper(II)	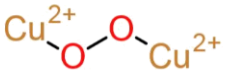
587		580		
812		830		
549	554		Superoxo copper(II) side-on	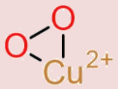
1006	1043			

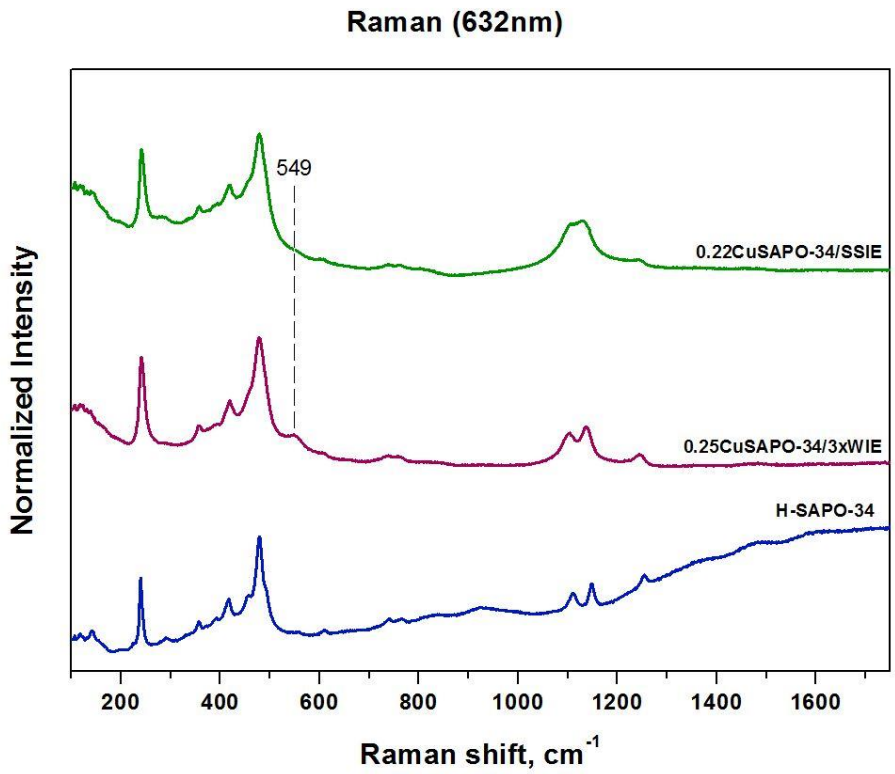

Figure 42. Raman spectra of samples in capillaries (632 nm). The band at 549 is the only Cu-related species observed in the red light range.

As seen in Figure 43, Raman spectra of Cu-SSZ-13 was compared to Cu-SAPO-34. Pappas et al. [11] has already assigned the bands for the Cu-SSZ-13 sample. The bands observed in both SSZ-13 and SAPO-34 are summarized in Table 9 together with band assignments for the other species observed in SAPO-34. The two samples have the same CHA type framework, but from comparing the Raman intensities, it is evident that the Cu-sites in the samples are rather different. As already explained above, the most pronounced band in SAPO-34 is at 549 cm^{-1}, and is assigned to a mono-copper superoxo side-on species. The most pronounced species in Cu-SSZ-13 however, is the trans-μ-1,2-peroxo dicopper species. Pappas et al. suggest that a three-fold coordinated Cu^{II} site may be the most favorable geometric site for methane conversion. This may indicate that the more pronounced species formed in SAPO-34, which has a four-fold coordination, are not as active in the reaction as the species formed in SSZ-13. The TEAOH template used to make SAPO-34 will ideally create one Si atom per cage, while the template used to make SSZ-13 (N,N,N-trimethhyl-1-adamantanamine hydroxide (TMAdaOH) does not have this restriction. This gives the SSZ-13 sample more freedom with respect to the possibility of multiple Brønsted sites to be situated in the same cage, even though the Si/Al ratio is close

to one Al atom per cage. As presented in Chapter 2.2.1, and discussed in section 5.2.2, the Si-islands that may form in SAPO-34 during synthesis *via* the SM3 mechanism can lead to fewer ion exchange sites for Cu, because Brønsted acid sites only form on the edges of the Si-islands. Therefore, it is possible that, in SAPO-34, there are fewer sites available to create the various dicopper species than in SSZ-13. To examine this further, the samples were also investigated with XAS-measurements.

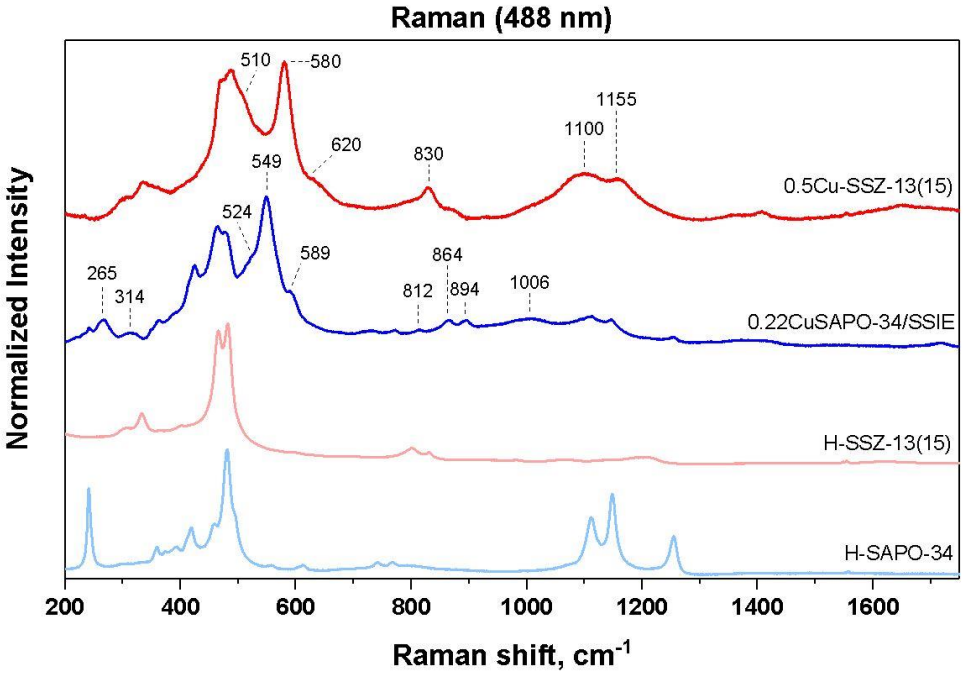

Figure 43. Comparison of SAPO-34 and SSZ-13. The band assignments are only given to the Cu-related bands.

In Situ Raman Measurements

After observing the Cu_xO_y species in the activated capillary-measurements, we decided to investigate further to see if it was possible to follow the whole reaction process with Raman. The *in situ* measurements were conducted in a Linkam cell. The particular setup had a relatively high dead volume around the holder for the material, making it more prone to air leaks and cold spots. Due to the aforementioned factors, the samples had a lot of fluorescence in the spectra when they were heated to higher temperatures making it difficult to detect bands corresponding to Cu_xO_y species. These bands should, in fact, be forming at high activation temperature, and stay present when cooling down to 200°C in O_2, as well

as during purging with He. Then, when CH_4 is being dosed after the He purging step, the CuO species should gradually go away as the methane starts reducing the active sites.

Figure 44 and Figure 45 depicts two spectra acquired after gradually decreasing the temperature from 600°C to 200°C in an O_2/Ar mixture for the two high loaded Cu materials, showing how the most intense band at 549 cm^{-1} were present at 600°C, and then gradually went away when the temperature decreased. Because of thermal induced effects, the bands were broadened, and it is only the most intense bands that were observed at this temperature.

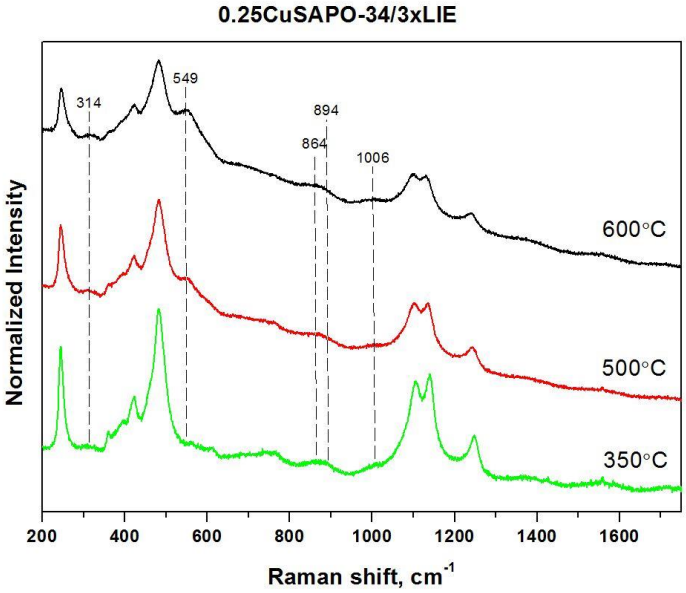

Figure 44. Raman measurements in a Linkam cell. Controlled decrease after activating in O2 at 600 °C.

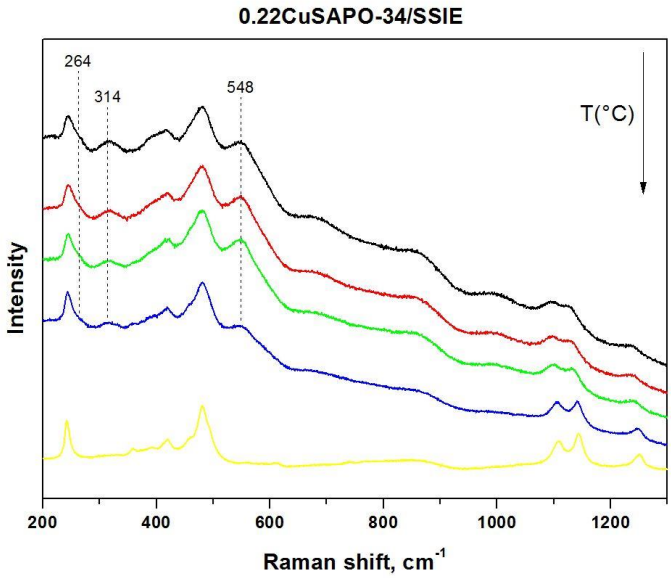

Figure 45. Raman measurements in a Linkam cell. Collection of spectra after activating in O2 at 600 °C with a cooling ramp of 5 °C/min.

Several measures were taken to improve the set-up. A water-trap on the O_2/Ar mixture was installed, as well as increasing the temperature of the heating traces. Even with our best efforts in the limited amount of time, the gas line set-up was a rather complicated system, and we were never able to remove all the water impurities that entered the system. Despite the outcome, the fact that the band at 549 cm^{-1} was observed when cooling down was very interesting. Moreover, the prospects of the technique, when complete control of the set-up is obtained are intriguing.

Since it turned out that the dead volume and impurities had strong influence on the experiment, the employment of a quarts capillary or reactor instead of the Linkam cell is suggested, if one was to follow up on this *in situ* experiment. This way, more control of the reaction over the material would be obtained. In addition, all the gas lines should be separated before arriving at the reactor, to make sure that no impurities from another step interferes with the reaction.

5.5.3 *In Situ* X-Ray Absorption Spectroscopy

In the previous section, the Raman spectroscopy results indicated peaks that corresponded to different three- and four- folded Cu^{II} coordinated species. To study the Cu speciation further, we performed X-ray absorption spectroscopy measurements at the Cu K-edge on the two materials with the highest Cu-loading, 0.22CuSAPO-34/SSIE and 0.25CuSAPO-34/3xLIE. The X-ray absorption near edge spectroscopy (XANES) and extended X-ray absorption fine structure (EXAFS) spectra collected for the two samples are shown in Figure 46. (a) shows the XANES spectra of 0.25CuSAPO-34/3xLIE compared to 0.5Cu-SSZ-13(Si/Al =15), following the same pretreatments. The spectra were collected after pretreatment in He at 500 °C (red) and further exposure to O_2 at 500 °C (blue) and 600 °C (purple). The dotted orange line is He-activation for the Cu-SSZ13 material, and the dotted blue line is further exposure to O_2 at 500 °C for the same material. The inset in Figure 46 (a) shows the FT-EXAFS spectra corresponding to the aforementioned pretreatments. The features observed in the XANES and FT-EXAFS spectra are characterized based on the publication by Borfecchia et al. [2] and Pappas et al. [11], who did in depth analyses of the XAS features of Cu-SSZ-13 samples after different pretreatments. The first feature on the rising edge at around 8983 eV, is assigned to 1s → 4p transitions of Cu(I) ions. The peak

at slightly higher energy (8986 eV), are also 1s → 4p transitions of Cu(I)/Cu(II) ions. The He-activated spectrum shows a highly developed Cu(I) state in Cu-SAPO-34, indicating that the Cu in the material has a high "self-reduction" potential; even more than Cu-SSZ-13. This finding is supported by H_2-TPR experiments, comparing the two CHA-materials by Gao et al. [77]. After the material is contacted with O_2, an important fraction of Cu(I) is reoxidised to Cu(II), as seen by the decrease of the peak corresponding to the 1s → 4p transition of Cu(I) ions, while the peak at higher energy rises, when compared to the He-activated material.

It is only small modifications in the Cu-SAPO-34 spectra when the material is activated in O_2 at 600 °C, but the higher intensity of the first peak at 8983 eV on the rising edge indicates a slightly higher amount of Cu(I) in the system. This could be due to thermal instability of the O_2-derived species that form at 500 °C. In addition, an increase in the white line (WL) is observed after exposure to O_2, and is slightly higher when the material is pretreated at 500 °C, compared to when it is pretreated at 600 °C.

The WL intensity is linked to the average coordination number of Cu [2, 11]. This is in line with the re-oxidation of bare Cu(I) species to Cu(II) containing Cu_xO_y moieties formed after O_2 reaction of the pre-reduced sample, and it appears that more $Cu^{II}_xO_y$ moieties are able to form at 500 °C. The FT-EXAFS spectra of Cu-SAPO-34 shows that the first shell increases when the pre-reduced sample is exposed to O_2. This coincides with the increase of the WL intensity observed in the XANES, as well as development in the second and third shell, indicating the formation of highly coordinated Cu(II) species. However, some Cu(I) remains, even after exposure to O_2. Qualitatively, it seems that there is a higher fraction of Cu(I) species in the SAPO-34 sample compared to SSZ-13 after exposure to O_2. The first maximum in the FT-EXAFS spectra comes from Cu-O single scattering paths, involving two framework (O_{fw}), and extra framework (O_{ef}) oxygen atoms.

The second peak has been assigned to a second shell aluminum atom (T_{fw}) in Cu atoms coordinated to the framework. Cu-SSZ-13 appears to have a higher intensity of the white line (WL) as well as in the first shell. This indicates that Cu-SSZ-13 contains more four-fold coordinated Cu than Cu-SAPO-34.

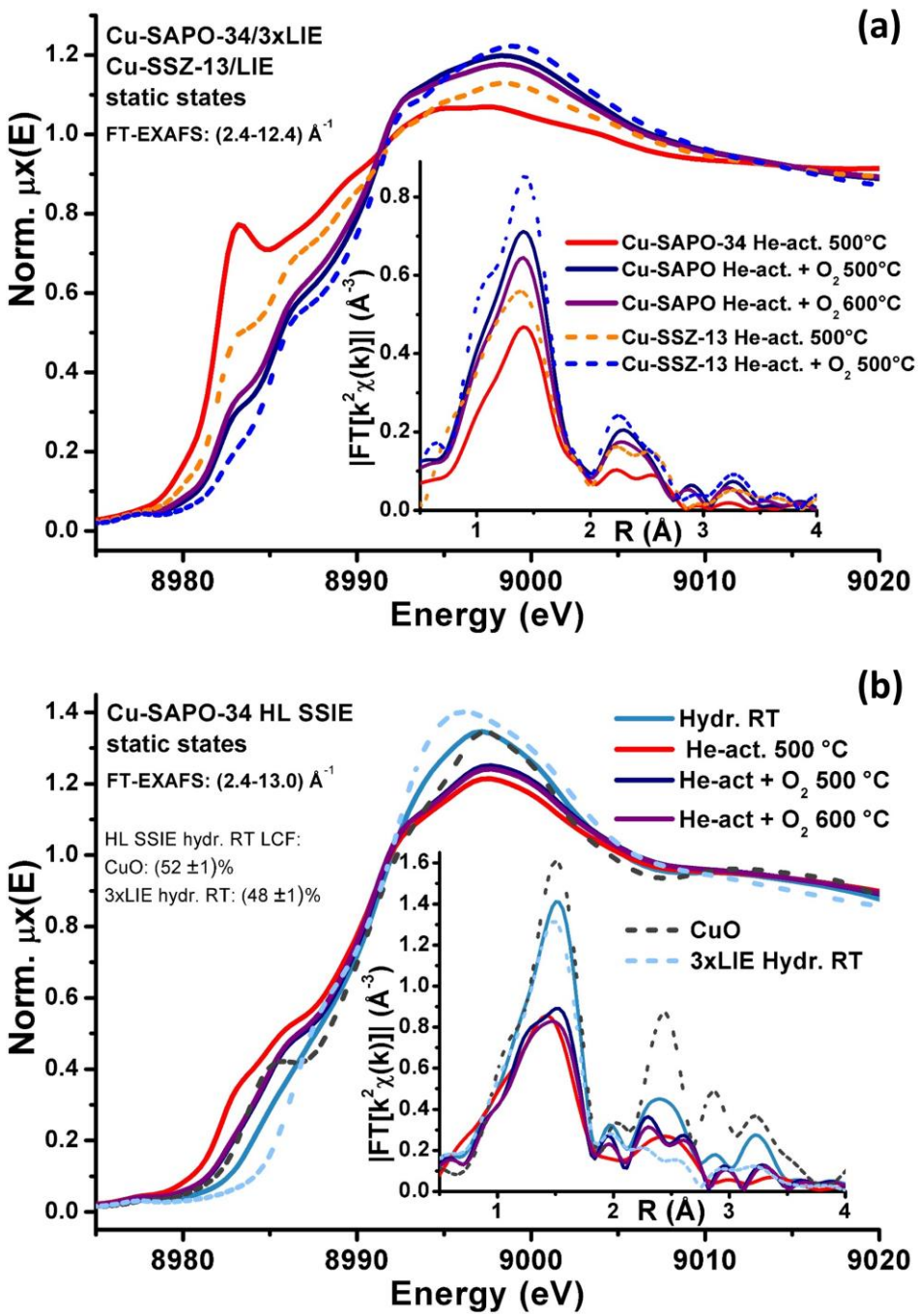

Figure 46. XAS spectra of (a) a comparison of Cu-SAPO-34 and Cu-SSZ-13 after activation of SAPO-34 in He @500°C (red line), O_2 @500°C (blue), O_2 @500°C (purple) and activation of SSZ-13 in He @500°C (dotted orange) and O_2 @500°C (dotted blue). 0.22CuSAPO-34/SSIE (b) is shown in the bottom spectra with the same treatments. The black dotted line is pure CuO for comparison between the hydrated sample of LIE (denoted WIE in the figure) and SSIE.

From the Raman spectra, we found that the most pronounced species in Cu-SAPO-34 was a superoxo Cu(II) species, which is a four-fold coordination, while the high intensity trans-peroxo dicopper species in the Raman spectrum of SSZ-13 is a three-fold coordinated species. This may seem contradictive; however, it is important to keep in mind that a high

Raman intensity does not necessarily correlate to the amount of species, since the Raman intensity is an effect of resonance. In addition, Cu-SSZ-13 contains redox inactive Cu-species, which are four-fold coordinated to the framework located in the 6-membered ring (6mr), where Cu coordinates to O_{fw} from two Al sites which contribute in the first shell and WL intenity [14]. These require two Brønsted sites inside the same 6mr of the framework, separated by one or two Si-atoms. For SAPO-34, it is not possible to have an even number of T-atoms between two Al-atoms, since Si can only exchange with the phosphorous atoms to form Brønsted sites, or in a Si-rich patch, it can exchange with two P, and one Al atoms (see Figure 47 for graphical representation). Therefore, the only possible configuration of two Brønsted sites in SAPO-34 are with one Si atom between the two Al atoms. This kind of species has been shown to be less stable than when the configuration has two Si between the Al atoms [14].

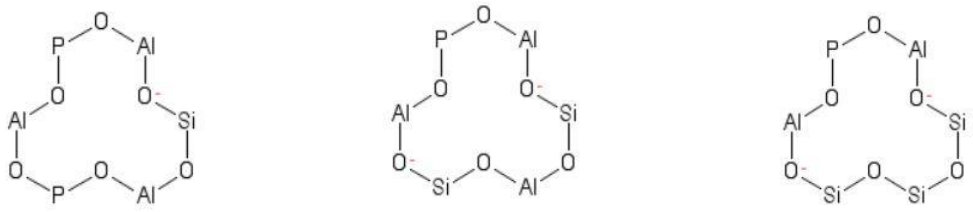

Figure 47. Scheme of possible Si environments in the 6mr of SAPO-34.

XAS measurements were also performed on 0.22CuSAPO-34/SSIE, as presented in Figure 46 (b), but already from the spectra of the hydrated sample collected at RT, it is evident that this SSIE sample had CuO particles in it, as already detected by PXRD. Because of this, it is difficult to directly compare the XANES and FT-EXAFS spectra of the two SAPO-34 materials. Preliminary linear combination fitting (LCF) analysis shows almost 52 % of the total Cu existing as CuO. The activated spectra in He and O_2 follows the same trend as the 0.25CuSAPO-34/3xLIE, but involving only the isolated Cu-components, while the CuO aggregates are most likely to be stable under these reaction conditions. Since so much of the Cu in the sample exists as CuO, it could be an explanation of the poor normalized productivity of the sample. The reason that we do not see the great influence of this in the other characterization techniques applied is because the other techniques mostly focuses on the surface, while XAS probes the bulk of the sample.

6 Conclusions and Further Work

Initially, NH_3-facilitated incorporation of Cu into Mordenites was attempted. Even though this approach was judged to be unsuccessful for the conditions tested in this work, it should be subjected to further investigation. This is due to the prospects of a simple and low temperature setup that can be used as an alternative to the more harsh conditions employed by the solid-state ion exchange method.

SAPO-34 was successfully ion exchanged with Cu, utilizing both a liquid (LIE) and a solid-state (SSIE) ion exchange method. The LIE exchanges were proven to be successful (i.e. to yield well dispersed Cu and no detectable particles) based on the results obtained by SEM/EDX, PXRD, N_2-adsorption and ^{27}Al and ^{31}P MAS-NMR characterization of the materials. The materials made from SSIE were also found to yield well dispersed Cu, however, some CuO agglomerates were detected.

The Cu-exchanged SAPO-34 materials showed the ability to activate CH_4 in a setup for the direct methane to methanol conversion (DMTM). The O_2-activation temperature and the H_2O-assisted extraction temperature were varied to observe the effects of the different conditions on the materials. Cu-SAPO-34 materials exchanged with liquid ion exchange proved to be the most promising candidates for the activation of methane at the process conditions employed as they exhibit a higher yield of methanol per Cu atom. However, it is clear that the performance found for Cu-SAPO-34 here is inferior to that found for aluminosilicates, such as the isostructural SSZ-13.

CO- and acetonitrile FTIR were performed on the materials to investigate the acid sites. These techniques showed that there is a significant decrease in acidity as Cu is incorporated into the materials, proving that Cu had been ion exchanged at the Brønsted acid sites as intended.

The materials were further studied to investigate the nature of the active sites in Cu-incorporated SAPO-34. CO was used as a probe with FTIR spectroscopy to investigate the ability of the materials to form mono-, di- and tricarbonyl species on Cu^{1+}. The materials with the highest Cu-loading had a higher absorbance of multi-carbonyl species, which indicated that a greater amount of lower coordinated Cu-species that are more prone to O_2-activation exists in these materials.

CO-FTIR also showed the existence of a mono-μ-oxo dicopper ($[Cu\text{-}O\text{-}Cu]^{2+}$) species less prone to self reduction. The observation of this species was supported by Raman spectroscopy, where a μ-1,1-hydroperoxo bridged dicopper ($[Cu\text{-}O\text{-}(OH)\text{-}Cu]^{2+}$) species was observed under O_2-activation of the material. This species is assumed to be a precursor for the mono-μ-oxo dicopper species, which forms when the μ-1,1-hydroperoxo bridged dicopper species is exposed to a reducing atmosphere. Mono-μ-oxo dicopper species are found on Cu-SSZ-13 as well, and is believed to be one of the active species in the direct conversion of methane to methanol over Cu-CHA [11]. From the results obtained from Raman, XAS and FTIR, it was also evident that a monomeric end-on superoxo copper(II) species was present in the material. This species has a four-fold coordination, and is possibly a less favorable site for methane conversion.

When comparing the activated Cu-sites found in SAPO-34 materials to coordinated species found to be active in Cu-SSZ-13, it was evident that the Cu_xO_y species that form in SAPO-34 differ from the ones found in SSZ-13. The dissimilarities in activity and Cu species formation of these two materials are likely caused by the obvious differences in the framework composition. The species believed to be the most active in SSZ-13, the peroxo $[Cu(trans\text{-}\mu\text{-}1,2\text{-}O_2)Cu]^{2+}$ species [11] is unlikely to be formed to a high extent in SAPO-34. This is because SAPO-34 has a higher dispersion, as well as fewer Brønsted acid sites for ion exchange to occur, leading directly to a higher formation of monocopper species.

Further contributions to the study of these SAPO-34 materials for the activation of methane in the DMTM conversion would be to perform more reproducibility tests to obtain a better understanding of the structure-activity relationships. A deeper investigation with in situ, as well as operando Raman spectroscopy to investigate which Cu-species are affected by exposure to methane would also be very interesting.

In general, it would be of value to investigate other (Al+P)/Si ratios of SAPO-34 for the reaction, as well as the effect of using other structure directing agents in the synthesis. This might lead to a different distribution of the Brønsted sites, and hence a different environment of Cu species. It could also be important to test different ion exchange procedures, to obtain a higher Cu-content in the materials. Finally, it would also be very interesting to study Cu-SAPO-34 with DFT calculations in particular to compare to Cu-SSZ-13 materials, and to investigate the exchange positions that lead to the most stable configurations in the two CHA-frameworks.

7 Appendix

7.1 Calculations for the Ion Exchange Procedures

Calculations performed to find the amount of Cu(I)O for NH_3-facilitated Cu-incorporation in Mordenite:

Constants used for the calculations:

Material weight: $m_{Mordenite}$

Molar mass of Cu(I)O: $M_{Cu(I)O}$ $(143.0914\ g/mol)$

$Al/g_{Mordenite}$ $(1.39\ mmol/g)$: b_{Al}

Cu/Al = x

First, the amount of Al (n_{Al}) in the weighed amount of Mordenite is found:

$$n_{Al} = m_{Mordenite} \cdot b_{Al}$$

Amount of Cu ($n_{Cu^{1+}}$) is found from the intended Cu/Al ratio:

$$n_{Cu(\mathrm{x})} = n_{Al} \cdot \mathrm{x}$$

$n_{Cu^{1+}} : n_{Cu(I)O} = 2:1$, leading to;

$$n_{Cu(I)O(\mathrm{x})} = \frac{n_{Cu(\mathrm{x})}}{2}$$

$$m_{Cu(I)O(\mathrm{x})} = n_{Cu(I)O(\mathrm{x})} \cdot M_{Cu(I)O}$$

Calculations performed to find the amount of $CuAc_2$ needed for full exchange of the material in the repeated Liquid ion exchange

Constants used for the calculations:

$Si/g_{SAPO-34}$ $(1.033\, mmol/g)$: b_{Si}, calculated from EDX-data (see appendix 7.3)

Material weight: $m_{SAPO-34}$

Molar mass of $CuAc_2$: M_{CuAc_2} $(181.6316\, g/mol)$

Cu/Si = x

First, the amount of Si in the weighed amount of SAPO-34 is found:

$$n_{Si} = b_{Si} \cdot m_{SAPO-34}$$

The amount of Cu ($n_{Cu^{2+}}$) is further found from the intended Cu/Si ratio:

$$n_{Cu^{2+}} = n_{Si} \cdot x$$

$n_{Cu^{2+}} : n_{CuAc_2} = 1 : 1$, leading to;

$$n_{CuAc_2} = n_{Cu^{2+}}$$

$$m_{CuAc_2} = n_{CuAc_2} \cdot M_{CuAc_2}$$

Example of calculations performed to find the amount of $CuCl_2$ needed for solid state ion exchange

Constants used for the calculations:

$Si/g_{SAPO-34}$ $(1.033\, mmol/g)$: b_{Si}, calculated from EDX-data (see appendix 7.3)

Material weight: $m_{SAPO-34}$

Molar mass of $CuCl_2$: $M_{CuCl_2 \cdot 2H_2O}$ $(170.452\ g/mol)$

Cu/Si = x

$$n_{Si} = b_{Si} \cdot m_{SAPO-34}$$

The amount of Cu needed is found from the Cu/Si ratios:

$$n_{Cu(x)} = n_{Si} \cdot x$$

$n_{Cu^{2+}} : n_{CuAc_2} = 1:1$, leading to;

$$n_{CuCl_2 \cdot 2H_2O} = n_{Cu(x)}$$

From the BET calculations, the total pore volume of H-SAPO-34 per gram of zeolite was found (V_{H_2O} $(0.3059 \frac{mL}{g})$), and can be used to find the concetration of $CuCl_2$ ($C_{CuCl_2 \cdot 2H_2O}$) in the solution:

$$V_{H_2O,total} = V_{H_2O} \cdot m_{SAPO-34}$$

$$C_{CuCl_2 \cdot 2H_2O} = \frac{n_{CuCl_2 \cdot 2H_2O}}{V_{H_2O,total}}$$

An excess amount of solution is made (V_{sol}), and is used to determine the mass of $CuCl_2$:

$$n_{CuCl_2 \cdot 2H_2O} = \frac{C_{CuCl_2 \cdot 2H_2O}}{V_{sol}}$$

$$m_{CuCl_2 \cdot 2H_2O} = n_{CuCl_2 \cdot 2H_2O} \cdot M_{CuCl_2 \cdot 2H_2O}$$

The volume of V_{H_2O} is eventually extracted from the solution, V_{sol}, to mix with the weighed amount of SAPO-34.

7.2 Stoichiometry calculations

Table A1. Molar mass and stoichiometric values of the elements in the SAPO-34 material ($A_{x/m}^{m+}[(SiO_2)_x \cdot (AlO_2)_y \cdot (PO_2)_z] \cdot kH_2O$)

	Molar mass (g/mol)	**ratio***
Si	28.085	0.0629
Al	26.982	0.491
P	30.974	0.4462
O	15.999	2**
H	1.008	0.0629***
Cu	63.546	

*Found with EDX analysis of H-SAPO-34.

**This value was not determined by EDX, it was instead determined from the stoichiometric equation in the table description.

***Assuming all Si atoms in the material lead to a Brønsted acid site, the stoichiometric amount of Hydrogen was set equal to the stoichiometric amount of Si.

From the values presented in Table A1, it is possible to calculate the molar mass (g/mol) of SAPO-34 per Si atom in the material;

$$M_{SAPO-34} = \frac{1}{Si_{ratio}} \sum (M_X * X_{ratio})$$

Here, X = Si, Al, P, O and H, M_X is the molar mass and X_{ratio} is the stoichiometric distribution of each of the elements, X.

For calculations related to the ion exchange (presented in the section above), it is necessary to know the amount of Si per gram of zeolite. When the molar mass of SAPO-34 per Si atom is known, it is straightforward to obtain the amount of Si per gram of zeolite (b_{Si});

$$b_{Si} = \frac{1}{M_{SAPO-34}}$$

To obtain the molar mass per Si atom in the ion exchanged materials, the calculations were as follows:

$$M_{Cu-SAPO-34} = M_{SAPO-34} + \left(\left(\left(\frac{Cu}{Si}\right)_{ratio} * M_{Cu}\right) - 1\right)$$

M_{Cu} is the molar mass of Cu, and the $\left(\frac{Cu}{Si}\right)_{ratio}$ is obtained from EDX, and presented in Table A2 for all the materials.

The weight percentage (wt%) of Cu is further calculated from these results:

$$wt\%_{Cu} = 100 \cdot \frac{\left(\left(\frac{Cu}{Si}\right)_{ratio} * M_{Cu}\right)}{M_{Cu-SAPO-34}}$$

Finally, the amount of Cu per the gram of SAPO-34 can be found (b_{Cu});

$$b_{Cu} = \left(\frac{\left(\frac{wt\%_{Cu}}{100}\right)}{M_{Cu}}\right) \cdot 1000000$$

Table A2. Values related to the Cu-content of the ion exchanged materials, needed for calculations of the productivity, presented in Section 4.3.2.

	Cu/Si*	**Molar mass (g/mol)**	**Wt% Cu**	**Cu (µmol/g)**
H-SAPO-34		968.151	-	
0.08CuSAPO-34/LIE*	0.084	972.508	0.55	86.7
0.23CuSAPO-34/LIE	0.230	981.763	1.49	234.2
0.25CuSAPO-34/3xLIE	0.245	982.709	1.58	249.1
0.03CuSAPO-34/SSIE	0.033	969.225	0.21	33.7
0.22CuSAPO-34/SSIE	0.220	981.122	1.42	224.1

*Found with EDX analysis of the materials.

7.3 Performance tests analysis

The yield of X obtained from the formulas presented in section 4.3.2 is plotted against TOS, so that the integrated area can be substracted as the total yield of the product X. An example of this integration is given in Figure A1. All performance data obtained for (Cu-)SAPO-34 is presented in the table below.

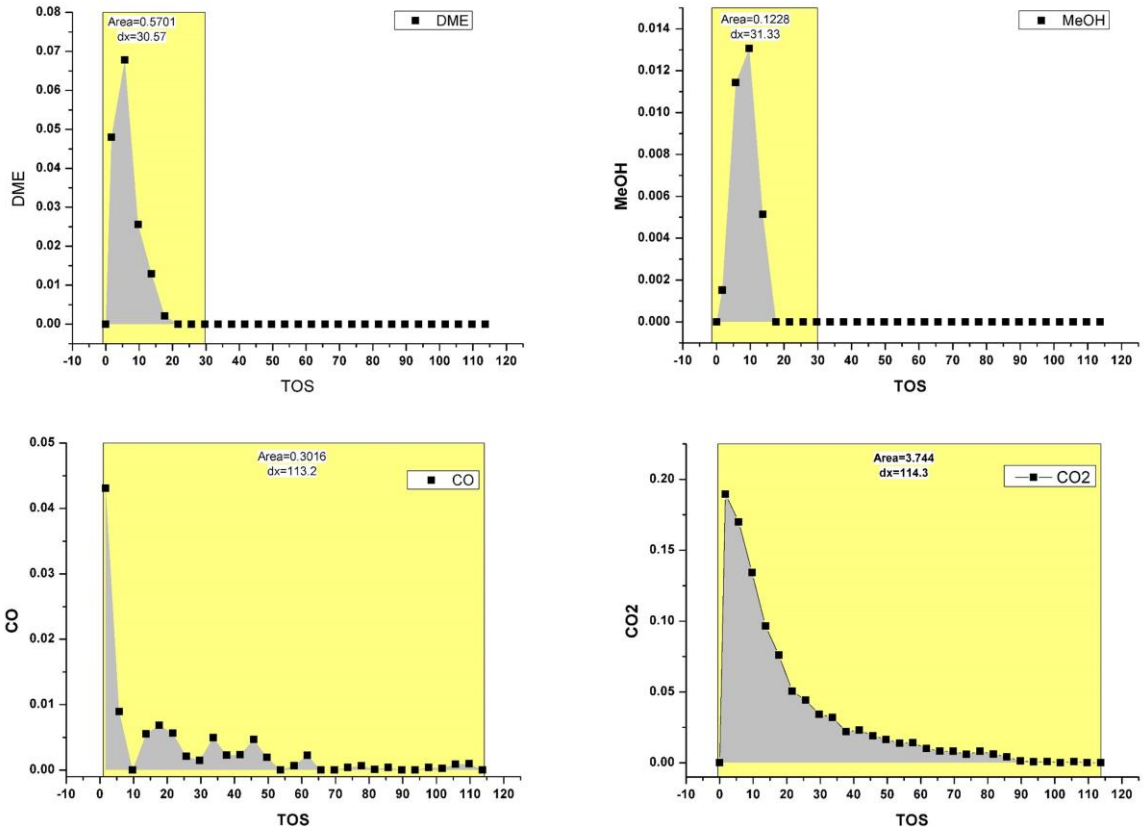

Figure A1. Integration of the products obtained after performing the standard test on 0.22CuSAPO-34/SSIE. The Area is the yield of the products per mass of the zeolite ($\mu mol_x/g_{zeolite}$).

Table A3. Performance data of all samples tested in this thesis. Test #1 is

	Test conditions	MeOH (μmol/g)	CO_x (μmol/g)	Selectivity (%)	Productivity (mol_{MeOH}/mol_{Cu})
H-SAPO-34	O_2@500°C(8h)/H_2O-ext.@200°C(2h)	-	3.20	-	-
0.08CuSAPO-34/LIE*	Same as above	1) 0.81 2) 1.22	1) 3.81 2) 3.32	1) 17.5 2) 26.8	1) 0.009 2) 0.014
0.23CuSAPO-34/LIE	Same as above	0.63	3.71	14.5	0.003
0.25CuSAPO-34/3xLIE	Same as above	0.99	7.13	12.2	0.004
0.03CuSAPO-34/SSIE	Same as above	0.31	5.49	5.4	0.009
0.22CuSAPO-34/SSIE	Same as above	1.26	4.04	23.8	0.006
0.3CuSSZ-13(12)	Same as above	18.25	12.08	60.2	0.043
0.08CuSAPO-34/LIE	O_2@500°C(8h)/H_2O-ext.@140°C(2h)	0.19	2.29	7.5	0.002
0.25CuSAPO-34/3xLIE	Same as above	2.96	7.54	28.2	0.012
0.22CuSAPO-34/SSIE	Same as above	1.69	3.28	33.9	0.008
0.08CuSAPO-34/LIE	O_2@600°C(8h)/H_2O-ext.@200°C(2h)	1.30	3.67	26.1	0.015
0.25CuSAPO-34/3xLIE*	Same as above	1) 1.57 2) 1.77	1) 4.69 2) 4.25	1) 25.1 2) 29.4	1) 0.006 2) 0.007
0.22CuSAPO-34/SSIE	Same as above	1.12	3.59	23.8	0.005
0.08CuSAPO-34/LIE**	O_2@600°C(8h)/H_2O-ext.@140°C(2h)	a) 0.79 b) 0.91 c) 0.94	a) 3.73 b) 3.28 c) 3.74	a) 17.5 b) 21.7 c) 20.1	a) 0.009 b) 0.011 c) 0.011
0.25CuSAPO-34/3xLIE**	Same as above	a) 2.21 b) 1.66 c) 1.67	a) 5.01 b) 4.01 c) 3.26	a) 30.6 b) 29.2 c) 33.8	a) 0.009 b) 0.007 c) 0.007
0.22CuSAPO-34/SSIE**	Same as above	a) 0.96 b) 1.03 c) 0.27	a) 3.24 b) 2.67 c) 3.74	a) 22.8 b) 27.9 c) 10.2	a) 0.004 b) 0.005 c) 0.001

*test performed two times for reproducibility test.

**test performed as a continuous cycle of three runs, (a), b) and c)), to investigate the stability of the materials.

7.4 Calibration Factors of MeOH, DME, CO and CO_2

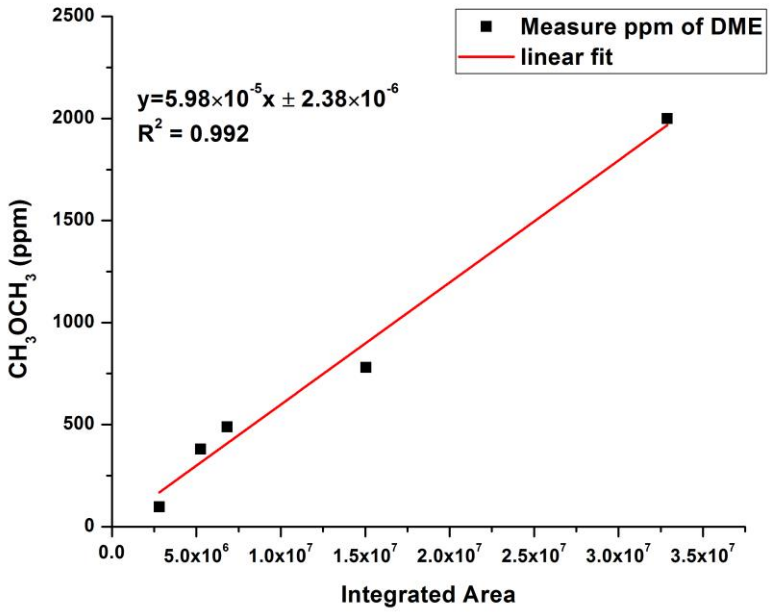

Figure A2. The slope of the linear fit is the calibration factor of DME used in the calculations above. The slope is obtained by plotting the ppm values dosed against the integrated area observed in the mass spectrometer of the GC-MS.

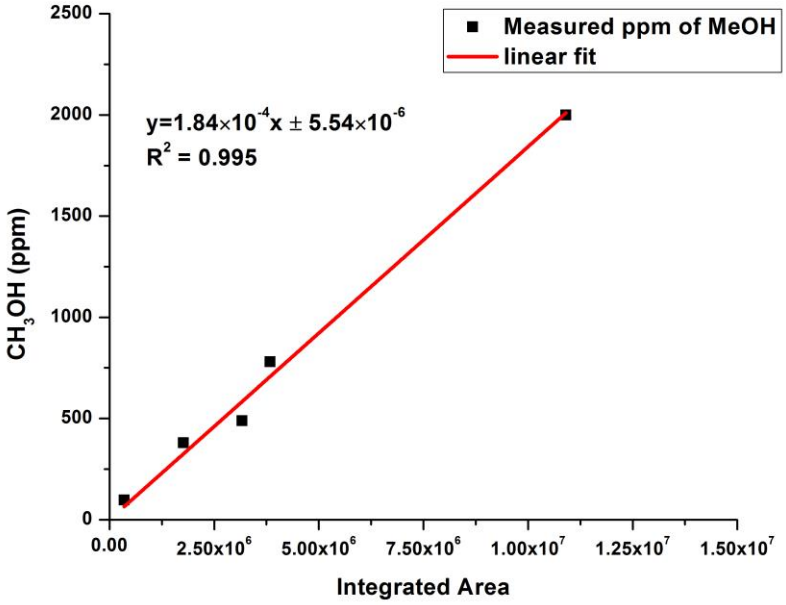

Figure A3. The slope of the linear fit is the calibration factor of MeOH used in the calculations above. The slope is obtained by plotting the ppm values dosed against the integrated area observed in the mass spectrometer of the GC-MS.

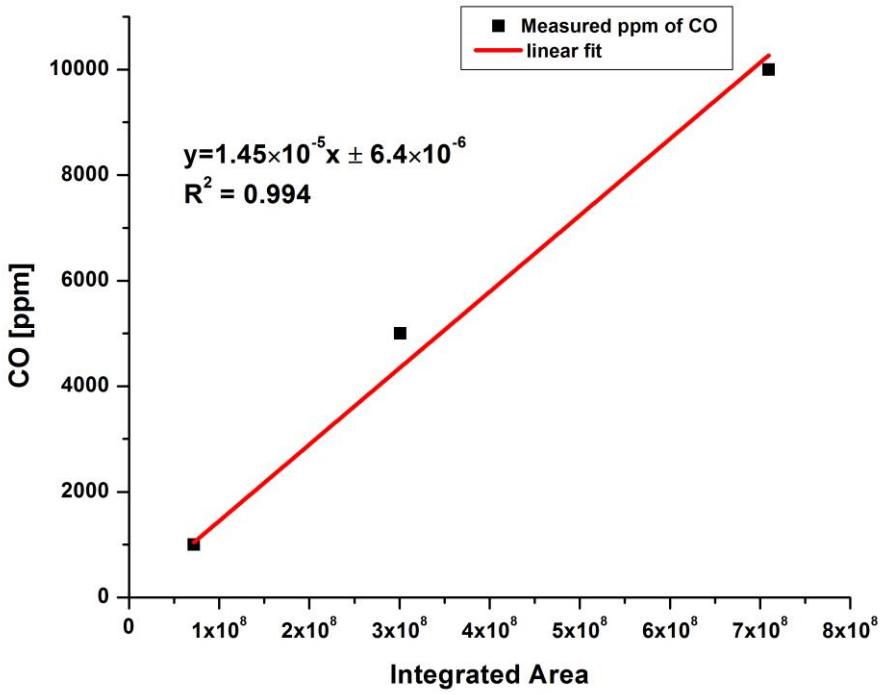

Figure A4. The slope of the linear fit is the calibration factor of CO used in the calculations above. The slope is obtained by plotting the ppm values dosed against the integrated area observed in the mass spectrometer of the GC-MS.

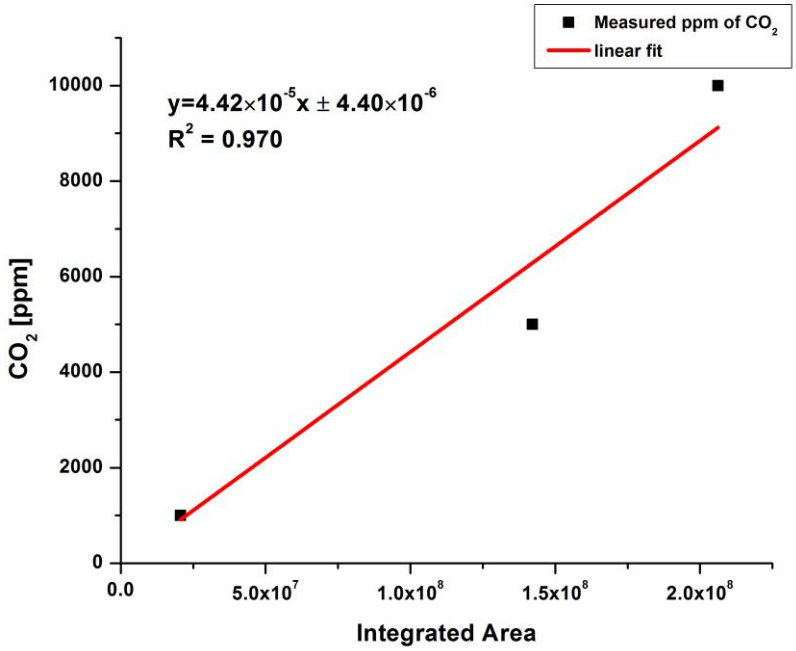

Figure A5. The slope of the linear fit is the calibration factor of CO_2 used in the calculations above. The slope is obtained by plotting the ppm values dosed against the integrated area observed in the mass spectrometer of the GC-MS.

7.5 Thermogravimetric Analysis of Template Removal in SAPO-34

The average template loss is estimated to be 16.8 ≈17 %, based on the Figure A6, with its corresponding values reported Table A4.

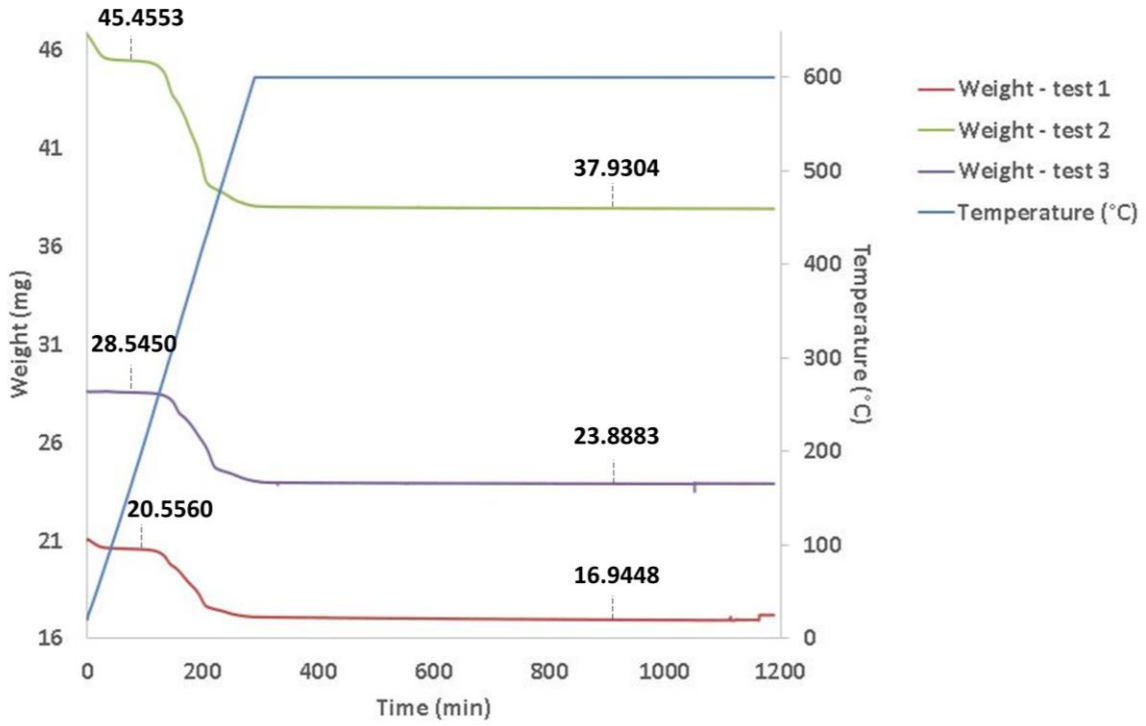

Figure A6. Template-loss in H-SAPO-34.

Table A4. Calculated weight loss for H-SAPO-34, reported in mass (g) and percentage (%).

	Weight loss (mg)	**Weight loss (%)**
Test 1	3.6112	17.6
Test 2	7.5249	16.6
Test 3	4.6567	16.3

7.6 Acetonitrile Adsorption with FTIR

Table A5. Calculated values of the area density of the three samples used in the Lambert-Beers law for calculating the concentration of CD_3CN per mass of zeolite.

	Water content (%)	Mass (mg)	dry mass (mg)	area density (mg/cm^2)*
H-SAPO-34	16.4	15.0	12.54	9.5
0.08CuSAPO-34/LIE	13.8	15.0	12.93	9.7
0.25CuSAPO-34/3xLIE	17.7	15.0	12.35	9.3
0.22CuSAPO-34/SSIE	6.94	15.0	13.96	10.5

*Area of pellet: 1.33 cm^2

Table A6. Peak position and integrated area of the Lewis and Brønsted acid sites, found with deconvolution of the graphs below into Gaussian curves.

	Lewis acid site position (cm^{-1})	Lewis acid site - integrated area (cm^{-1})	Brønsted acid site position (cm^{-1})	Brønsted acid site - integrated area (cm^{-1})
H-SAPO-34	2318	6.60	2293	2.20
0.08CuSAPO-34/LIE	2318	4.53	2294	1.29
0.25CuSAPO-34/3xLIE	2316	4.27	2298	1.71
0.22CuSAPO-34/SSIE	2316	5.91	2295	0.69

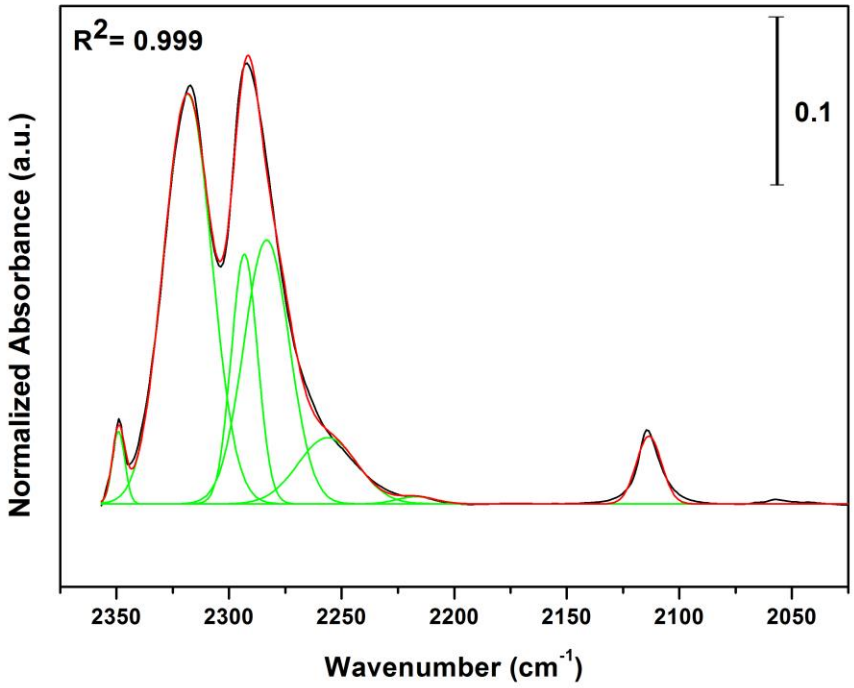

Figure A7. Deconvoluted spectrum of H-SAPO-34. The spectra have been normalized to the framework, bfore the activated spectrum before dosing has been subtracted as background.

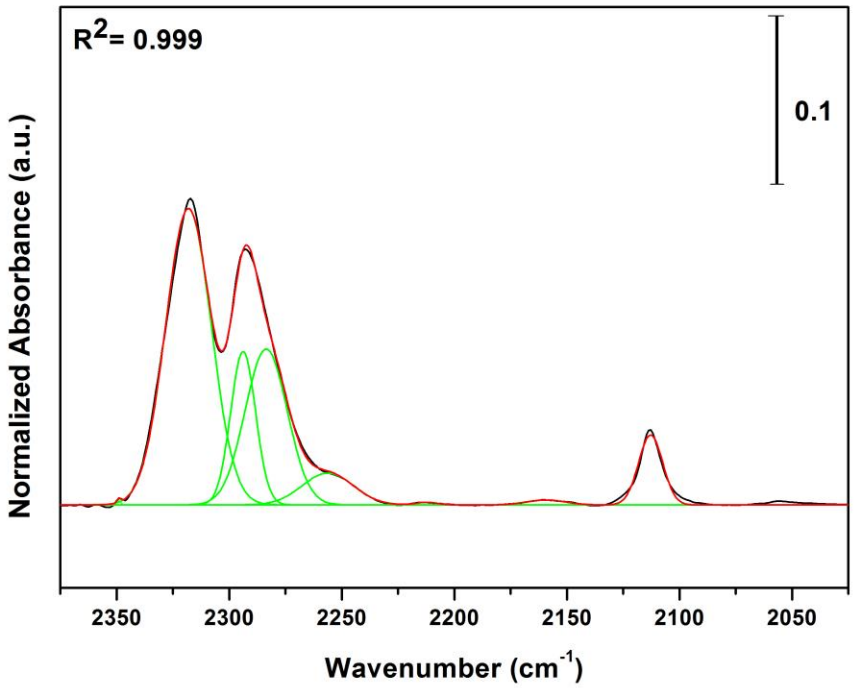

Figure A8. Deconvoluted spectrum of 0.08CuSAPO-34/LIE. The spectra have been normalized to the framework, bfore the activated spectrum before dosing has been subtracted as background.

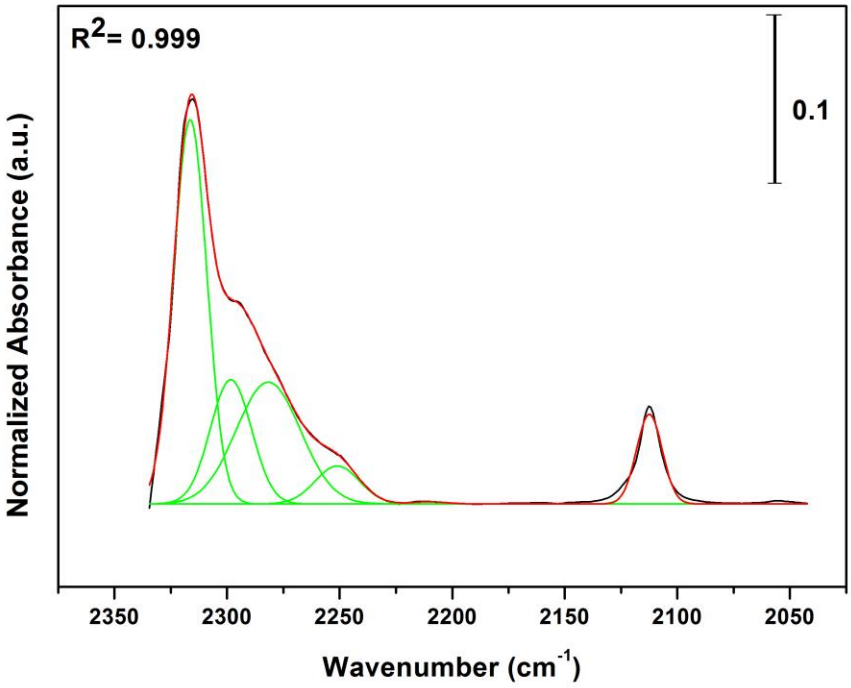

Figure A9. Deconvoluted spectrum of 0.25CuSAPO-34/3xLIE. The spectra have been normalized to the framework, bfore the activated spectrum before dosing has been subtracted as background.

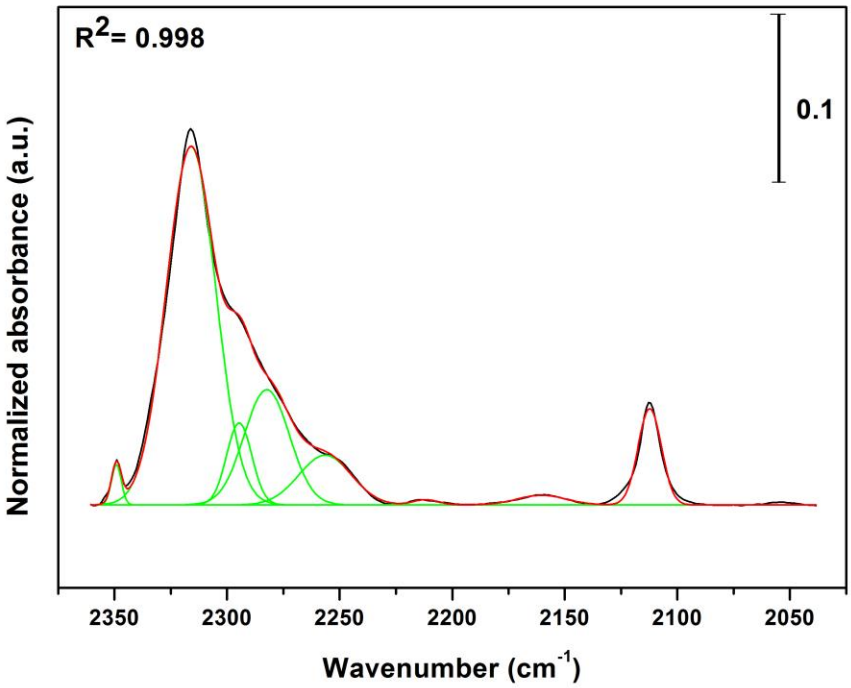

Figure A10. Deconvoluted spectrum of 0.22CuSAPO-34/SSIE. The spectra have been normalized to the framework, bfore the activated spectrum before dosing has been subtracted as background.

7.7 Difference in FTIR Spectra, Observed for 0.08CuSAPO-34/LIE

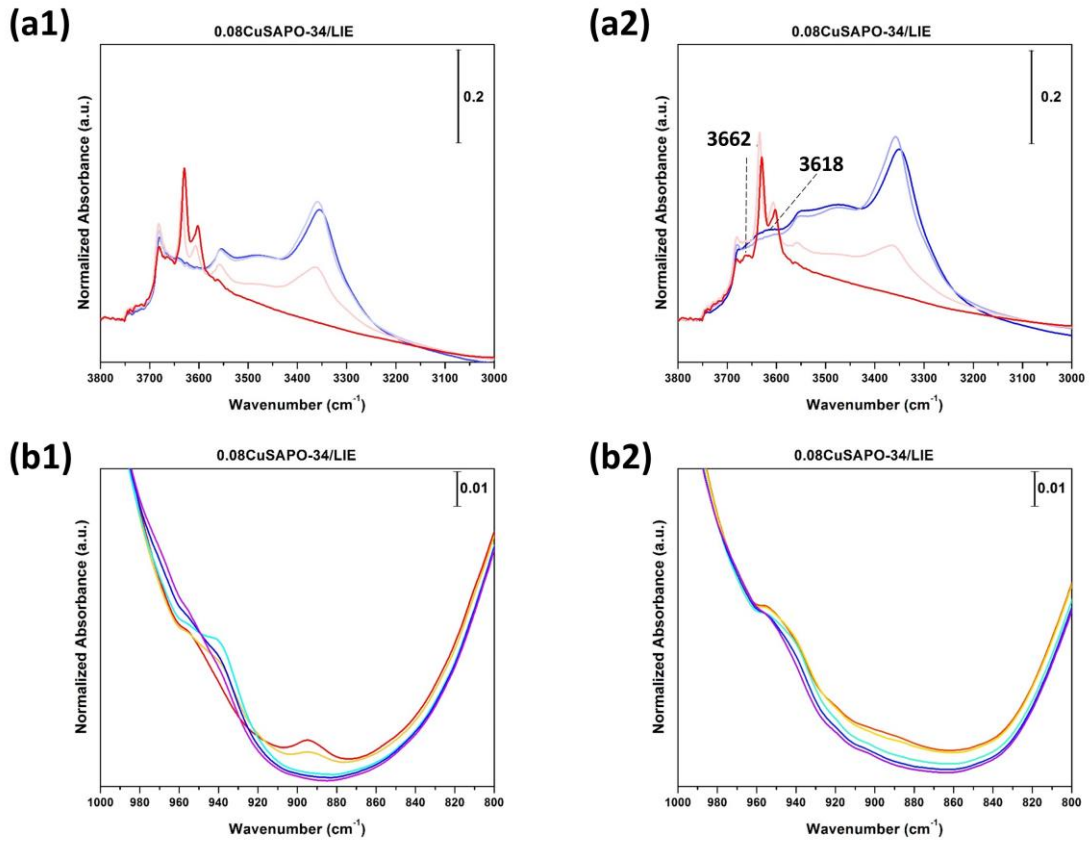

Figure A11. (a1) and (b1) are the spectra of the OH-stretching region interacting with CO, and framework vibration region of 0.08CuSAPO-34/LIE after activation in vacuum at 450 °C. (a2) and (b2) are the the same regions of 0.08CuSAPO-34/LIE after activation in vacuum at 300 °C.

7.8 Data Collected for the Articles Accepted in JACS and ACS Catalysis, 2018

Data Tested for the Article Accepted in ACS Catalysis [9]

The first three materials in Table A7 was stability tests performed in a multiple process cycle. First, the materials were dried in He at 150 °C, before the materials were ramped in O_2 at 5 °C/min, and kept there for 8 h. The materials were then cooled to 200 °C, and purged with He for 45 min. Then, CH_4 was loaded for 6 h, before He was purged again for 45 min. Finally, the H_2O-assisted extraction of methanol was performed at 200 °C. After each reaction cycle, the materials were kept in a He flow at 200 °C, before the materials were subjected to a new full cycle. The data obtained from the multiple cycle process are illustrated in Figure A12, together with other MOR-materials tested by Dimitrios Pappas. The figure is copied from the published article.

The last three materials in Table A7 was tested with the same reaction conditions as presented above for one cycle, to compare characterizations of the materials before and after being exposed to the reaction conditions.

Table A7. Performance data of the Cu-Mordenite zeolites (calculated after 1st extraction) tested for the ACS Catalysis paper.

	Exch.	MeOH (μmol/g)	CO_x (μmol/g)	Selectivity (%)	Productivity (mol_{MeOH}/mol_{Cu})
0.11Cu,H-MOR/11 *	LIE	39.0	6.4	86.0	0.21***
0.36Cu,H-MOR/11	LIE	124.3	10.6	92.1	0.25***
0.09Cu,H-MOR/11/Cl**	SSIE	36.1	5.5	86.9	0.28***
0.06Cu,H-MOR/7	LIE	37.4	7.4	83.5	0.30
0.18Cu,Na-MOR/11	LIE	36.2	6.1	86.9	0.15
0.32Cu,Na-MOR/11	LIE	73.8	11.0	87.0	0.17

*The name is abbreviated as follows: The first value is the Cu/Al ratio, and the number at the end is the Al/Si ratio of the samples.

**The Cl at the end of the name indicates that the ion exchange were performed with $CuCl_2$ as Cu-precursor.

***Test repeated 3 times, with a flushing step in He at 200 °C, before the test were started again.

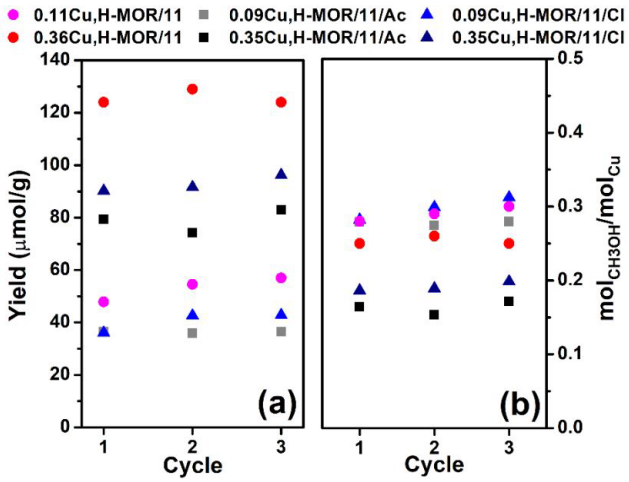

Figure A12. Published plot of the stability tests that were performed on the first three materials in the table above.

Data Tested for the Article Accepted in JACS [82]

All the different test conditions employed are presented in Table A8.

Test #1 was tested on the materials to replicate the Operando XAS test conditions used during XAS experiments at the BM31 beamline at ESRF, to investigate reproducibility of values obtained from the MS-spectrometer connected to the setup at ESRF.

Test #2 was tested on the materials to replicate the O_2 activation step used during HERFD XANES experiments used at ID26 beamline at ESRF, to ensure that the normalized productivity can be quantitatively correlated with the fraction of active Cu evaluated from spectroscopy.

Test #2.1 was performed to investigate if a prolonged CH_4-activation step would alter the productivity values obtained from test #2.

Test #4 was tested on MOR samples with Si/Al = 7, to replicate the test conditions used during HERFD XANES experiments used at ID26 beamline at ESRF.

In Table A9 are all the productivity values that was obtained for the different materials presented.

Table A8. Test conditions employed on the different activity tests.

	He activation (°C) [time(min)]	**O_2 activation (°C) [time(min)]**	**CH_4 loading (°C) [time(min)]**	**H_2O-assisted Methanol extraction (°C) [time(min)]**
Test #1	-	500 [90]	200 [120]	200 [70]
Test #2	-	500 [30]	200 [360]	200 [70]
Test #2.1	-	500 [30]	200 [480]	200 [70]
Test #3	500 [240]	500 [150]	200 [360]	200 [70]

Table A9. Productivity data obtained for all materials tested in the different conditions.

	Exch.	**Productivity Test #1 (mol_{MeOH}/mol_{Cu})**	**Productivity* Test #2 ($mol_{act.Me}/mol_{Cu}$)**	**Productivity* Test #2.1 ($mol_{act.Me}/mol_{Cu}$)**	**Productivity Test #3 (mol_{MeOH}/mol_{Cu})**
0.28Cu,H-MOR/11	LIE		0.140		
0.36Cu,H-MOR/11 *	LIE	0.076	0.084	0.087	
0.18Cu,H-MOR/7 *	LIE	0.129	0.247	0.237	
0.24Cu,H-MOR/7*	LIE		0.100		0.152

*Productivity of these tests are reported as the total amount of activated methane per Cu content.

7.9 Reported Productivity Values from Literature for Cu-CHA Used in the DMTM-conversion

Table A10. Overview from literature on the effect of composition and reaction conditions on the productivity of Cu-CHA. Table is published in [14].

Table 1 Performance of Cu loaded CHA materials (SSZ-13 and SAPO-34) in the stepwise selective oxidation of methane to methanol. Information about the cation predominantly present in the parent material (sodium or proton), elemental composition and copper loading, details of the three steps of the reaction protocol, the means by which the products were detected and quantified, the productivities (normalized to both mass of material and Cu loading), the selectivity, and notes about the exact Cu introduction procedure are listed. Values in italics have been recalculated by us from the published data for completeness. Some of the data reported here are summarized in Fig. 20. Previously unpublished table summarizing data taken form ref. 28, 30 and 33–35

Zeolite	Si/Al or (Al + P)/Si	Cu/Al or Cu/Si	Cu (wt%)	Protocol	Detection principle	Productivity ($\mu mol\ g^{-1}$)		Productivity (mol_{MeOH}/mol_{Cu})		Selectivity	Preparation	Ref.
Na-SSZ-13	6	0.35 ± 0.07	*5.0*[a]	(i) 10 h in O_2 at 450 °C (ii) 20 + 20 min in 7.5 kPa CH_4 at 60 and 200 °C (iii) 5 h with N_2 saturated with water vapor at 200 °C	On-line GC and MS	28		0.03		Not reported	Liquid exchange of Na-form with copper(II)acetate	28
Na-SSZ-13	12	0.35 ± 0.06	*2.8*	As above	As above	31		0.06		As above	As above	28
Na-SAPO-34	5	0.17 ± 0.06	*2.9*	As above	As above	<1		<0.001		As above	As above	28
H-SAPO-34	6	0.6 ± 0.2	*8.2*	(i) 10 h in N_2 at 650 °C; 15 h in O_2 at 450 °C (ii) 20 + 20 min in 7.5 kPa CH_4 at 60 and 200 °C (iii) 8 h with N_2 saturated with water vapor at 200 °C	As above	15		0.01		As above	High temperature gas–solid exchange of H-form with copper(I)chloride	28
H-SSZ-13	6	0.6 ± 0.3	*8.3*	As above	As above	5		0.003		As above	As above	28
H-SSZ-13	12	0.8 ± 0.3	*6.1*	As above	As above	10		0.008		As above	As above	28
H-SSZ-13	5	0.39	6.5	(i) 7 h in O_2 at 450 °C (ii) 20 min in neat CH_4 at 50 °C (iii) N_2 saturated with water vapor at 200 °C	On-line GC and MS	28.5		0.03		Not reported	Liquid exchange of H-form with copper(II)acetate	30
H-SSZ-13	12	0.40	*3.2*	As above	As above	26		0.05		As above	As above	30
Na-SSZ-13	12	0.47	*3.7*	As above	As above	28.1		0.05		As above	Liquid exchange of Na-form with copper(II)acetate	30
Na-SSZ-13	12	0.47	*3.7*	(i) 4 h in He at 450 °C (ii) 20 min in neat CH_4 at 50 °C (iii) N_2 saturated with water vapor at 200 °C	As above	10		0.018		As above	As above	30
Na-SSZ-13	15.8	0.84	4.5	(i) 4 h in O_2 at 450 °C (ii) 30 min in neat CH_4 at 200 °C (iii) Repeated stirring with deionized water for 24 h	GC-FID analysis of extracts	30.0		0.0424		Not reported	Liquid exchange of Na-form with copper(II)acetate	34
Na-SSZ-13	20	*0.30*	1.5	(i) 2 h in O_2 at either 450 °C or 550 °C (ii) 20 min in 38 kPa CH_4 at 60 °C, heating to 200 °C in 38 kPa CH_4 (iii) N_2 saturated with water vapor at 200 °C for 110 min	On-line GC-FID	7.6		0.033		Not reported	Liquid exchange of Na-form with copper(II)acetate	35
Na-SSZ-13	20	*0.28*	1.38	As above	As above	7.6		0.036		As above	Liquid exchange of Na-form with copper(II)sulfate	35
Na-SSZ-13	20	*0.23*	1.15	As above	As above	7.2		0.041		As above	As above	35
Na-SSZ-13	20	*0.24*	1.21	As above	As above	*8.2*[b]	*9.0*[c]	*0.045*[b]	*0.049*[c]	As above	As above	35
H-SSZ-13	20	*0.23*	1.14	As above	As above	*6.3*[b]	*7.6*[c]	*0.036*[b]	*0.043*[c]	As above	Liquid exchange of H-form with copper(II)sulfate	35
Na-SSZ-13	20	*0.19*	0.95	As above	As above	*4.9*[b]	*7.5*[c]	*0.034*[b]	*0.052*[c]	As above	Liquid exchange of Na-form with copper(II)sulfate	35

Table 1 (*continued*)

Zeolite	Si/Al or (Al + P)/Si	Cu/Al or Cu/Si	Cu (wt%)	Protocol	Detection principle	Productivity ($\mu mol\ g^{-1}$)	Productivity (mol_{MeOH}/mol_{Cu})	Selectivity	Preparation	Ref.
Na-SSZ-13	20	*0.20*	1.03	As above	As above	5.3	0.034	As above	As above	35
Na-SSZ-13	20	*0.19*	0.93	As above	As above	5.4	0.038	As above	Liquid exchange of Na-form with copper(II)acetate	35
Na-SSZ-13	20	*0.18*	0.91	As above	As above	4.7	0.034	As above	Liquid exchange of Na-form with copper(II)sulfate	35
Na-SSZ-13	5.2	0.49	*7.0*	(i) 8 h in O_2 at 500 °C (ii) 6 h in neat CH_4 at 200 °C (iii) He/Ne saturated with water vapor (saturator at 45 °C) at 200 °C for 110 min	GC-MS both dimethyl ether and methanol considered products; CO and CO_2 as by-products	132	0.112	87% to MeOH and DME	Liquid exchange of H-form with copper(II)acetate	33
Na-SSZ-13	12.1	0.14	*1.1*	As above	As above	17.5	0.097	85%	As above	33
Na-SSZ-13	12.1	0.16	*1.3*	As above	As above	19.3	0.097	85%	As above	33
Na-SSZ-13	12.1	0.34	*2.7*	As above	As above	67	0.16	87%	As above	33
Na-SSZ-13	12.1	0.49	*3.8*	As above	As above	107	0.172	87%	As above	33
Na-SSZ-13	14.8	0.53	*3.4*	As above	As above	88.9	0.165	87%	As above	33
Na-SSZ-13	28	0.52	*1.9*	As above	As above	39.3	0.131	86%	As above	33

[a] Values in italics are calculated by us from published data. [b] Pre-treated in oxygen at 450 °C. [c] Pre-treated in oxygen at 550 °C.

*The last six samples in the table are H-SSZ-13, and not Na-SSZ-13.

Bibliography

[1] ScienceFacts.net - Raman Spectroscopy, *https://www.sciencefacts.net/raman-spectroscopy.html* (Accessed: 29.12.2018).
[2] Borfecchia, E.; Lomachenko, K. A.; Giordanino, F.; Falsig, H.; Beato, P.; Soldatov, A. V.; Bordiga, S. and Lamberti, C., *Chemical Science* **2015**, *6*, 548-563.
[3] E. Bjorck, C.; D. Dobson, P. and Pandhal, J., *AIMS Bioengineering* **2018**, *5*, 1-38.
[4] Holmen, A., *Catalysis Today* **2009**, *142*, 2-8.
[5] Horn, R. and Schlögl, R., *Catalysis Letters* **2014**, *145*, 23-39.
[6] Zero Routine Flaring by 2030, *http://www.worldbank.org/en/programs/zero-routine-flaring-by-2030#1* (Accessed: 08.01.2019).
[7] Hydrogen Production: Natural Gas Reforming, *https://www.energy.gov/eere/fuelcells/hydrogen-production-natural-gas-reforming* (Accessed: 08.01.2019).
[8] McFarland, E., *Science* **2012**, *338*, 340-342.
[9] Dyballa, M.; Pappas, D. K.; Kvande, K.; Borfecchia, E.; Arstad, B.; Beato, P.; Olsbye, U. and Svelle, S., *ACS Catalysis* **2018**, *9*, 365-375.
[10] Tomkins, P.; Ranocchiari, M. and van Bokhoven, J. A., *Accounts of Chemical Research* **2017**, *50*, 418-425.
[11] Pappas, D. K.; Borfecchia, E.; Dyballa, M.; Pankin, I. A.; Lomachenko, K. A.; Martini, A.; Signorile, M.; Teketel, S.; Arstad, B.; Berlier, G.; Lamberti, C.; Bordiga, S.; Olsbye, U.; Lillerud, K. P.; Svelle, S. and Beato, P., *Journal of the American Chemical Society* **2017**, *139*, 14961-14975.
[12] Grundner, S.; Markovits, M. A.; Li, G.; Tromp, M.; Pidko, E. A.; Hensen, E. J.; Jentys, A.; Sanchez-Sanchez, M. and Lercher, J. A., *Nature Communications* **2015**, *6*, 7546.
[13] Groothaert, M. H.; Smeets, P. J.; Sels, B. F.; Jacobs, P. A. and Schoonheydt, R. A., *Journal of the American Chemical Society* **2005**, *127*, 1394-1395.
[14] Borfecchia, E.; Beato, P.; Svelle, S.; Olsbye, U.; Lamberti, C. and Bordiga, S., *Chemical Society Reviews* **2018**, *47*, 8097-8133.
[15] Olsbye, U.; Svelle, S.; Bjorgen, M.; Beato, P.; Janssens, T. V.; Joensen, F.; Bordiga, S. and Lillerud, K. P., *Angewandte Chemie International Edition* **2012**, *51*, 5810-5831.
[16] Cortés-Reyes, M.; Finocchio, E.; Herrera, C.; Larrubia, M. A.; Alemany, L. J. and Busca, G., *Microporous and Mesoporous Materials* **2017**, *241*, 258-265.
[17] Chorkendorf, I. and Niemantsverdriet, J. W., *Concepts of Modern Catalysis and Kinetics*, WILEY-VCH, **2007**.
[18] Roth, J. F., *Platinum Metals Review* **1975**, *19*, 12-14.
[19] Dyer, A., *An Introduction to Zeolite Molecular Sieves*, John Wiley & Sons, **1988**.
[20] Lillerud, K. P., *KJM5810 Heterogeneous Catalysis - lecture notes* **2018**.
[21] Łukaszuk, K., *Controlling the Morphology of Zeolite Crystals in OFF and MTT/TON Systems (Doctoral dissertation)*, Department of Chemistry, Faculty of Mathematics and Natural Sciences, University of Oslo, **2018**.
[22] Bekkum, H. v.; Flanigen, E. M.; Jacobs, P. A. and Jansen, J. C., *Elsevier* **2001**, *137*, 11-35.
[23] Weitkamp, J., *Solid State Ionics* **2000**, *131*, 175-188.
[24] Pinilla-Herrero, I.; Olsbye, U.; Márquez-Álvarez, C. and Sastre, E., *Journal of Catalysis* **2017**, *352*, 191-207.

[25] Vercaemst, C., *Isomeric Olefinic Periodic Mesoporous Organosilicas: An Emerging Class of Versatile Nanomaterials (Doctoral dissertation)*, Department of Inorganic and Physical Chemistry, Faculty of Sciences, Ghent University, **2009**.
[26] Teketel, S.; Skistad, W.; Benard, S.; Olsbye, U.; Lillerud, K. P.; Beato, P. and Svelle, S., *ACS Catalysis* **2012**, *2*, 26-37.
[27] Nystrom, S.; Hoffman, A. and Hibbitts, D., *ACS Catalysis* **2018**, *8*, 7842-7860.
[28] Bordiga, S.; Regli, L.; Cocina, D.; Lamberti, C.; Bjørgen, M. and Lillerud, K. P., *The Journal of Physical Chemistry B* **2005**, *109*, 2779-2784.
[29] Sławiński, W. A.; Wragg, D. S.; Akporiaye, D. and Fjellvåg, H., *Microporous and Mesoporous Materials* **2014**, *195*, 311-318.
[30] Albuquerque, A.; Coluccia, S.; Marchese, L. and Pastore, H. O., *Studies in Surface Science and Catalysis* **2004**, *154*, 966-970.
[31] Ravi, M.; Ranocchiari, M. and van Bokhoven, J. A., *Angewandte Chemie International Edition* **2017**, *56*, 16464-16483.
[32] Galadima, A. and Muraza, O., *Journal of Industrial and Engineering Chemistry* **2016**, *37*, 1-13.
[33] Guo, X.; Fang, G.; Li, G.; Ma, H.; Fan, H.; Yu, L.; Ma, C.; Wu, X.; Deng, D.; Wei, M.; Tan, D.; Si, R.; Zhang, S.; Li, J.; Sun, L.; Tang, Z.; Pan, X. and Bao, X., *Science* **2014**, *344*, 616-619.
[34] Morejudo, S. H.; Zanón, R.; Escolástico, S.; Yuste-Tirados, I.; Malerød-Fjeld, H.; Vestre, P. K.; Coors, W. G.; Martínez, A.; Norby, T.; Serra, J. M. and Kjølseth, C., *Science* **2016**, *353*, 563-566.
[35] Periana, R. A.; Taube, D. J.; Gamble, S.; Taube, H.; Satoh, T. and Fujii, H., *Science* **1998**, *280*, 560-564.
[36] Alayon, E. M.; Nachtegaal, M.; Ranocchiari, M. and van Bokhoven, J. A., *Chemical Communications* **2012**, *48*, 404-406.
[37] Beznis, N. V.; Weckhuysen, B. M. and Bitter, J. H., *Catalysis Letters* **2010**, *138*, 14-22.
[38] Borfecchia, E.; Pappas, D. K.; Dyballa, M.; Lomachenko, K. A.; Negri, C.; Signorile, M. and Berlier, G., *Catalysis Today* **2018**, *https://doi.org/10.1016/j.cattod.2018.07.028*.
[39] Pappas, D. K.; Borfecchia, E.; Dyballa, M.; Lomachenko, K. A.; Martini, A.; Berlier, G.; Arstad, B.; Lamberti, C.; Bordiga, S.; Olsbye, U.; Svelle, S. and Beato, P., *ChemCatChem* **2018**, *10*, 1-8.
[40] Narsimhan, K.; Iyoki, K.; Dinh, K. and Roman-Leshkov, Y., *ACS Central Science* **2016**, *2*, 424-429.
[41] Wulfers, M. J.; Teketel, S.; Ipek, B. and Lobo, R. F., *Chemical Communications* **2015**, *51*, 4447-4450.
[42] Jørgensen, S., *MENA3100, Scanning Electron Microscopy - lecture notes* **2018**.
[43] Materials Evaluation and Engineering, Inc. (MEE), *https://www.mee-inc.com/hamm/energy-dispersive-x-ray-spectroscopyeds/* (Accessed: 02.12.2018).
[44] Wragg, D., *Powder X-ray Diffraction, module - lecture notes* **2017**.
[45] Hogg, C. R.; Kadane, J. B.; Lee, J. S. and Majetich, S. A., *Bayesian Analysis* **2010**, *5*, 1-34.
[46] Tatlier, M.; Munz, G. and Henninger, S. K., *Microporous and Mesoporous Materials* **2018**, *264*, 70-75.
[47] PerkinElmer, *A Beginners Guide to Thermogravimetric Analysis (TGA)*, 009380c_009301 PKI.
[48] Kolboe, S., *Chemical Kinetics and Catalysis - a very short introduction*, Compendium.

[49] Larkin, P. J., *Infrared and Raman Spectroscopy - Principles and Spectral Interpretation*, Elsevier, **2011**.
[50] Pavia, D. L.; Lampman, G. M.; Kriz, G. S. and Vyvyan, J. A., *Introduction to Spectroscopy*, CENGAGE Learning, 4th edition, **2008**.
[51] Raman Spectroscopy - A Tutorial, *https://www.kosi.com/na_en/products/raman-spectroscopy/raman-technical-resources/raman-tutorial.php* (Accessed: 02.12.2018).
[52] kjernemagnetisk resonans (NMR), *https://snl.no/kjernemagnetisk_resonans_(NMR)* (Accessed: 02.12.2018).
[53] Polenova, T.; Gupta, R. and Goldbourt, A., *Anal Chem* **2015**, *87*, 5458-5469.
[54] Penner-Hahn, J. E., *X-ray Absorption Spectroscopy*, Elsevier, 2nd edition, **2003**, 159-186.
[55] Arstad, B.; Lind, A.; Cavka, J. H.; Thorshaug, K.; Akporiaye, D.; Wragg, D.; Fjellvåg, H.; Grønvold, A. and Fuglerud, T., *Microporous and Mesoporous Materials* **2016**, *225*, 421-431.
[56] Shwan, S.; Skoglundh, M.; Lundegaard, L. F.; Tiruvalam, R. R.; Janssens, T. V. W.; Carlsson, A. and Vennestrøm, P. N. R., *ACS Catalysis* **2015**, *5*, 16-19.
[57] Vennestrøm, P. N. R.; Katerinopoulou, A.; Tiruvalam, R. R.; Kustov, A.; Moses, P. G.; Concepcion, P. and Corma, A., *ACS Catalysis* **2013**, *3*, 2158-2161.
[58] Wichterlová, B.; Tvarůžková, Z.; Sobalík, Z. and Sarv, P., *Microporous and Mesoporous Materials* **1998**, *24*, 223-233.
[59] Mathon, O.; Beteva, A.; J. Borrel, D. B.; S. Gatla, R. H.; Kantor, I.; Mairs, T.; Munoz, M.; Pasternak, S.; Perrin, F. and Pascarelli, S., *Journal of Synchrotron Radiation* **2015**, *22*, 1548-1554.
[60] Bellet, D.; Gorges, B.; Dallery, A.; Bernard, P.; Pereiro, E. and Baruchel, J., *Journal of Applied Crystallography* **2003**, *36*, 366-367.
[61] Giordanino, F.; Borfecchia, E.; Lomachenko, K. A.; Lazzarini, A.; Agostini, G.; Gallo, E.; Soldatov, A. V.; Beato, P.; Bordiga, S. and Lamberti, C., *The Journal of Physical Chemistry Letters* **2014**, *5*, 1552-1559.
[62] Bordiga, S.; Groppo, E.; Agostini, G.; Bokhoven, J. A. v. and Lamberti, C., *Chemical Reviews* **2013**, *113*, 1736-1850.
[63] Ravel, B. and Newville, M., *Journal of Synchrotron Radiation* **2005**, *12*, 537-541.
[64] Dean, J. A., *Lange's handbook of chemistry*, McGraw-Hill Inc., 15th edition, **1999**, 5.28-25.29.
[65] Gas Chromatography-Mass Spectroscopy Background, *https://www.gmu.edu/depts/SRIF/tutorial/gcd/gc-ms2.htm* (Accessed: 12.11.2018).
[66] Stakheev, A. Y.; Bokarev, D. A.; Mytareva, A. I.; Janssens, T. V. W. and Vennestrøm, P. N. R., *Topics in Catalysis* **2016**, *60*, 255-259.
[67] Cubillas, P. and Anderson, M. W., *Zeolites and Catalysis: Synthesis, Reactions and Applications, Vol. 1, Synthesis Mechanism: Crystal Growth and Nucleation*, Wiley-VCH Verlag GmbH & Co., **2010**, 1-55.
[68] Smith, R. L.; Svelle, S.; del Campo, P.; Fuglerud, T.; Arstad, B.; Lind, A.; Chavan, S.; Attfield, M. P.; Akporiaye, D. and Anderson, M. W., *Applied Catalysis A: General* **2015**, *505*, 1-7.
[69] Smith, R. L.; Sławiński, W. A.; Lind, A.; Wragg, D. S.; Cavka, J. H.; Arstad, B.; Fjellvåg, H.; Attfield, M. P.; Akporiaye, D. and Anderson, M. W., *Chemistry of Materials* **2015**, *27*, 4205-4215.
[70] Wang, Y.; Chen, S.-L.; Jiang, Y.-J.; Cao, Y.-Q.; Chen, F.; Chang, W.-K. and Gao, Y.-L., *RSC Advances* **2016**, *6*, 104985-104994.
[71] Martins, G. V. A.; Berlier, G.; Bisio, C.; Coluccia, S.; Pastore, H. O. and Marchese, L., *The Journal of Physical Chemistry C* **2008**, *112*, 7193-7200.

[72] Akolekar, D. B.; Bhargavaa, S. K. and Foger, K., *Journal of the Chemical Society, Faraday Transactions* **1998**, *94*, 155-160.
[73] Buchholz, A.; Wang, W.; Xu, M.; Arnold, A. and Hunger, M., *Microporous and Mesoporous Materials* **2002**, *56*, 267-278.
[74] Buchholz, A.; Wang, W.; Arnold, A.; Xu, M. and HUnger, M., *Microporous and Mesoporous Materials* **2003**, *57*, 157-168.
[75] Kalantzopoulos, G. N.; Lundvall, F.; Checchia, S.; Lind, A.; Wragg, D. S.; Fjellvag, H. and Arstad, B., *Chemphyschem* **2018**, *19*, 519-528.
[76] Deka, U.; Lezcano-Gonzalez, I.; Warrender, S. J.; Lorena Picone, A.; Wright, P. A.; Weckhuysen, B. M. and Beale, A. M., *Microporous and Mesoporous Materials* **2013**, *166*, 144-152.
[77] Gao, F.; Walter, E. D.; Washton, N. M.; Szanyi, J. and Peden, C. H. F., *Applied Catalysis B: Environmental* **2015**, *162*, 501-514.
[78] Giordanino, F.; Vennestrom, P. N.; Lundegaard, L. F.; Stappen, F. N.; Mossin, S.; Beato, P.; Bordiga, S. and Lamberti, C., *Dalton Transactions* **2013**, *42*, 12741-12761.
[79] Bulanek, R.; Frolich, K.; Cicmanec, P.; Nachtigallova, D.; Pulido, A. and Nachtigall, P., *The Journal of Physical Chemistry C* **2011**, *115*, 13312-13321.
[80] Kwak, J. H.; Varga, T.; Peden, C. H. F.; Gao, F.; Hanson, J. C. and Szanyi, J., *Journal of Catalysis* **2014**, *314*, 83-93.
[81] Lei, G. D.; Adelman, B. J.; Sárkány, J. and Sachtler, W. M. H., *Applied Catalysis B: Environmental* **1995**, *5*, 245-256.
[82] Pappas, D. K.; Martini, A.; Dyballa, M.; Kvande, K.; Teketel, S.; Lomachenko, K. A.; Baran, R.; Glatzel, P.; Arstad, B.; Berlier, G.; Lamberti, C.; Bordiga, S.; Olsbye, U.; Svelle, S.; Beato, P. and Borfecchia, E., *Journal of the American Chemical Society* **2018**, *140*, 15270-15278.
[83] Wang, L.; Li, W.; Qi, G. and Weng, D., *Journal of Catalysis* **2012**, *289*, 21-29.
[84] Chen, P.; Root, D. E.; Campochiaro, C.; Fujisawa, K. and Solomon, E. I., *Journal of the American Chemical Society* **2003**, *125*, 466-474.
[85] Ipek, B.; Wulfers, M. J.; Kim, H.; Göltl, F.; Hermans, I.; Smith, J. P.; Booksh, K. S.; Brown, C. M. and Lobo, R. F., *ACS Catalysis* **2017**, *7*, 4291-4303.
[86] Root, D. E.; Mahroof-Tahir, M.; Karlin, K. D. and Solomon, E. I., *Inorganic Chemistry* **1998**, *37*, 4838-4848.
[87] Woertink, J. S.; Smeets, P. J.; Groothaert, M. H.; Vance, M. A.; Sels, B. F.; Schoonheydt, R. A. and Solomon, E. I., *PNAS* **2009**, *106*, 18908-18913.